Diffusion in Mesoporous Glass: Simulations and Experiments

Thesis by

Neil Edward Fernandes

In Partial Fulfillment of the Requirements

for the Degree of

Doctor of Philosophy

California Institute of Technology

Pasadena, California

1997

(Submitted April 24, 1997)

To Mum and Dad

Acknowledgements

I have had a good time here at Caltech for the past five odd years, and it has been filled with the ups and downs that one can always expect to face in life. I am in one of those downs right now, sitting here as I am with a torn MCL and in a reasonable amount of pain. Nevertheless, it is good to have the chance to acknowledge those colleagues and friends who were essential to my success at Caltech.

I would like to thank my advisor, Dr. George Gavalas, for being my mentor over the past years. I don't think I could have worked with a more knowledgeable and motivated person. I greatly appreciate your patience with me George, and look forward to our future collaboration. I would also like to thank Dr. Rick Flagan, Dr. Mark Davis, and Dr. Konstantinos Giapis, for reviewing my thesis, and providing many helpful insights. My work here at Caltech has been an instructive blend of theory and experiments, but the latter could not have been successful without the support of Dr. Konstantinos Giapis, Rodney Rojas, Brian Franklin, Rick Gerhart, Suresha Gupta, Dr. John Thornley, and Tom Dunn. Thank you all for lending your expertise.

I would also like to thank Dr. Michael Tsapatsis and Dr. Soojin Kim, for the groundwork they did for my project; and the past and present members of my group, Dr. Yushan Yan, Shaocong, Ramesh, and Rei, for their helpful input.

I have been blessed with many friends here at Caltech. At the risk of possibly omitting the names of people whose support has meant so much to me, I would like to mention just a few.

Thank you Rodney, Denis, John, Greg, Jay, and Pat for making lunch time so entertaining. You're mates and a half.

I spent at least half of my time at Caltech, drinking tea at the Red Door Café, and I am grateful to Matt, Mark, and Muruhan, for relieving me of any guilt by their similar presence.

This last year would have been unbearable but for the establishment of the Caltech Rugby Football Club. I have not played with a finer bunch of blokes, nor enjoyed the support of a more vocal bunch of supporters. I look forward to playing with you guys again in December. Thanks also for the going away present!

I was also fortunate enough to captain and manage the department soccer team, Real Scared, for some years. Thanks to those who participated in making this experience so very rich.

Throughout my years here I have been blessed with the company of amiable flatmates. Bob and Todd, thank you for having been so considerate in the last half year. I am grateful.

Nancy, Lisa, Mike, Paul, Yvette, Pat, Linda, Matt, Frank, Pablo, Dave, Andrew, and Matt, your friendship has meant so much to me. I cannot easily express my sentiments in writing, so I will not try. Paul and Yvette, I was truly honoured to be at your wedding. Andrew and Matt, it was great spending time with you guys in Jamaica, I suspect you will both owe me crates within the next couple of years. And Dave - I'll sorely miss thumping you in pool!

Finally, a special thank you to my family, Mum, Dad, Heather, Paul and JoAnn, for their support. Mum and Dad, I am more proud of you than you could ever be of me.

Abstract

The diffusivities of simple gases in mesoporous glass were studied by experiment and simulation.

Porous Vycor® glass was modified by deposition of silica on the internal pore surface using consecutive cycles of liquid phase silylation with silicon tetrachloride, and hydrolysis. Macroscopically uniform deposition was achieved by exploiting the self limiting nature of the reaction and the extent of deposition was monitored by the weight change of the samples. Weight increases as high as 24% were recorded and the average pore diameter was estimated to decrease from ~44Å to ~20Å. Permeation measurements were conducted in the Henry's law region at various levels of deposition for hydrogen, methane, isobutane and nitrogen, at temperatures between 60°C and 180°C. The measurements were compared to values calculated with a model using the effective medium approximation to treat network effects and Clausing's correction to account for conductances in pores of finite aspect ratio. The calculated values proved to be inaccurate for hydrogen, overestimating the permeance by a factor of two at high levels of deposition possibly because of non-ideal pore shapes accentuated by the deposition. For nitrogen and methane the agreement between calculations and measurements was better due to a fortuitous cancellation of deviations caused by the enhanced potential energy well within the pores and the non ideal pore shape. The intrapore potential energy effect was especially strong for isobutane and as a result the calculated flux was always less than the experimental.

In an effort to understand the importance of the intrapore potential and pore surface roughness on diffusion, molecular dynamics simulations of nitrogen and isobutane in a mesoporous glass pore, under free molecular flow conditions, were conducted for pores of diameter 40Å to 20Å, and for temperatures between 200K and 800K. To study the effect of

the intrapore potential, the gases were treated as simple Lennard-Jones atoms and the pore was simulated as a perfect cylinder exerting a 9-3 potential, but with its surface roughened by the superposition of spherical Lennard-Jones atoms representing silica tetrahedra. The molecular trajectories were calculated by the application of Nosé-Hooverian mechanics and no momentum transfer was allowed between the pore walls and the gas molecules. Random walk behavior resulted from the resulting specular collisions. The effect of the intrapore potential was decoupled into two contributions. The effective diffusivity was respectively increased and decreased by a partitioning effect (or Henry's law adsorption) and a path curvature effect (the trapping of molecules near the surface). In pores of radius 40Å, both effects were present for temperatures as high as 500K, and were enhanced as the temperature decreased. For nitrogen, the combination of effects canceled over the temperature range of 500-200K and resulted in a temperature dependence similar to that of Knudsen diffusion. For isobutane, the partitioning effect overwhelmed the path curvature effect, resulting in significant surface flows at temperatures as high as 500K. At a temperature of 393K, as the pore radius was reduced from 40Å to 20Å, the path curvature effect decreased and the partitioning effect increased. Although the intrapore potential becomes more negative as the pore size decreases, the magnitude of the potential energy barrier trapping molecules near the surface also decreases. The effect of surface roughness was studied through a hard sphere dynamics version of the above simulation. Diffusivities were obtained for various surface coverage of the silica tetrahedra. The specular reflection condition resulted in diffusivities at least twice that of the Knudsen value.

Table of Contents

1. Introduction 1

1.1 Intoduction 2

Biliography 5

2. Gas Transport in Porous Vycor Glass Subjected to Gradual Pore Narrowing..... 7

Abstract 8

2.1 Introduction 9

2.2 Experimental 11

2.3 Capillary Network Model 14

2.4 Results 16

2.5 Discussion 18

2.6 Conclusion 23

2.7 Acknowledgments 23

2.8 Notation 24

Bibilography 26

3. Molecular Dynamics Simulation of Diffusion in Mesoporous Glass 45

Abstract 46

3.1 Introduction 47

3.2 Effects of the Intrapore Potential Field 48

3.2.1 Path Curvature 48

3.2.2 Partitioning and Henry's Law 51

3.3 Surface Roughness 53

3.4 Surface Reflections and Velocity Distributions 55

3.5 Molecular Dynamics Simulations 57

3.5.1 Diffusion in Rough Walled Pores 57

3.5.2 Pore Simulations 59

3.5.3 Soft Sphere Dynamics Simulations..... 61

3.5.4 Evaluation of the Partitioning Constants..... 63

3.5.5 Hard Sphere Dynamics Simulations..... 64

3.5.6 Simulation Algorithms..... 65

3.6 Results and Discussions..... 68

3.6.1 Molecular Interaction Parameters..... 68

3.6.2 Velocity Distributions..... 68

3.6.3 Hard Sphere Molecular Dynamics Results..... 69

3.6.4 Soft Sphere Molecular Dynamics Results..... 70

3.7 Conclusion..... 74

3.8 Acknowledgments..... 75

3.9 Notation..... 76

Bibliography..... 78

4. Concluding Remarks..... 96

4.1 Concluding Remarks..... 97

Bibliography..... 98

Appendix A

A Semi Analytical Technique for Describing Irreversible Fluid-Solid Reactions in Packed Columns..... 99

Abstract..... 100

A.1 Introduction..... 101

A.2 Analytical Development..... 102

A.3 Discussion and Conclusion..... 116

A.4 Acknowledgment..... 117

A.5 Notation..... 117

Bibliography..... 119

Appendix..... 120

Appendix B

Derivation of Mean Free Path Formulae in Chapter 3 130

B.1 Mean Free Path in a Slit with an Intrapore Potential..... 131

B.2 Random Walk in 1-D with Persistence of Velocity Effects..... 135

Appendix C

Gas Phase Deposition Experiments..... 136

C.1 Introduction 137

C.2 Pore Narrowing of Vycor Glass by Silica Deposition 137

C.2.1 Characteristics of Vycor®..... 137

C.2.2 Silica Deposition from the Gas Phase 140

C.2.3 Silica Deposition using the TEOS Precursor..... 141

C.2.4 Silica Deposition using Gas Phase $SiCl_4$..... 142

C.3 Experimental Apparatus and Design Schematics..... 143

C.3.1 The Reaction System 144

C.3.2 The Residual Gas Analyzer 145

C.4 Quantitative Measurements Using the RGA..... 147

C.4.1 Overview of the Quadrapole Mass Filter 147

C.4.2 Quantitative Measurements..... 149

List of Figures

2. Gas Transport in Porous Vycor Glass Subjected to Gradual Pore Narrowing

2.1 Cumulative weight gain of Vycor glass after each deposition cycle 30

2.2 Apparatus for permeance measurements by the pressure rise technique 31

2.3 Pore size distribution of Vycor before and after deposition..... 32

2.4 Normalized diffusivities of various gases vs extent of deposition at 180°C.. 33

2.5 Normalized diffusivities of various gases vs extent of deposition at 120°C.. 34

2.6 Normalized diffusivities of various gases vs extent of deposition at 60°C... 35

2.7 Normalized permeance of various gases through untreated Vycor vs temperature 36

2.8 Normalized permeance of various gases through Vycor after 5 cycles of deposition (19.8 wt% gain) vs temeperature 37

2.9 Effect of pressure difference on gas permeances..... 38

2.10 Experimental and calculated hydrogen permeances at 180°C for different assumed deposit densities..... 39

2 11 Conformal pore closing and pore closing by necking 40

2.12 Correction factor for pore necking for different assumed deposit densities... 41

2.13 Normalized permeance of different gases at 180°C vs extent of deposition .. 42

2.14 Normalized permeance of different gases at 120°C vs extent of deposition... 43

2.15 Normalized permeance of different gases at 60°C vs extent of deposition 44

3. Molecular Dynamics Simulation of Diffusion in Porous Glass

3.1 Molecular trajectories and the intrapore potential for the slit problem 82

3.2 Normalized mean free path of molecules with $u>\Phi^{1/2}$ as a function of Φ for D/H=1..... 83

3.3 Normalized mean free path as a function of Φ for D/H=1 84

3.4 Velocity distributions obtained from the SSMD simulation of nitrogen at 200K. Cluster density = 0.5 nm^{-2}..... 85

3.5 HSMD results of diffusion of isobutane, nirogen, and hydrogen in pores of R_p = 25Å at 393K 86

3.6 Intrapore potential for nitrogen in silica pores at various pore radii. The potential has been normalized with kT at 393K..... 87

3.7 Intrapore potential for nitrogen in silica pores at various pore radii. The potential has been normalized with kT at 393K..... 88

3.8 The variation of the partitioning constant K and its separate contributions K_V and K_H for nitrogen in silica pores of radius 25Å with temperature 89

3.9 The variation of the partitioning constant K and its separate contributions K_V and K_H for nitrogen in silica pores at 393K with pore radius..... 90

3.10 The variation of the nitrogen an isobutane pore diffusivities with temperature. R_p = 20Å 91

3.11 Variation of the nitrogen and isobutane effective pore diffusivities with temperature. R_p = 20Å..... 92

3.12 Variation of normalized pore diffusivities with pore radius at 393K 93

3.13 Variation of normalized effective pore diffusivities with pore radius at 393K..... 94

3.14 Comparison of SSMD simulation results with the pore narrowing experiment results. Normalized effective diffusivity vs pore radius..... 95

Appendix A

A Semi Analytical Technique for Describing Irreversible Fluid-Solid Reaction in Packed Columns

A.1 The function h(y) in Example 1 for $Bi_m = 50$ for various values of Φ^2..... 123

A.2 Development of the cumulative concentration profiles $Y(\xi,\tau)$ in Example 1 for $\Phi^2 = 100$, $Bi_m = 50$, $Pe = 1.1$, $\beta = 3.3$.....124

A.3 Development of the concentration profiles $y(\xi,\tau)$ in example 1 for $\Phi^2 = 100$, $Bi_m = 50$, $Pe = 1.1$, $\beta = 3.3$ 125

A.4 Concentration profiles of the solid reactant in Example 1 for $\Phi^2 = 100$ $Bi_m = 50$, $Pe = 1.1$, $\beta = 3.3$.....126

A.5 The effect of reaction rate constant on the shape of the breakthrough curve in Example 1 for $Bi_m = 50$, $Pe = 1.1$, $\beta = 3.3$, $L = 300$ 127

A.6 The effect of axial dispersion on the breakthrough curve in Example 1 for $\Phi^2 = 100$, $Bi_m = 50$, $L = 300$.....128

A.7 Breakthrough curves for the progressive conversion model and the shrinking core model of example 2 for $\Phi^2 = 100$, $Bi_m = 50$, $L = 300$, $Pe = 1.1$, $\beta = 3.3$.....129

Appendix C

Gas Phase Deposition Experiments

C.1 Reaction schematic for the CVD of silica.....156

C.2 Pore size distribution of the suspended and mounted Vycor samples after silica deposition by TEOS pyrolysis 157

C.3 Weight gain of powdered vycor after CVD of silica using $SiCl_4$.....158

C.4 CVDR and TGA schematic.....159

C.5 RGA schematic 160

C.6 Valve numbering for quantiative measurements using comparative calibration.....161

List of Tables

2. Gas Transport in Porous Vycor Glass Subjected to Gradual Pore Narrowing

2.1 Physical Properties of Vycor (Corning code 7930)..... 28

2.2 Tri-modal pore size distribution used to describe the initial pore structure of Vycor glass..... 28

2.3 Experimental and calculated permeances for untreated Vycor..... 29

2.4 Lennard-Jones (6-12) parameters of gases used in the permeation measurements..... 29

3 Molecular Dynamics Simulation of Diffusion in Porous Glass

3.1 Intermolecular potential parameters..... 81

Appendix C

C.1 Weight changes of Vycor samples habing undergone different pre-treatments..... 140

Chapter 1

Introduction

1.1 Introduction

Porous solids are involved in almost every large scale chemical industry, either at the heart of the process (e.g., heterogeneous catalysis, gasification) or in some secondary aspect (e.g., separations by membranes and adsorption). These operations are modeled at the level of the porous solid using a variety of expressions obtained from the judicious application of mass and energy balances (Levenspiel, 1972). However, all these models rely on the knowledge of at least one or two transport or reaction parameters such as the effective diffusivity or the reaction rate constant. These parameters effectively summarize in a single number very complicated molecular phenomena.

For example, one particular fluid-solid reaction problem of broad interest is that of diffusion and reaction in *dynamic pore structures*. Here as the reaction proceeds the pore structure changes either due to depletion of the solid from the pore walls (e.g., char gasification) or by growth of the pore wall due to deposition or reaction (e.g., lime sulfation). Several elegant models (e.g., Yu and Sotirchos, 1987, Reyes and Jensen, 1984) have been put forward to deal with these reactions, but it is always assumed that some expression for the gas diffusivity in the pore elements is known.

To more fully utilize the current porous solid technology, and to possibly open new vistas for its application, it is important to try to understand, at the molecular level, the nature of these transport and reaction processes. Hence, much effort is spent in understanding the reaction mechanisms of heterogeneous catalysis. For reactions involving porous solids, the internal transport of fluids also demands an equal level of understanding but proves to be almost as tasking. The diffusion process depends not only on the physical properties of the gas, but also those of the solid, the geometry and topology of the porous network, and the prevailing process conditions. The text of Kärger and Ruthven (1992) provides an excellent

review of the various diffusion regimes that exist as a result of the interplay of these variables.

In this thesis one small aspect of this vast field is considered - diffusion in mesoporous solids. In particular we concentrate on the pore diameter range of 40Å to 20Å. In this limit, for most practical problems, gas transport is by free molecular flow or Knudsen diffusion. Free molecular flow results when the mean free path of the fluid molecules is very large in comparison with the pore diameter. As a result the molecules mostly collide with the pore surface and very rarely interact with each other. In 1909 Knudsen put forward an expression for the diffusivity of rarefied gases in infinite cylindrical capillaries

$$D_K = \frac{2}{3} r_p \sqrt{\frac{8kT}{\pi m}} \qquad (1.1)$$

where r_p is the pore radius, and the radical represents the average molecular speed. Though the assumptions in its derivation are particularly restrictive, it is almost universally used to describe free molecular flow in pores. Here we try to gain more insight into diffusion in mesoporous glass by experimental methods and molecular dynamics simulations.

The aims of Chapter 2 are twofold. Experimental permeation measurements are presented for a variety of gases in mesoporous glass subjected to incremental pore narrowing by silica deposition. In addition to providing information for an interesting regime of pore sizes (namely the transition region between micropores and mesopore), the permeance data also allows the evaluation of the transport models typically used for inferring the effective diffusivity of gases in dynamic mesopore structures. A prediction is made for the evolution of the permeance with the degree of deposition using the effective medium approximation

(Burganos and Sotirchos, 1987) to treat the effect of network topology and an expression by Clausing (Kennard, 1938) for Knudsen diffusion in capillaries of finite aspect ratio.

The Knudsen diffusivity formula is based on several assumptions that are arguably unrealistic in mesoporous materials. In particular the pore is assumed to be cylindrical and infinite, the effect of the intrapore force field on trajectories is ignored and the reflection of molecules from the pore surface is assumed to follow the cosine law of reflection (Present,1958). The more advanced form of equation (1.1) due to Smoluchowski, which relaxes the assumption of circular cross-section, is the furthest one can go in presenting a simple analytical form for the diffusivity (Kennard, 1938). To account for diffusion in non-capillary type structures such as elbow shapes, one must eventually resort to molecular dynamics or Monte Carlo analyses (Talley and Whitaker, 1969). In the last two decades such techniques were used by Nicholson and Petropoulos (1979,1981 and 1985) to incorporate the effect of the intrapore potential on the trajectories of the molecules. Chapter 3 describes the methodology for and the results of the molecular dynamics simulation of free molecular flow in mesoporous glass. Here we concentrate on two influences on the diffusion coefficient, the intrapore potential and the pore surface. The effect of the intrapore potential on diffusion has been studied by other investigators (Nicholson and Petropoulos, as well as Brodka and Zerda, 1991), but we include the new aspect of pore roughness. Simulations of fluids in confined geometries have been of great interest in recent years (Cracknell *et al.,* 1995), but more often than not the concern has been with high pressure fluids. Though such problems are complicated in themselves, the effect of the gas-surface interaction only has minor effects on the equilibrium properties sought and the cosine law of reflection is adequate. In free molecular flow problems however the method used for the treatment of the gas-surface interaction has a strong influence on the diffusivity. By using a specular reflection condition in our simulations (i.e., no energy transfer between the gas and solid) we examine the nature of this dependency.

Bibliography

Cracknell, R.F., Nicholson, D., Gubbins, K.E., 1995, Molecular Dynamics study of the Self-diffusion of Supercritical Methane in Slit-shaped Graphitic Micropores, *J. Chem. Soc. Faraday, Trans.*, **91**(9), 1377-1383

Kärger, J., Ruthven, D.M., *Diffusion in Zeolites and Other Microporous Materials*, John Wiley & Sons, Inc., New York, (1992)

Kennard, E.H., 1938, *Kinetic Theory of Gases*, 1st edn, McGraw-Hill Book Company, New York

Levenspiel, O., 1972, *Chemical reaction Engineering*, 2nd Edn, John Wiley & Sons, New York

Nicholson, D., Petrou, J., Petropoulos, J.H., 1979, Calculation of the Surface Flow of a Dilute Gas in Model Pores from First Principles: 1. Calculation of Free Molecule Flow in an Adsorbent Force Field by Two Methods, *J. Colloid Interface Sci.*, **71**(3), 570-579

Nicholson, D., Petropoulos, J.H., 1981, Calculation of the Surface Flow of a Dilute Gas in Model Pores from First Principles: 2. Molecular Gas Flow in Model Pores as a Function of Gas-Solid Interaction and Pore Shape, *J. Colloid Interface Sci.*, **83**(2), 420-427

Nicholson, D., Petropoulos, J.H., 1985, Calculation of the Surface Flow of a Dilute Gas in Model Pores from First Principles: 3. Molecular Gas Flow in Single Pores and Simple Model Porous Media, *J. Colloid Interface Sci.*, **106**(2), 538-546

Present, D.R., 1958, *Kinetic Theory of Gases*, 1st edn, McGraw-Hill Book Company, New York

Reyes S., Jensen, K.F., 1985, Estimation of Effective Transport Coefficients in Porous Solids based on Percolation Concepts, *Chem. Engng Sci.*, **40**(9), 1723-1734

Talley, W.K, Whitaker, S., 1969, Monte Carlo Analysis of Knudsen Flow, *J. Comp. Phys.*, **4**, 389-410

Yu, H., Sotirchos, S.V., 1987, A Generalized Pore Model for Gas-Solid Reactions Exhibiting Pore Closure, *A.I.Ch.E. J.*, **33**(3), 382-393

Chapter 2

Gas Transport in Porous Vycor Glass Subjected to Gradual Pore Narrowing

Submitted to *Chem. Engng Sci.*

Gas Transport in Porous Vycor Glass Subjected to Gradual Pore Narrowing

Neil E. Fernandes and George R. Gavalas
Chemistry and Chemical Engineering Division
California Institute of Technology
Pasadena, CA 91125

Abstract

Porous Vycor® glass was modified by deposition of silica on the internal pore surface using consecutive cycles of liquid phase silylation with silicon tetrachloride, and hydrolysis. Macroscopically uniform deposition was achieved by exploiting the self limiting nature of the reaction and the extent of deposition was monitored by the weight change of the samples. Weight increases as high as 24% were recorded and the average pore diameter was estimated to decrease from ~44Å to ~20Å. Permeation measurements were conducted in the Henry's law region at various levels of deposition for hydrogen, methane, isobutane and nitrogen, at temperatures between 60°C and 180°C. The measurements were compared to values calculated with a model using the effective medium approximation to treat network effects and Clausing's correction to account for conductances in pores of finite aspect ratio. The calculated values proved to be inaccurate for hydrogen, overestimating the permeance by a factor of 2 at high levels of deposition possibly because of non-ideal pore shapes accentuated by the deposition. For nitrogen and methane the agreement between calculations and measurements was better due to a fortuitous cancellation of deviations caused by the enhanced potential energy well within the pores and the non ideal pore shape. The intrapore potential energy effect was especially strong for isobutane and as a result the calculated flux was always less than the experimental.

2. 1 Introduction

Chemical reactions involving porous solids are ubiquitous in petroleum, chemical and materials processing industries. The reacting solids, be they catalyst, sorbents or solid reactants, undergo considerable physical change during reaction. In the common example of flue gas desulfurization by porous lime

$$CaO_{(s)} + SO_{2(g)} + \tfrac{1}{2}O_{2(g)} \rightarrow CaSO_{4(s)}, \tag{2.1}$$

the solid product has a molar volume more than three times that of the lime reactant. Therefore, as the reaction proceeds the pore radii shrink and diminishing network connectivity results in low solid conversions. The porous calcium oxide under these conditions is characterized as having a dynamic pore structure. Other examples of processes involving dynamic pore structures include char gasification and inorganic membrane formation in porous supports. In char gasification, as solid carbon is depleted, the pores become enlarged and eventually fragmentation takes place at the percolation threshold. Fluid-solid reactions in porous solids undergoing structural changes have been reviewed, among others, by Sahimi *et al.* (1990).

The problem of concern in this paper can be introduced by considering the equations governing reaction and diffusion in a spherical porous particle:

$$\frac{1}{y^2}\frac{\partial}{\partial y}\left[y^2 D_{\text{eff}}(X)\frac{\partial c}{\partial y}\right] = br(c,T)f(X) \tag{2.2}$$

$$\frac{\partial X}{\partial t} = f(X)r(c,T) \tag{2.3}$$

Here both the local reaction rate and the effective diffusivity vary with the extent of reaction and, as a first approximation, it is convenient to characterize the structure by a single

variable such as the conversion X. The rate factor, $f(X)$, can be obtained from reaction experiments carefully performed in the kinetically controlled regime. The effective diffusivity D_{eff} is also a function of the local extent of reaction but is more difficult to measure. In fact, there is little or no data for $D_{eff}(X)$ of common materials such as lime and coke. Lacking direct diffusivity data various authors, in order to solve equations (2.2) and (2.3), have resorted to estimating $D_{eff}(X)$ from capillary models. Starting with an initial measured pore size distribution, the common approach is to estimate the pore size distribution for different conversions and from this calculate the diffusion coefficient. The latter calculation must consider geometric effects at a single pore level as well as network effects. Networks effects can be taken into account by methods such as the effective medium approximation (EMA, Burganos and Sotirchos, 1987). However, the geometry of the network elements - the pore segments - is uncertain and the change of the conductances of these pores is not experimentally accessible. For example in the limit of free molecular flow, Knudsen's equation for diffusion in infinite cylindrical capillaries is almost always assumed. By relating then the pore radius, a, to conversion of the solid, one can obtain a value for D_{pore}, the diffusivity of the dilute gas within a single pore, and ultimately through the EMA calculate $D_{eff}(X)$. The main uncertainty in this predictive scheme lies in the parameterization of the element conductances rather than in the treatment of network effects.

In this paper direct experimental measurements of permeance are provided at different extents of pore narrowing. By carrying out pore altering reactions in the kinetically controlled regime, spatially *uniform* conversion, at the macroscopic level, can be achieved throughout the porous material. The effective diffusivity can then be measured at various levels of conversion and an experimental relationship between D_{eff} and X established. The material in this study is Vycor glass (Corning code 9310) made by spinodal decomposition of a silica-boria-sodium oxide melt and subsequent leaching of the boria-rich phase. This

mesoporous glass has a particularly narrow pore size distribution. The pores are approximately cylindrical with diameters in the range of 40-50Å and are well connected. Other pertinent data for Vycor are given in Table 2.1. In pores of this size and at pressures of ~1 atm, free molecular flow is prevalent and the Knudsen diffusion model is appropriate. Most importantly Vycor admits reactions enabling pore closure. Tsapatsis *et al.* (1991) carried out chemical vapor deposition (CVD) of silica in the pores of Vycor to make inorganic membranes for hydrogen separation by reacting gas phase silicon tetrachloride, $SiCl_4$ and water vapor with the pore surface. By carrying out the reactions with $SiCl_4$ (silylation) and H_2O (hydrolysis) sequentially rather than simultaneously, it is possible to ensure uniform deposition throughout the substrate. This scheme has also been used for membrane fabrication (Kim and Gavalas, 1993).

The permeance data obtained after different extents of deposition provide useful information concerning the transport behavior of dilute gases in mesopores of 2-4nm diameter. The temperature effect on dilute gas behavior in untreated porous Vycor has been experimentally investigated by Hwang and Kammermeyer (1966). Using a pore closing reaction, we are here able to address the effects of *pore size* on dilute gas transport. In addition to supplying information for this important range of pore sizes, the permeation data provided here are useful in ascertaining the predictive capability of capillary network models of porous solids undergoing structural change.

2.2 Experimental

Silica deposition on the pore surface of Vycor can be described by the reactions of silylation, hydrolysis and condensation as follows:

Silylation $$SiCl_4 + HO- \rightarrow Cl_3SiO- + HCl \qquad (2.4)$$

Hydrolysis $H_2O + Cl_3SiO- \rightarrow HOSiCl_2O- + HCl$ (2.5)

Hydrolysis $Cl_3SiO- + HO- \rightarrow -OSiCl_2O- + HCl$ (2.6)

Condensation $(HO)_3SiO- + HO- \rightarrow -O(HO)_2SiO- + H_2O$ (2.7)

where the hyphens in the above equations indicate surface species. A more detailed examination of these and other reactions occurring on the Vycor surface was reported by Kim and Gavalas (1993).

To avoid spatial gradients of the deposit layer caused by diffusional resistances, reactions (2.4)-(2.7) are not carried out simultaneously; rather the reactants are admitted sequentially to the reaction chamber in a cyclical fashion so that the pore surface is first silylated by $SiCl_4$ (equation 2.4), purged under nitrogen, and then hydroxylated by water (equation 2.5) before being purged again. This process can be applied as many times as is necessary to build up a sufficient deposit on the pore surface. As only one reactant is admitted to the reactor at a time, the reaction is self limiting and uniform deposition is ensured by allowing sufficient time for completion of the reaction. Each complete reaction cycle produces, at most, one molecular layer. This layer is uniform at the macroscopic level but not the microscopic; deposition actually occurs in clumps centered around the original silanols. As the clumps grow and overlap, some smoothing of the deposit layer is anticipated. The deposition reactions, equations (2.4) and (2.5), can be performed either in the gas phase or in the liquid phase. Both variations have been used in our investigations, but only data obtained with liquid phase deposition are presented here. Silicon tetrachloride is a very volatile liquid at ordinary temperatures and reacts violently with water. To avoid leaks and premature hydrolysis by atmospheric humidity, all reactions involving $SiCl_4$ were performed in a dry box under an argon atmosphere at room temperature. Initially a number of 30mm Vycor tubes (outside diameter 8mm, wall thickness 1mm) and a Vycor test piece

were rehydroxylated by boiling in water for ten hours. The tubes were subsequently washed in acetone for 24 hours before being dried for 24 hours at 180°C under vacuum to ensure the removal of physisorbed water and light organic contaminants. Some loss of silanols also took place under this treatment. The Vycor was subsequently silylated in a stirred solution of $SiCl_4$ in dry acetone (~15ml $SiCl_4$ to 300ml acetone) for 24 hours, washed in dry acetone for several hours, and hydrolyzed in water for ~15 hours. The final step in each cycle was to dry the Vycor under vacuum at 200°C. This procedure represented a single reaction cycle and caused the deposition of a single molecular layer of silica. Between cycles the Vycor test piece was weighed, the weight change being an indication of the level of deposition. A number of the samples were removed at this stage for further analysis. The deposition cycle was repeated five more times. Figure 2.1 shows the cumulative weight gain of the tubular Vycor samples. After six depositions of silica the porous glass became susceptible to fracture, possibly because of internal stresses caused by the deposited film. Nitrogen adsorption porosimetry was performed on the treated Vycor samples.

The permeances of gases through the different samples were measured using the simple pressure rise method illustrated in Figure 2.2. The 30mm Vycor tubes are sealed at one end to a Pyrex disc, and at the other end to a Pyrex tube. The sealant used was Torr-seal® by Varian, which can stand temperatures up to ~200°C. A vacuum was drawn on the inside of the tube while the gas under investigation was allowed to flow around the outside of the tube at the desired pressure - in most cases 210 Torr. The vacuum was then isolated from the inside of the tube and the time required for a pressure rise of ~1 Torr measured. The pressure was recorded using an MKS Baratron (0-10 Torr). Using the ideal gas law, the rate of pressure change is easily converted into a molar flux. The permeances of hydrogen, nitrogen, isobutane and methane were measured through each of the treated samples up to a weight increase of 19.8% at temperatures of 60°C, 120°C and 180°C. Unfortunately, the

21.2% samples fractured before any permeation measurements could be undertaken. The measured permeances of nitrogen and hydrogen through untreated Vycor compare favorably with those made by Hwang and Kammermeyer (1966).

2.3 Capillary Network Model

For the purpose of predicting the permeance evolution, the porous glass is represented as a network of finite capillaries of discrete diameters, with the network connectivity being represented through the pore coordination number, z, set equal to 6. The relatively narrow initial pore size distribution was modeled as comprising the three modes of pore size given in Table 2.2. The frequencies were chosen so as to match volume fractions found by porosimetry for each pore size range. The surface area to pore volume ratio using these frequencies also matched the experimental value of 0.09 $Å^{-1}$ inferred from porosimetry. To calculate D_{eff} it is necessary to examine the respective contributions of the network topology and pore geometry (pore conductance). The most accurate procedure to account for network effects in porous structures far from the percolation threshold is the effective medium approximation (EMA) employed by Burganos and Sotirchos (1987). The EMA technique is used to map the network of distributed conductances g_i onto a network of the same effective diffusivity which has pores of a single conductance g_e. The effective diffusivity of this uniformly sized equivalent network can be easily and exactly calculated, assuming knowledge of the individual element conductances. For the trimodal approximation of Vycor, EMA gives the following equation for the pore conductance g_e of the equivalent network

$$\frac{g_1 - g_e}{g_1 + \frac{z-1}{2} g_e} + \frac{g_2 - g_e}{g_2 + \frac{z-1}{2} g_e} + \frac{g_3 - g_e}{g_3 + \frac{z-1}{2} g_e} = 0 \qquad (2.8)$$

The effective diffusivity can then be expressed as

$$D_{\text{eff}} = \frac{K g_e l^2}{3} \tag{2.9}$$

where K is the number of pore segments per unit volume.

In the free molecular flow regime, the pore conductance is a function of the pore shape which is very difficult to characterize mathematically. Payatakes and Burganos (1992) have used Monte Carlo simulations to calculate conductances in relatively complex pore geometries, but their results are not directly applicable since typically the only geometrical information available is the pore size distribution and possibly the average pore length. In the present analysis the pores are assumed to shrink in a concentric, or conformal, fashion preserving an initial cylindrical geometry. Any effects of the intra-pore potential field have also been ignored. With these simplifying assumptions the following formula for conductance is applicable.

$$g(l/a) = \frac{20 + 8(l/a)}{20 + 19(l/a) + 3(l/a)^2} \frac{\pi a^2 u_{\text{av}}}{4} \tag{2.10}$$

The first factor in equation (2.10) attempts to capture the effect of finite aspect ratios of cylindrical pores. It is a semi-empirical expression for the transmission probability through the pore based on the work of Clausing (Kennard, 1938). Although there is no one-to-one correspondence between transmission probability and conductance, equation (10) provides a rough correction for the effect of aspect ratio.

In order to apply equation (2.10), an estimate of the pore aspect ratio is required. The only experimental information available for this purpose is the fractional weight change after deposition and to convert this information into a pore radius an estimate of the deposit

density is required. An experiment was performed whereby the deposition procedure was applied up to a weight change of 24% when no more mass increase could be obtained. With the assumption that network connectivity breaks down (as far as the diffusion of $SiCl_4$ is concerned) when the pore radii of the smallest two modes (19.75 and 22.5Å) are reduced to ~7.5Å, the average density of the deposit is estimated to be ρ_{exp}~1.45 gcm^{-3} by using the expression

$$\frac{\Delta w}{w} = \frac{\alpha \rho_{exp}}{\rho_{app}} \frac{\sum_i \left(a_i^2 - (a_i - t)^2\right) n_i}{\sum_i n_i a_i^2} \qquad (2.11)$$

Using this density it is straightforward to calculate the thickness of the deposit layer, t, and hence the pore radii at each level of deposition. To complete the calculation of pore conductance by equation (2.10), an average pore length of 120Å was adopted. In a trivial way one can also account for the finite size of the diffusing molecules by further defining the pore radius at any time to be a-σ/2-t.

2.4 Results

Figure 2.1 illustrates the cumulative weight gain of the Vycor samples during the pore narrowing process. In the network model it has been assumed that these films grow in a conformal fashion, maintaining the initial cylindrical pore shape. Figure 2.3 gives the pore size distribution for the untreated sample and for samples after one and three complete reaction cycles, obtained by applying Kelvin's equation to the desorption branch of the nitrogen adsorption isotherm. Nitrogen adsorption porosimetry can only be used as a rough indication of the pore size distribution as capillary condensation is sensitive to the pore

shape, and as the pore radius decreases below 2 nm, the Kelvin equation becomes increasingly inaccurate.

For untreated Vycor, the experimental permeances and the permeances calculated by the EMA analysis of the capillary network are given in Table 2.3. The comparison is quite favorable for hydrogen, and in light of the minimal information used in the calculation, the agreement for nitrogen and methane is fair. Figures 2.4-2.6 illustrate how the reduced effective diffusivities evolve with deposition at temperatures of 180°C, 120°C and 60°C. In these figures the experimental and calculated permeances have been normalized with the permeances appearing in Table 2.3. The uncertainty in the measurements is of the same order of size as the symbols and so error bars have not been drawn. At any level of deposition, the aspect ratio, corrected for molecular size, is different for each gas and thus the calculated gas permeances deviate slightly from each other. The calculated hydrogen permeances in the treated Vycor deviate significantly from the experimental results at all temperatures. With increasing deposition, EMA overestimates the actual diffusivity, the deviation ultimately reaching a factor of ~2. Similar deviations are noticed for nitrogen and methane, however, as the temperature decreases the discrepancy between experiment and calculation becomes smaller. The opposite behavior is exhibited by isobutane. As the temperature decreases the deviations increase, the isobutane flux eventually being underestimated at high depositions by a factor of ~2.

The discrepancy between calculated and experimental permeances is more clearly illustrated in Figures 2.7 and 2.8 where the permeance, normalized with the Knudsen temperature and mass dependency, $(MT)^{1/2}$, has been plotted against the temperature for untreated and treated (19.8% weight gain) Vycor respectively. For true Knudsen diffusion all the data points would be expected to lie on the straight lines drawn on the figures. In Figure 2.7, the hydrogen permeance apparently follows the Knudsen temperature dependence while the

nitrogen and methane permeances show weak positive deviations. However, the isobutane permeance markedly departs from Knudsen behavior. Figure 2.8 shows further increases in deviations as the pores become narrower.

2.5 Discussion

It is clear from the foregoing discussion that the capillary network model does not accurately predict the evolution of diffusivity with increasing deposition, and the assumptions built into the model need to be reviewed. Firstly, to investigate whether the free molecular flow assumption is appropriate, the permeances of isobutane and nitrogen were measured for various pressure differences across the Vycor tube wall. In Figure 2.9 the permeances through a Vycor sample with 17.7% mass of deposited silica are seen to be constant over the pressure difference range of 0-300 Torr indicating that under these experimental conditions the molecules were almost certainly diffusing independently of each other.

In order to apply the standard network analysis, the pore space was described as a simple network of conductances, ignoring the finite size of the pore intersections (network nodes). The implication of this assumption is that the effects of network topology and pore conductance can be simply decoupled and that the individual pore conductances can be calculated from

$$g = \tfrac{1}{4} f\pi a^2 u_{av} \qquad (2.12)$$

where, as discussed previously, f is a transmission probability correction for the effect of aspect ratio. Burganos and Payatakes (1992) have remarked that the simple network models are satisfactory for low porosity media. As also indicated by the fair agreement

between calculated and experimental results for the untreated Vycor, the large permeance discrepancies observed in Figures 2.4-2.6 cannot be accounted for by the network representation of the pore space nor by the effect of the pore aspect ratio *per se*.

Of more consequence is the representation of the pores as finite cylindrical segments of some effective pore radius. Calculating the radius at different extents of deposition requires knowledge of the deposit density. Owing to the initially discrete arrangement of reactions sites the silica deposit is a highly defective material of density lower than the 2.0 gcm^{-3} typical of fused silica glasses. If a density of 2.0 gcm^{-3} was assumed for the deposit, and all pores were assumed to be completely blocked with silica, then based on the data in Table 2.1 a weight change of ~39% would be expected. Clearly such a gain could never be achieved because of the low density of the deposited silica and the finite size of the reacting $SiCl_4$ molecules (~5.8 Å). Permeance calculations using various deposit densities are illustrated for hydrogen at 180°C in Figure 2.10. It would appear that the best choice of density is ~1.25 gcm^{-3}. However, the assumption of conformal pore closing applied to the measured maximum mass gain of Vycor leads to an average deposit density of about 1.45 gcm^{-3}.

In addition to the uncertainty concerning the deposit density, the pore shape must also be considered. Even if the pores are initially cylindrical, they would generally deviate from this ideal shape with the progress of deposition. From the discussion on the mechanism of silica deposition, it can be argued that after the first deposition cycle, if not before, there must exist surface spatial heterogeneities at a length scale ~5Å. One can only speculate about the detailed nature of these perturbations, but it is likely that they will cause pore blocking at much earlier times than if the cylindrical shape persisted. Under the premise that pores close conformally, i.e., deposition is uniform at all length scales, the deposit density was estimated to be ~1.45 gcm^{-3}. If the deposit is allowed to grow in the form of clumps

(or as silica trees), then a higher density must be used, closer to the value of fused silica, ~2.0 gcm^{-3}. In this case the pore conductivity would be eventually interrupted not by total pore closure but by pore necking. This idea is more easily understood through a quantitative example, indicating the magnitude of the correction required to account for pore necking. For the purpose of illustration, deposition is assumed to close the pores in either of the two ways illustrated in Figure 2.11. Burganos and Payatakes (1992) subjected the sinusoidal pore in this figure to Monte Carlo analysis and calculated the effect of the dimensionless aperture size d/H on the pore diffusivity. Here the density for the cases of pore necking and conformal closing are denoted by ρ_n and ρ_c respectively and $\rho^*=\rho_n/\rho_c$. Since the deposit mass is the same in both cases, it can be shown from simple geometrical considerations that to be commensurate with the pore necking model, the pore aspect ratio for the conformal closing model must be

$$\frac{l}{a_{\text{eff}}}=\frac{2\sqrt{2}}{\sqrt{\frac{1}{2}(1-\rho^*)+\frac{3}{16}\rho^*\left(1+\left(\frac{d}{H}\right)^2\right)+\frac{1}{8}\rho^*\frac{d}{H}}} \qquad (2.13)$$

Using equation (2.10) it is a simple matter to obtain the conductance of cylindrical pore segments of this aspect ratio and ultimately obtain the correction illustrated in Figure 2.12 for different values of ρ^*. For instance, at $\rho^*=1.4$ (=2.0/1.45) the diffusivity in pores undergoing necking falls to zero at $2a_{\text{eff}}/H=0.33$. However, at this level of deposition the diffusivity obtained for conformal closing is still ~33% of its initial value. This correction is calculated for pores of initial aspect ratio 4 and cannot be strictly applied to the capillary network model where the pores range in initial aspect ratio from 4.5 to 6.1. Nevertheless, it is clear that pore necking reduces the network conductivity below that calculated for

conformal closing and offers a reasonable explanation for the overestimation of the permeances of hydrogen, nitrogen and methane.

Another assumption inherent in equation (2.10) is that the gas concentration inside the pores is equal to that of bulk gas outside of the solid. This assumption is restrictive in not taking into account the increase of the intrapore concentration due to the attractive force field of the solid. The intrapore concentration is generally described by the adsorption isotherm which in the limit of low concentrations is linear corresponding to the Henry's law regime. Under these conditions the flux can be described by incorporating Henry's constant, K_H, as a multiplicative factor in the customary expression of Knudsen diffusion. This partitioning effect is enhanced as the pore radii get smaller (Everett and Powl, 1976). The intra-pore potential also causes strong deviations from the linear trajectories assumed in Knudsen diffusion, with the result that the mean step size in the random walk is altered (Nicholson *et al.*, 1979, Nicholson and Petropoulos, 1981 and 1985). This path curvature effect is also used in kinetic gas theory to partially explain the variation of gas viscosity with temperature (Present, 1958). Characterizing the intrapore potential by the dimensionless parameters ε/kT and σ/a, the diffusivity might then be written down approximately as

$$D_{\text{pore}} = K_H(\varepsilon/kT, \sigma/a) K_\lambda(\varepsilon/kT, \sigma/a) f(1/a) u_{\text{av}} \qquad (2.14)$$

where K_λ is a correction factor for mean free path and it is assumed that the effects of the potential on concentration and mean free path can be separated. In the limit of high temperature, shallow potentials, or large pore sizes, K_H and K_λ become unity and D_{pore} tends to the diffusivity calculated from geometric considerations only.

By considering the effects of the intrapore potential, it is easy to explain the non-Knudsen temperature behavior evidenced in Figures 2.7 and 2.8. Referring to the Lennard-Jones parameters given for the gases in Table 2.5, isobutane is seen to be strongly adsorbing and its deviation from the predicted permeance is clearly due to its relatively large Henry's constant. Similarly, in Figure 8 the normalized permeance of methane is seen to be slightly higher than that of nitrogen while hydrogen shows little or no departure from Knudsen behavior, all in accord with the parameters in Table 2.4.

That the intrapore potential is enhanced as the pore radius decreases can be seen from the renormalized data in Figures 2.13-2.15. Here the data in Figures 2.4-2.6 have been replotted after first multiplying the permeances by $M^{1/2}$, to eliminate the effect of molecular mass, and then by normalizing the resulting permeances with the mass corrected hydrogen permeance to roughly eliminate the effects of pore shape. This latter interpretation is valid if the finite molecular sizes of the gases can be neglected and the mean free paths are assumed to be identical for all molecules. In this event the ordinate represents the combined effect of partitioning and path curvature on the permeance of a given gas relative to that of hydrogen. It is not possible to decouple the effects of partitioning and path curvature using simple permeation measurements, but the separate contributions can be estimated by molecular dynamics and Monte Carlo simulations using, for instance, the methodology expounded by Nicholson and Petropoulos (1981).

2.6 Conclusion

In this report experimental values of gas permeances have been presented for a material undergoing pore narrowing. Comparison of the experimental values with calculations using capillary network models show significant deviations that grow with decreasing pore size. In the Henry's law limit it has been demonstrated that several effects must be accounted for in order to make an accurate prediction of gas transport. The principal causes of the discrepancy are the deviations from the cylindrical pore geometry and the strong potential energy wells that exist in small pores.

2.7 Acknowledgments

The authors would like to acknowledge the DOE funding of this research through the University Coal Research Program, Grant DE-FG22-92PC92525.

2.8 Notation

Symbols not presented here are defined in the text.

Roman

a	pore radius, m
b	stoichiometric coefficient
c	gas concentration, mol m^{-3}
d	throat or aperture diameter in the pore necking model, m
D_{eff}	effective diiffusivity, m^2s^{-1}
D_{pore}	pore diffusivity, m^2s^{-1}
D_o	effective diffusivity in untreated Vycor (calculated or experimental), m^2s^{-1}
H	initial pore diameter, m
$f(X)$	structural factor relating reaction rate to level of conversion
f	transmission probability
g	conductance, m^3s^{-1}
K	number of pores per unit volume, m^{-3}
K_h	Henry's constant
K_λ	modifying factor for the mean step size
l	average pore length, m
M	molar mass, kg mol^{-1}
N	molar flux, cm^3 (25°C, 1atm) $cm^2min^{-1}atm^{-1}$
n	number frequency of pores of a particular size
ΔP	pressure difference across the samples
r	intrinsic reaction rate, s^{-1}
T	temperature, K
t	deposit thickness, m

u_{av} mean molecular speed, ms^{-1}

w initial sample weight, kg

Δw incremental weight change, kg

X fractional level of conversion

y radial position inside the solid pellet, m

z coordination number at pore network nodes

Greek

α void fraction

ε a measure of the depth of potential well in the pore, also the Lennard-Jones interaction energy, J

σ Lennard-Jones molecular diameter, m

Bibiography

Burganos, V.N., Payatakes, A.C., 1992, Knudsen Diffusion in Random and Correlated Networks of Constricted Pores, *Chem. Engng Sci.*, **47**(6), 1383-1400

Burganos, V.N., Sotirchos, S.V., 1987, Diffusion in Pore Networks; Effective Medium Theory and Smooth Field Approximation, *A.I.Ch.E. J.*, **33**(10)

Everett, D.H., Powl, J.C., 1976, Adsorption in Slit-like and Cylindrical Micropores in the Henry's Law Region, *J. Chem. Soc. Faraday Trans. I*, **72**(61), 619-635

Hwang, S.T., Kammermeyer, K., 1966, Surface Diffusion in Microporous Media, *Can. J. Chem. Engng*, **44**, 82-89

Kennard, E.H., 1938, *Kinetic Theory of Gases*, 1st edn, McGraw-Hill Book Company, New York

Kim, S., Gavalas, G.R., 1993, Kinetic Study of the Reactions of Chlorosilanes with Porous Vycor Glass, *J. Colloid Interface Sci.*, **161**(1), 6-18

Nicholson, D., Petrou, J., Petropoulos, J.H., 1979, Calculation of the Surface Flow of a Dilute Gas in Model Pores from First Principles: 1. Calculation of Free Molecule Flow in an Adsorbent Force Field by Two Methods, *J. Colloid Interface Sci.*, **71**(3), 570-579

Nicholson, D., Petropoulos, J.H., 1981, Calculation of the Surface Flow of a Dilute Gas in Model Pores from First Principles: 2. Molecular Gas Flow in Model Pores as a Function of Gas-Solid Interaction and Pore Shape, *J. Colloid Interface Sci.*, **83**(2), 420-427

Nicholson, D., Petropoulos, J.H., 1985, Calculation of the Surface Flow of a Dilute Gas in Model Pores from First Principles: 3. Molecular Gas Flow in Single Pores and Simple Model Porous Media, *J. Colloid Interface Sci.*, **106**(2), 538-546

Present, D.R., 1958, *Kinetic Theory of Gases*, 1st edn, McGraw-Hill Book Company, New York

Sahimi, M., Gavalas, G.R., Tsotsis, T.T., 1990, Statistical and Continuum Models of Fluid-Solid Reactions in Porous Media, *Chem. Engng Sci.*, **45**(6), 1443-1502

Tsapatsis, M., Kim, S., Nam, S.W., Gavalas, G.R., 1991, Synthesis of Hydrogen Permselective SiO_2, TiO_2, Al_2O_3, B_2O_3 Membranes from the Chloride Precursors, *I & EC Res.*, **30**, 2152-2159

Table 2.1 Physical Properties of Vycor (Corning code 7930)

Composition	96% SiO_2 , ~4%B_2O_3
Dry Apparent Density, ρ_{app}	1.48 gcm^{-3}
Void Fraction, α	0.28
Surface Area	200 $m^2 g^{-1}$
Average Pore Length	120 Å
Average Pore Diameter	40 Å

Table 2.2 Tri-modal pore size distribution used to describe the initial pore structure of Vycor glass

Pore Diameter /Å	Number Fraction	Volume Fraction
52.8	0.128	0.182
45.4	0.484	0.510
39.5	0.388	0.308

Table 2.3 Experimental and calculated permeances for untreated Vycor

	Permeance /cm^3(NTP)$min^{-1}cm^{-2}atm^{-1}$					
	180°C		120°C		60°C	
	Exp.	Calc.	Exp.	Calc.	Exp.	Calc.
Hydrogen	0.637	0.600	0.717	0.644	0.778	0.700
Methane	0.244	0.199	0.268	0.214	0.310	0.232
Nitrogen	0.195	0.152	0.209	0.163	0.237	0.177
Isobutane	0.175	0.094	0.229	0.101	0.299	0.110

Table 2.4 Lennard-Jones (6-12) parameters of gases used in the permeation measurements

Gas	ε/k /K	σ /Å
Hydrogen	30	2.87
Isobutane	338	5.34
Methane	140	3.82
Nitrogen	90	3.71

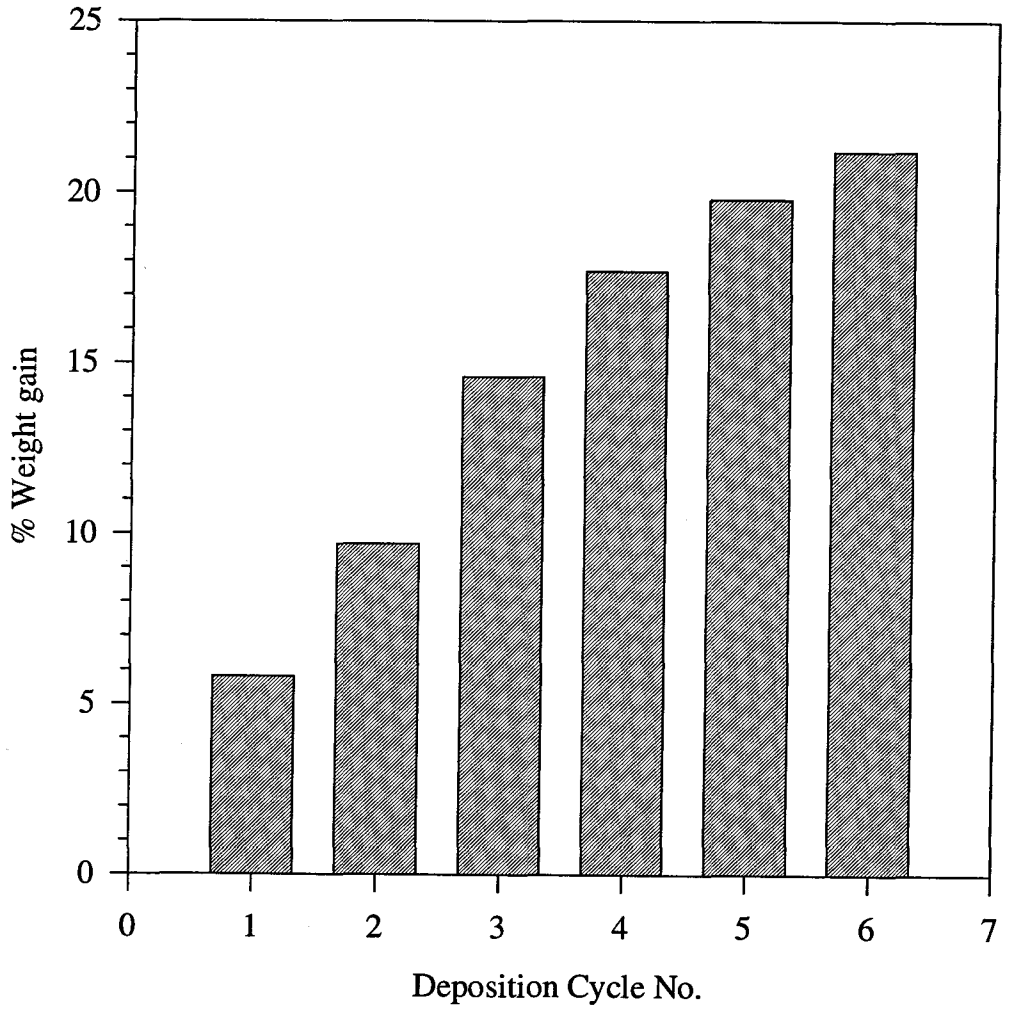

Figure 2.1 Cumulative weight gain of Vycor glass after each deposition cycle

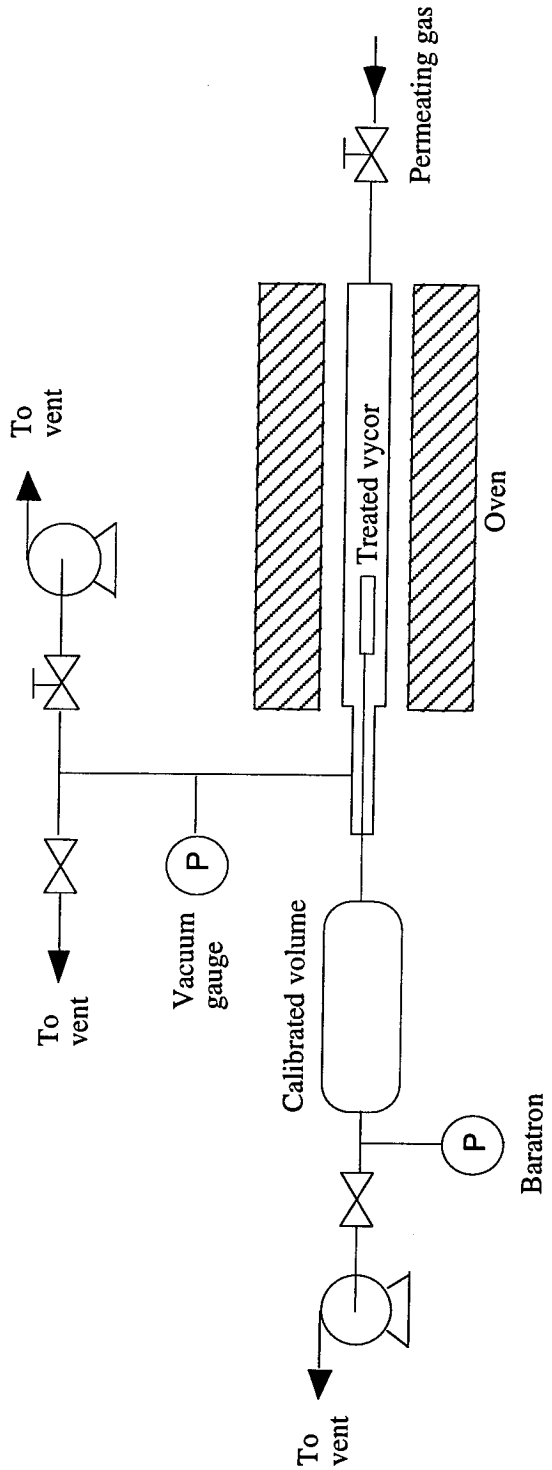

Figure 2.2 Apparatus for permeance measurements by the pressure rise technique

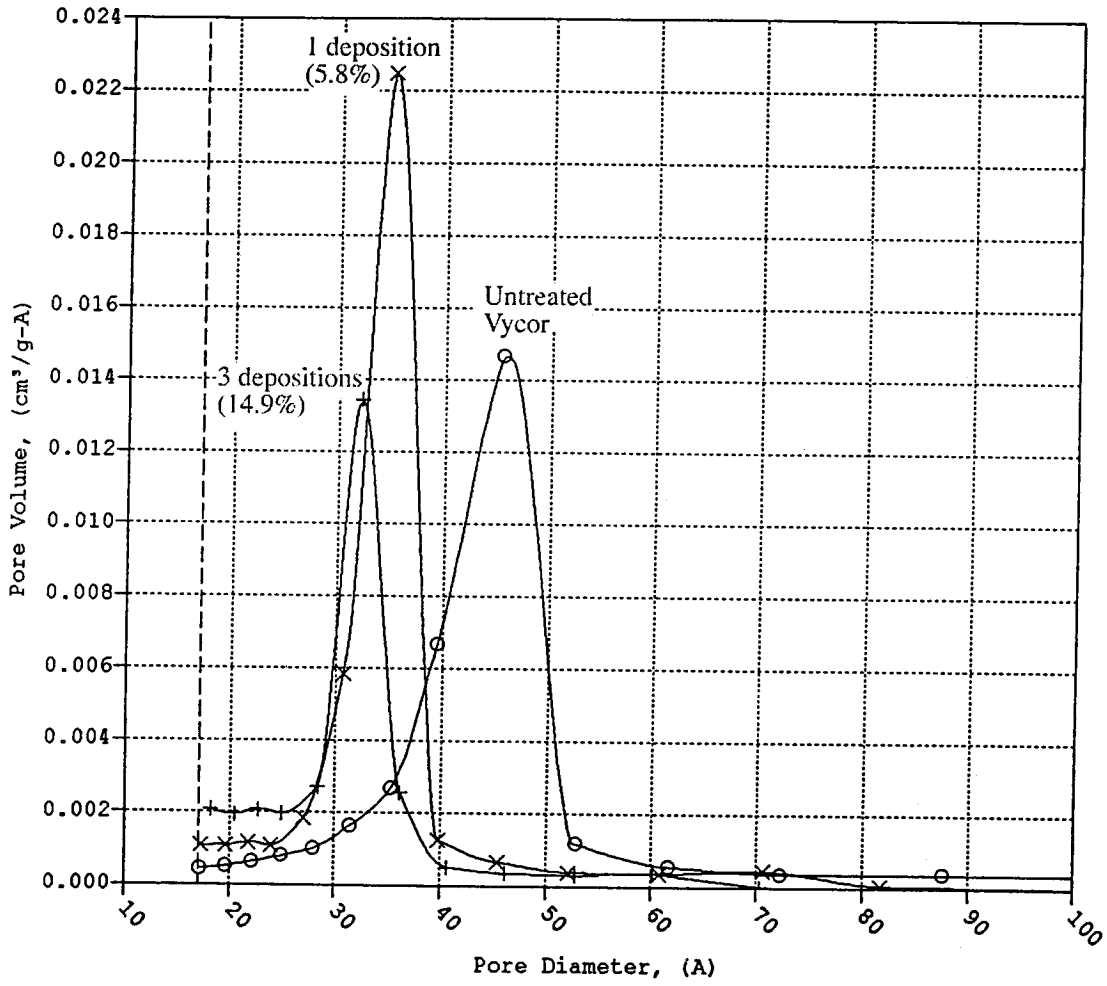

Figure 2.3 Pore size distribution of Vycor before and after deposition

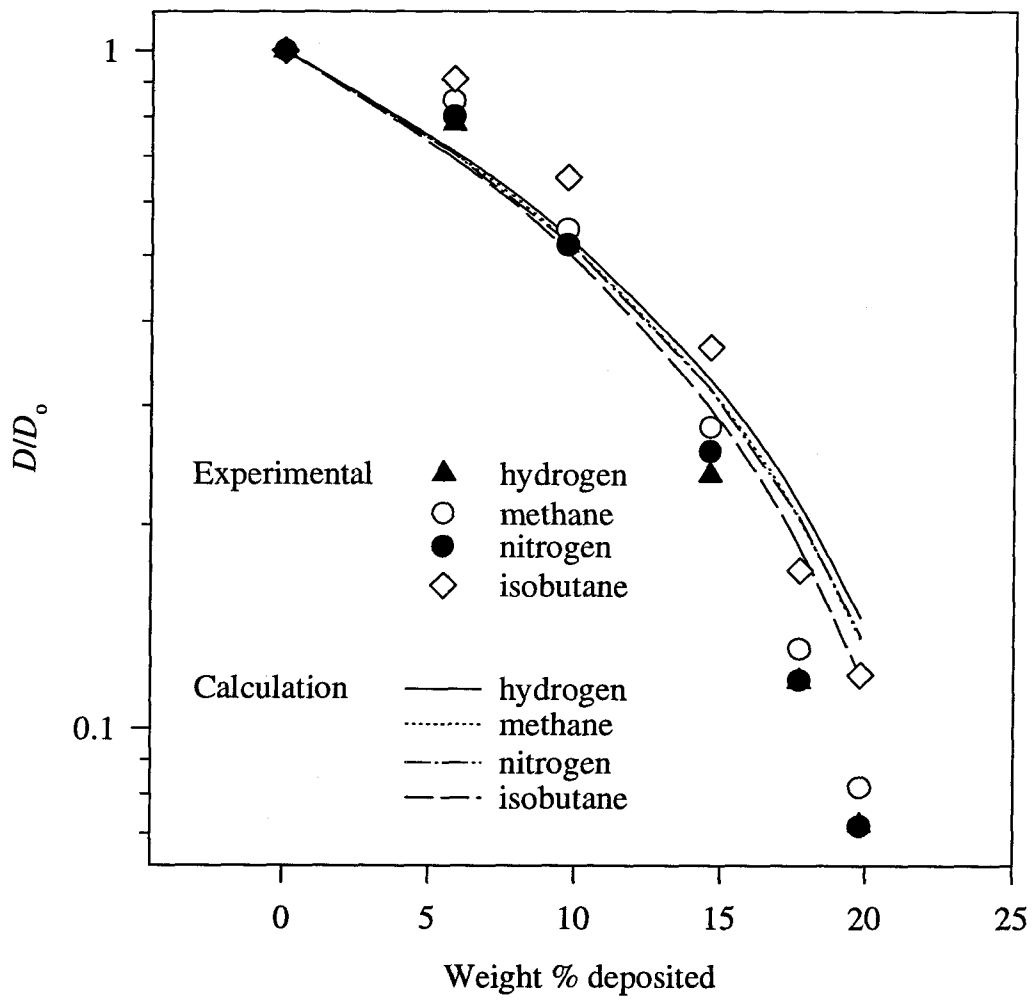

Figure 2.4 Normalized diffusivities of various gases vs extent of deposition at 180°C

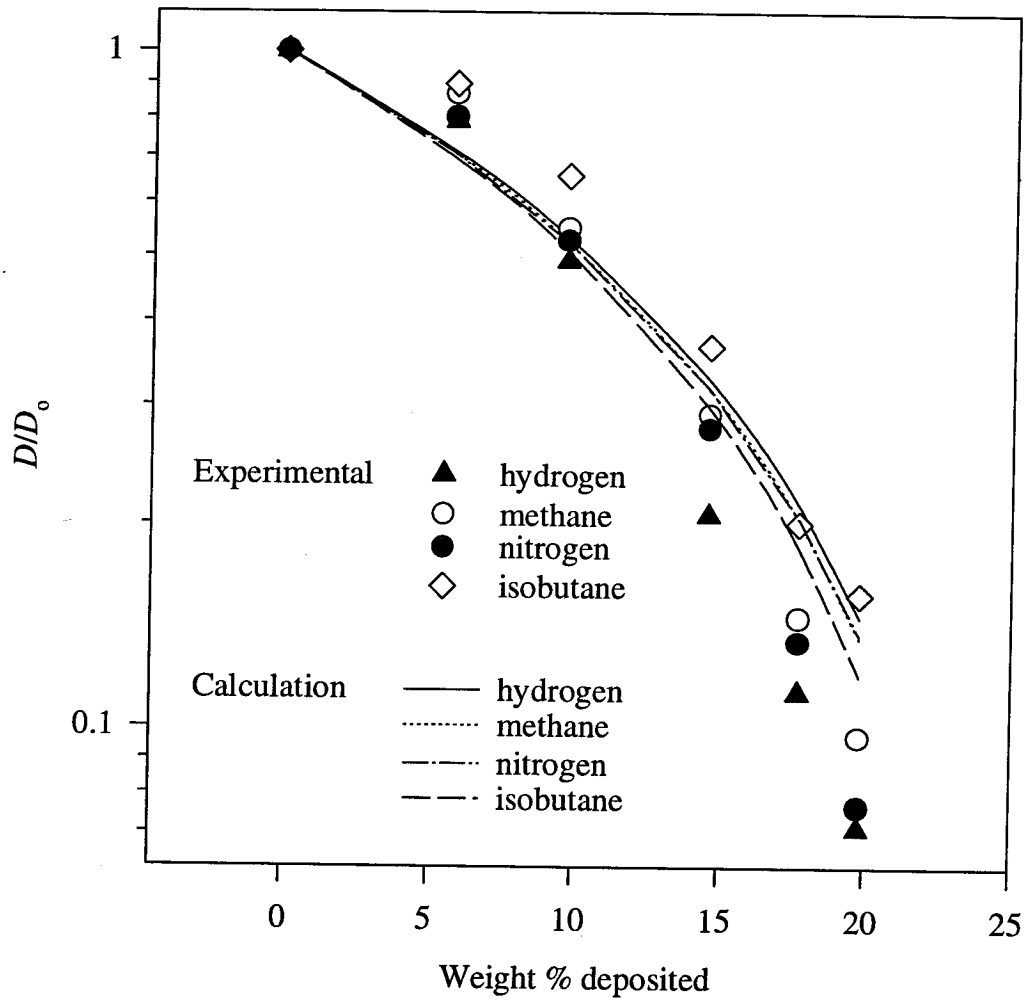

Figure 2.5 Normalized diffusivities of various gases vs extent of deposition at 120°C

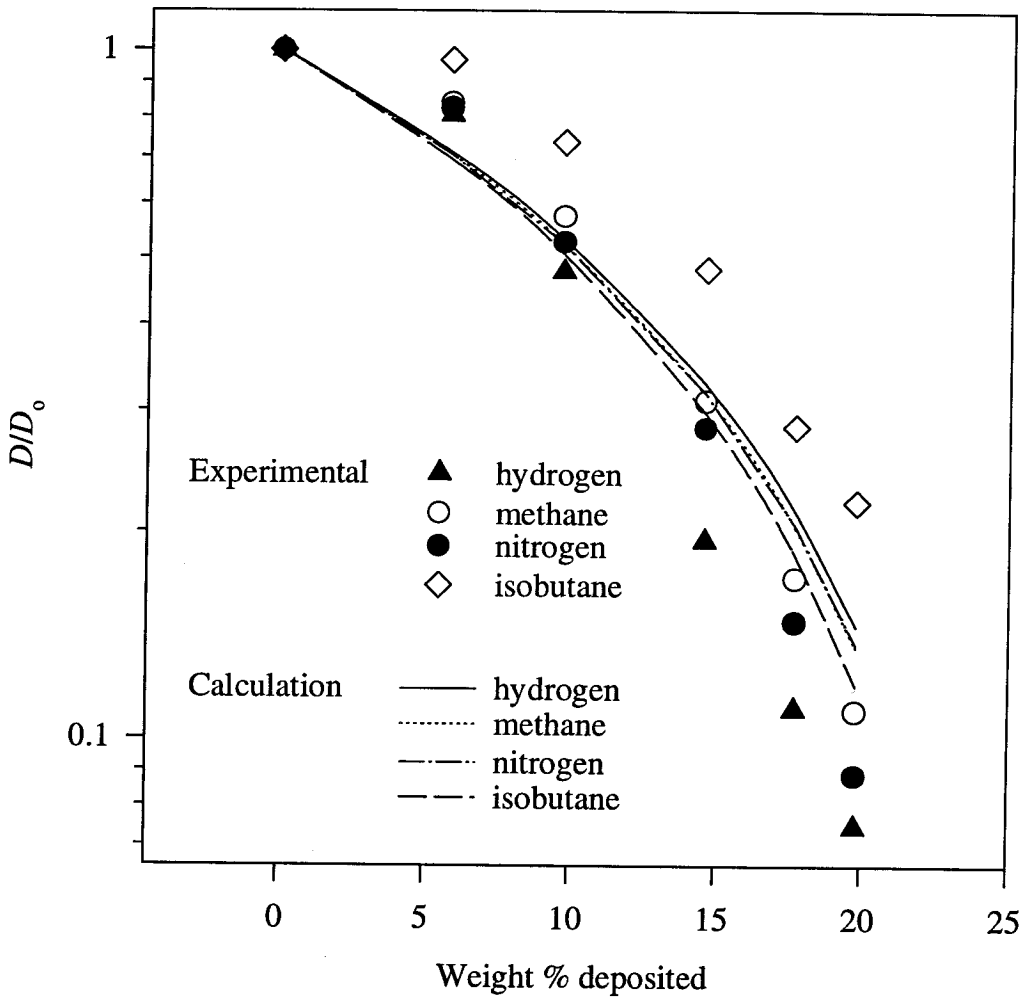

Figure 2.6 Normalized diffusivities of various gases vs extent of deposition at 60°C

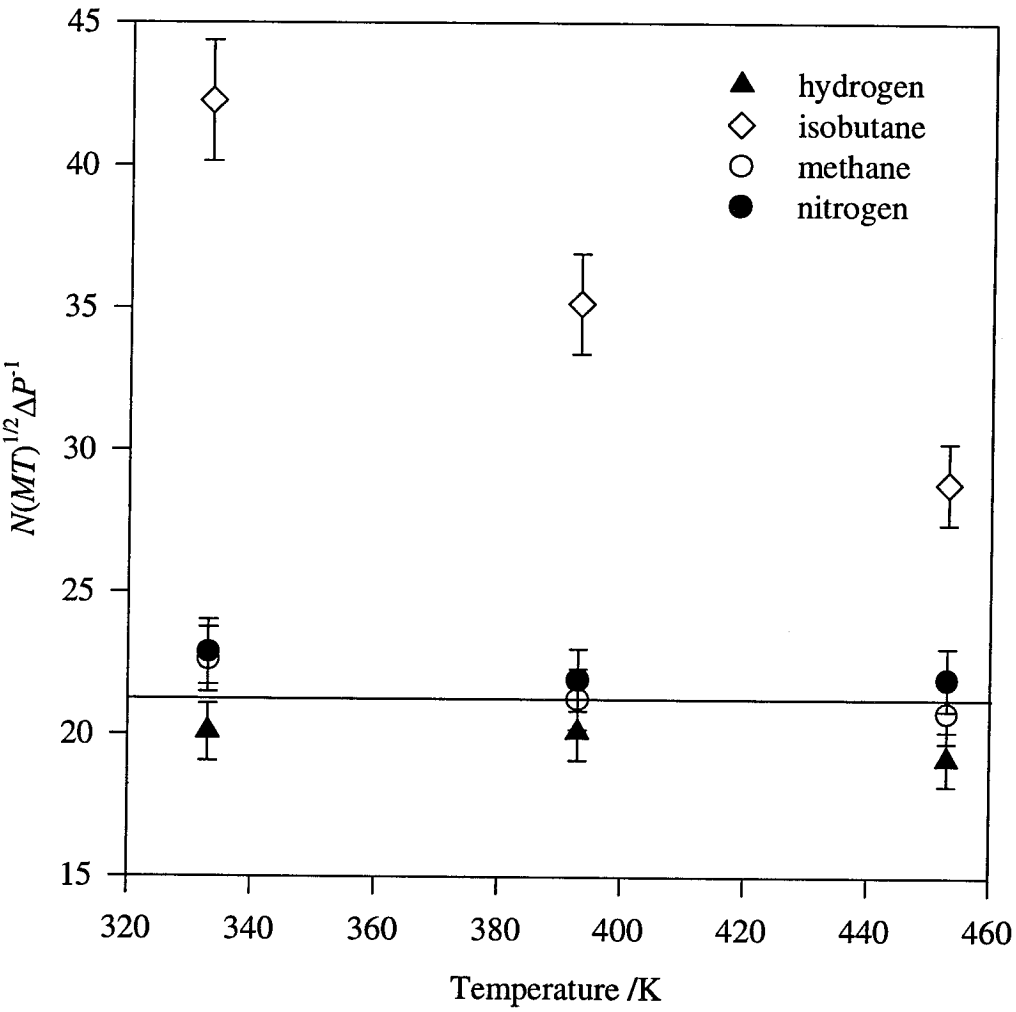

Figure 2.7 Normalized permeance of various gases through untreated Vycor vs temperature

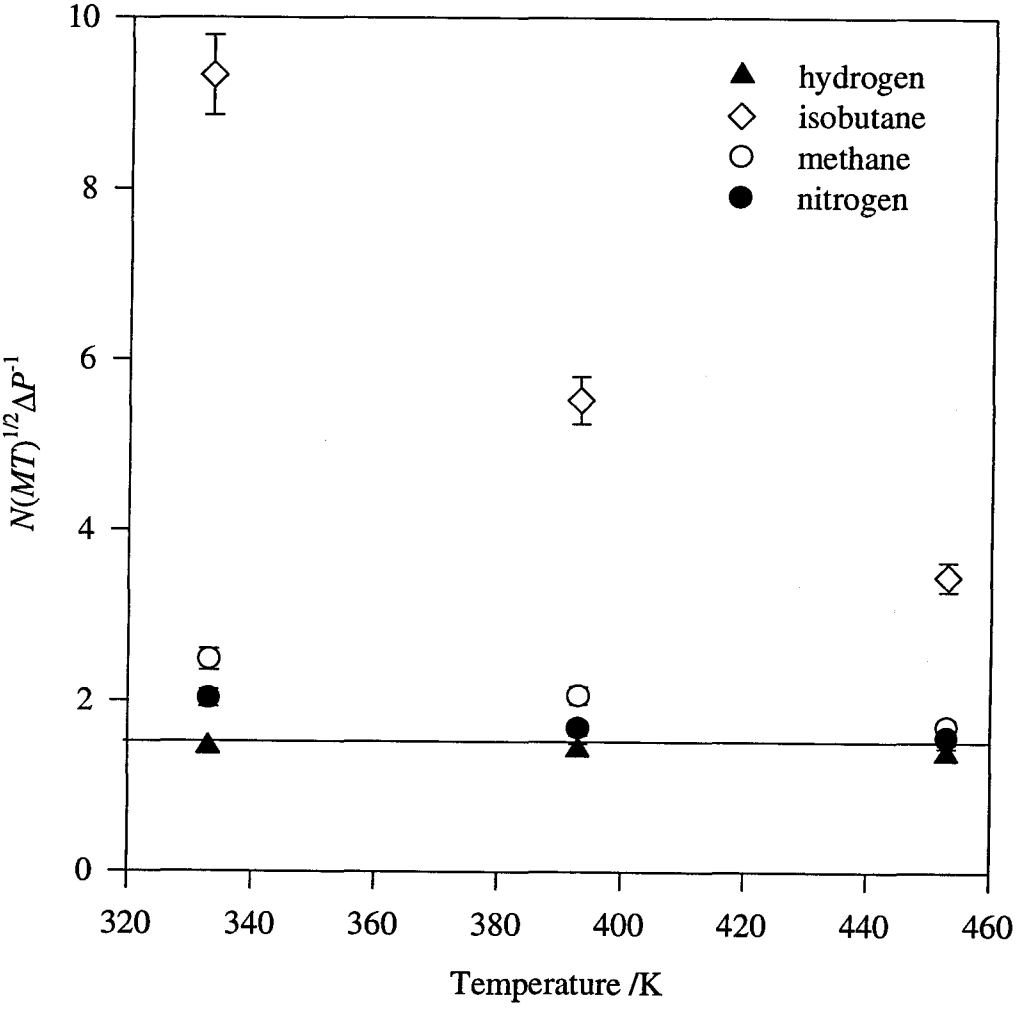

Figure 2.8 Normalized permeance of various gases through Vycor after 5 cycles of deposition (19.8 wt% gain) vs temperature

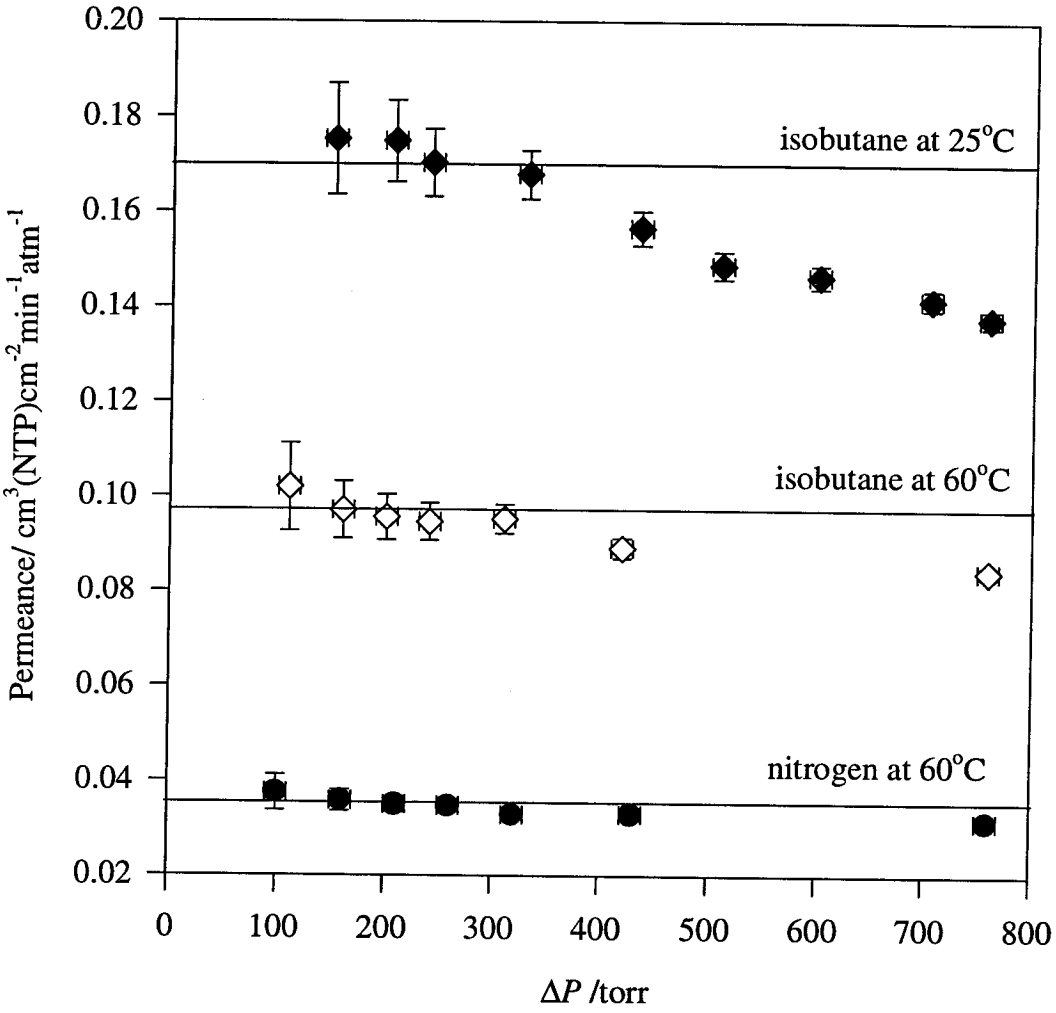

Figure 2.9 Effect of pressure difference on gas permeances

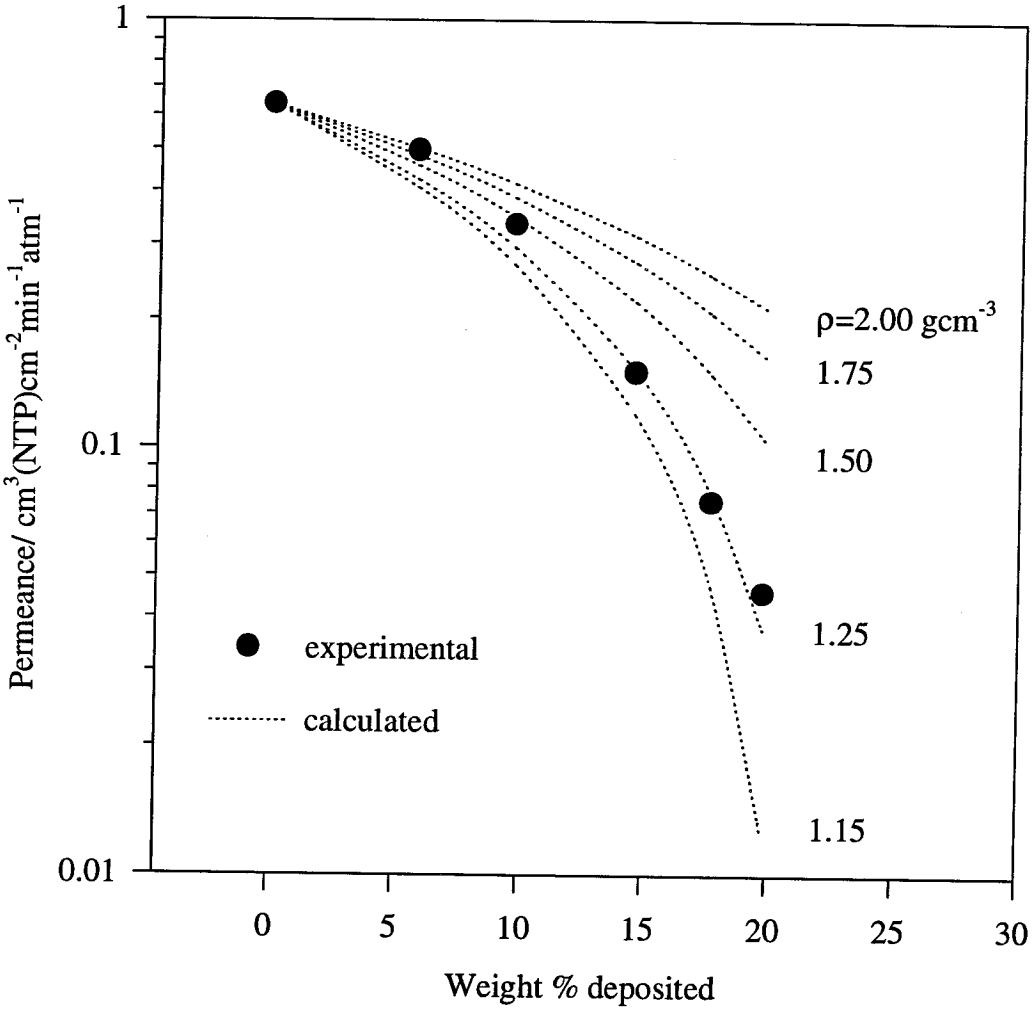

Figure 2.10 Experimental and calculated hydrogen permeances at 180°C for different assumed deposit densities

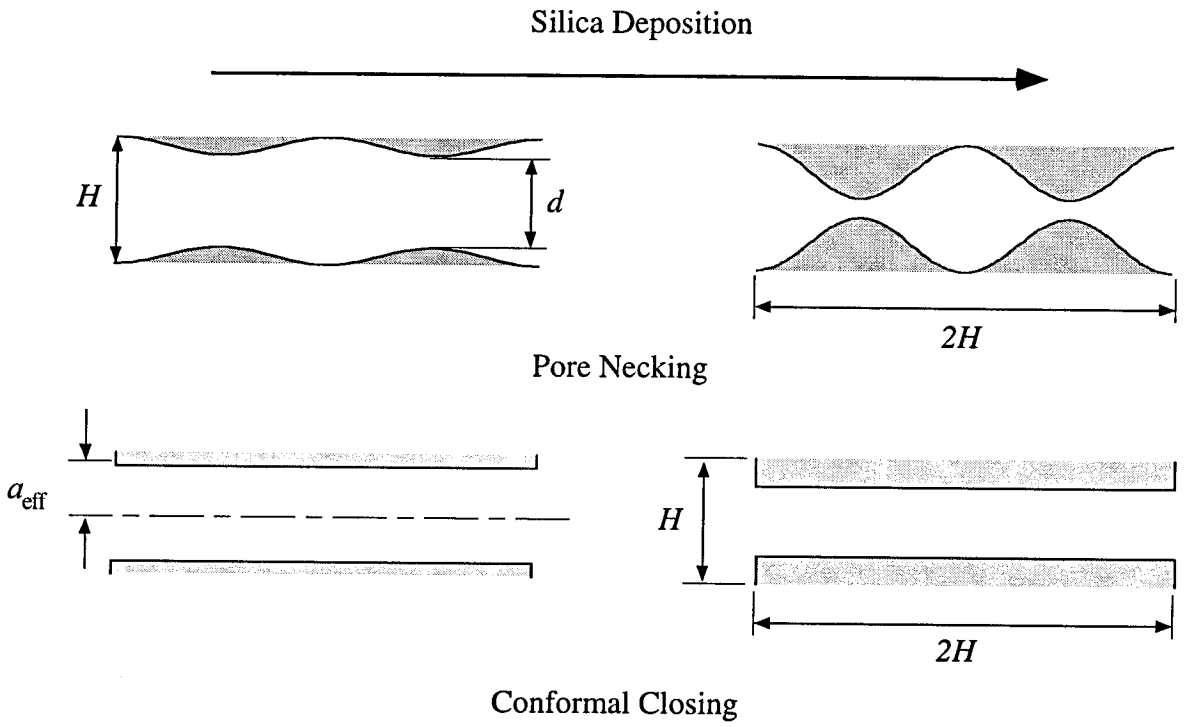

Figure 2.11 Conformal pore closing and pore closing by necking

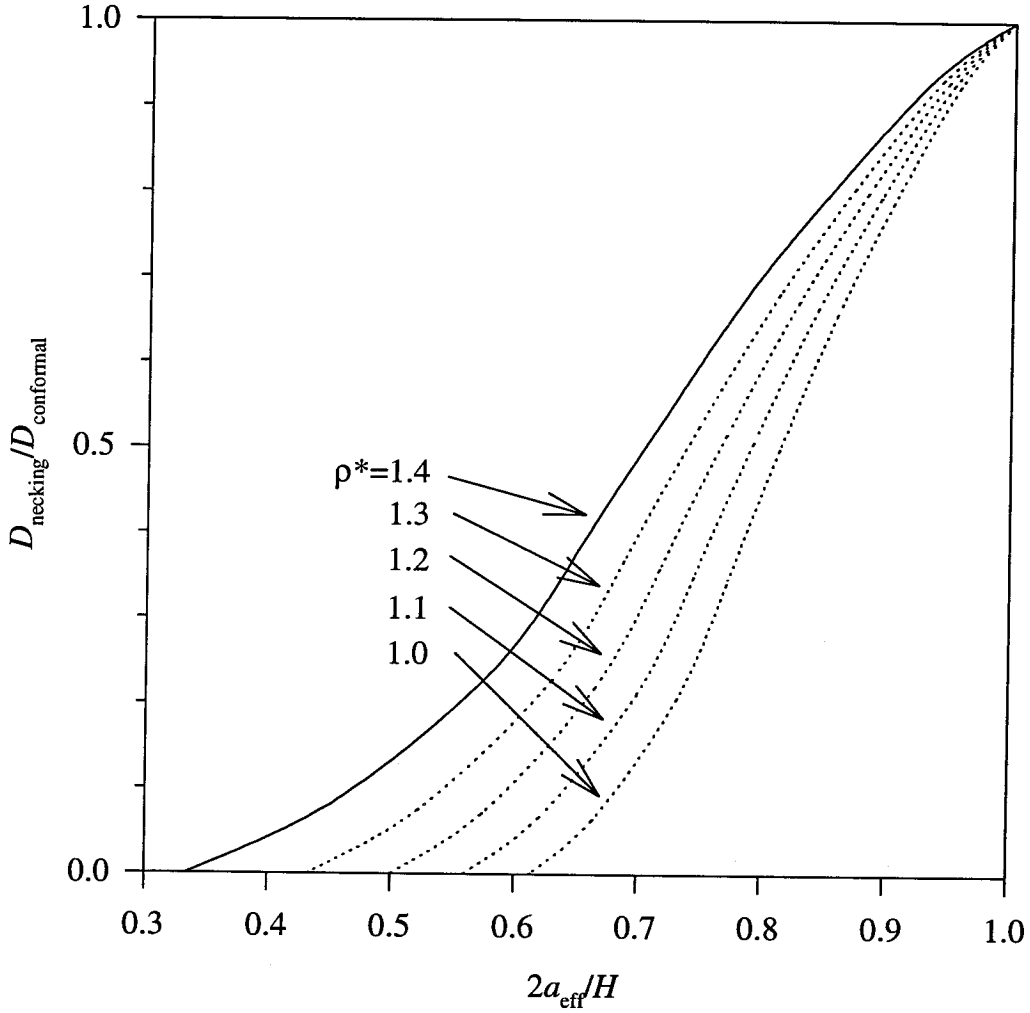

Figure 2.12 Correction factor for pore necking for different assumed deposit densities

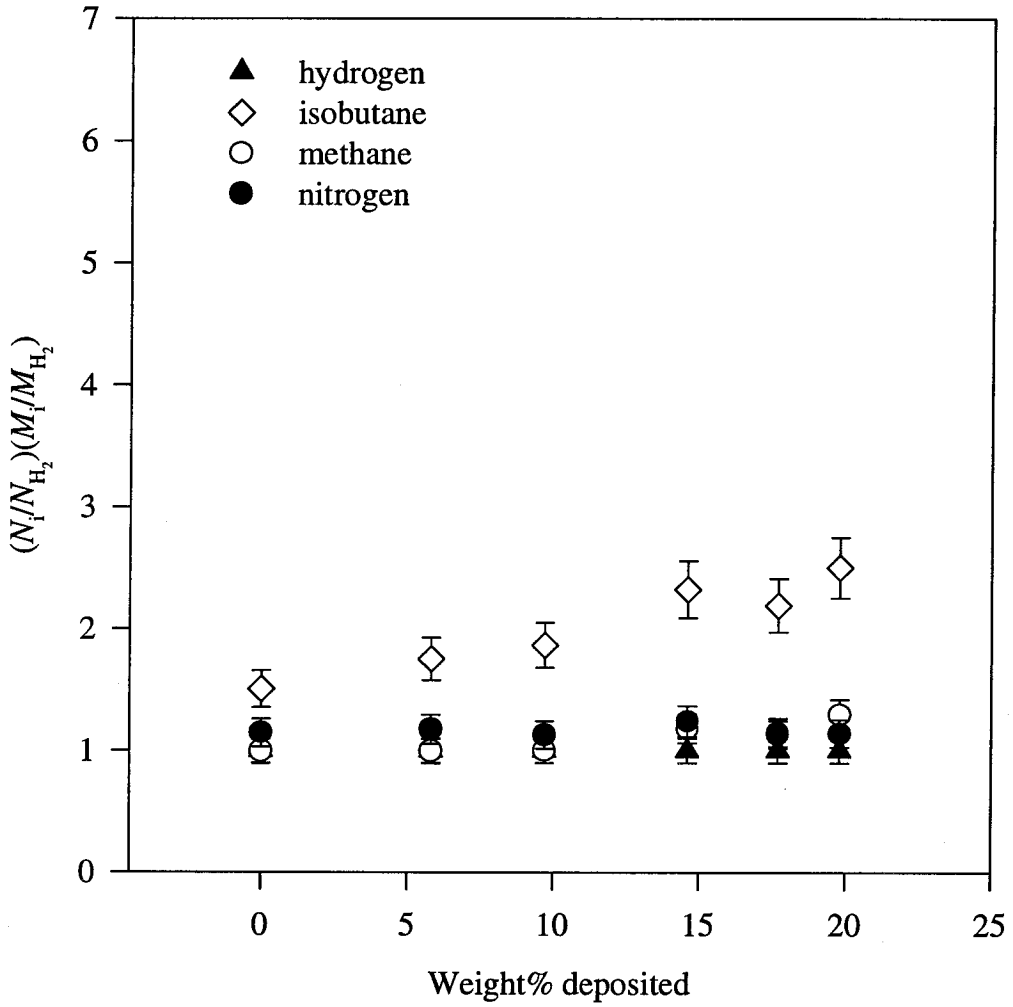

Figure 2.13 Normalized permeance of different gases at 180°C vs extent of deposition

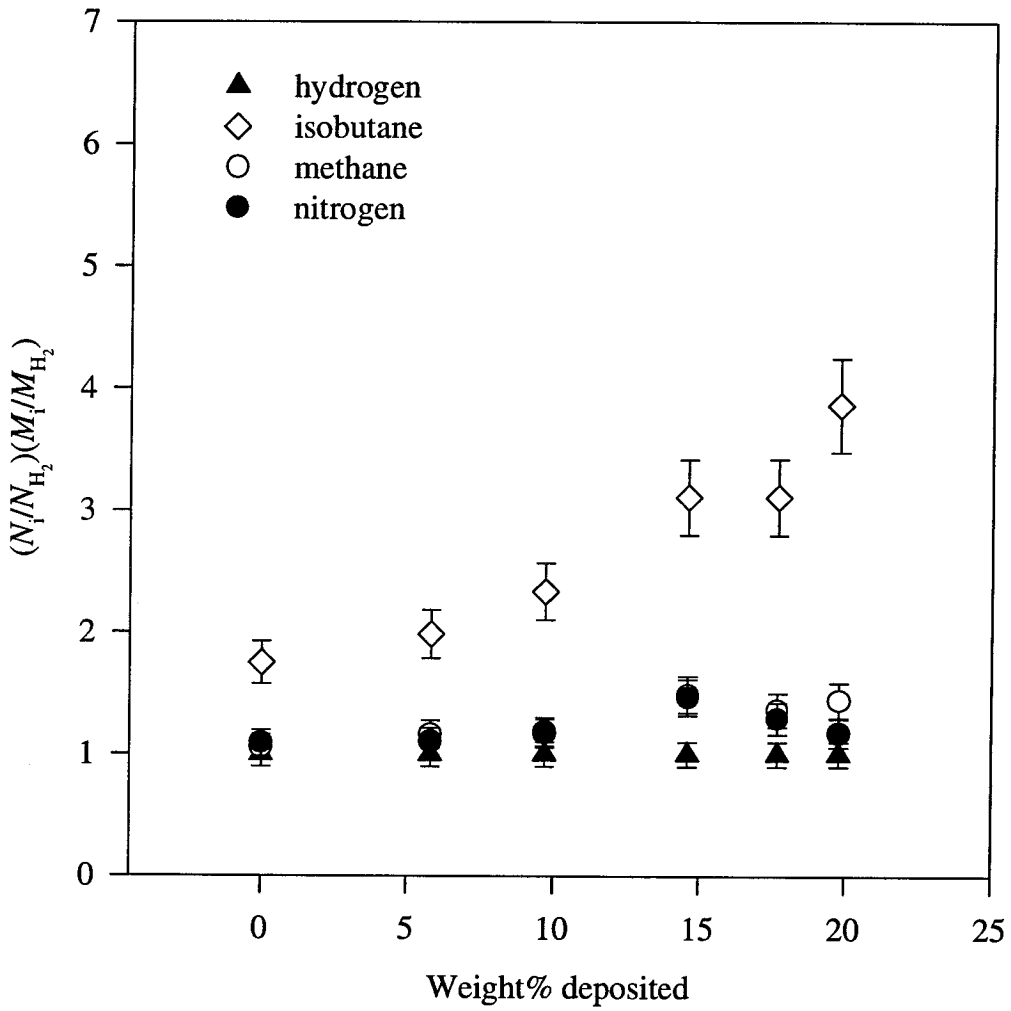

Figure 2.14 Normalized permeance of different gases at 120°C vs extent of deposition

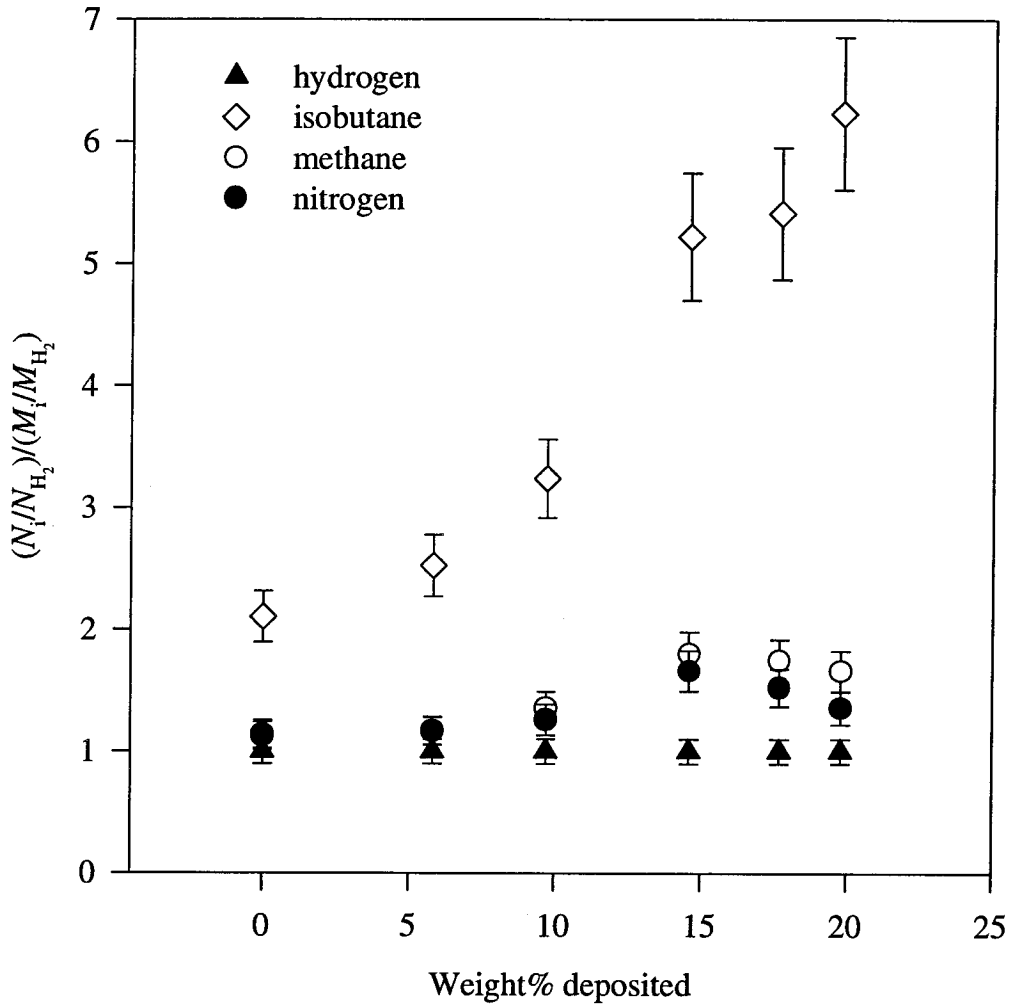

Figure 2.15 Normalized permeance of different gases at 60°C vs extent of deposition

Chapter 3

Molecular Dynamics Simulations of Diffusion in Mesoporous Glass

Abstract

In an effort to understand the importance of the intrapore potential and pore surface roughness on diffusion, molecular dynamics simulations of nitrogen and isobutane in a mesoporous glass pore, under free molecular flow conditions, were conducted for pores of radius 20Å to 10Å and for temperatures between 200K and 800K. To study the effect of the intrapore potential, the gases were treated as simple Lennard-Jones atoms, and the pore was simulated as a perfect cylinder exerting a 9-3 potential, but with its surface roughened by the superposition of spherical Lennard-Jones atoms representing silica tetrahedra. The molecular trajectories in the passive potential were simulated using Nosé-Hooverian mechanics. No mechanism was utilized for transferring energy between the solid and gas and the gas scattering required for random walk behavior was solely due to specular collisions with the rough surface. The effect of the intrapore potential was decoupled into two contributions. The effective diffusivity was respectively increased and decreased through a partitioning effect (or Henry's law adsorption) and a path curvature effect (the trapping of molecules near the surface). In pores of radius 20Å, both effects were present for temperatures as high as 500K and were enhanced as the temperature decreased. For nitrogen the two effects approximately canceled each other over the temperature range of 500-200K and resulted in a temperature dependence similar to that of Knudsen diffusion. For isobutane the partitioning effect overwhelmed the path curvature effect resulting in significant surface flows at temperatures as high as 500K. At a temperature of 393K, as the pore radius was reduced from 20Å to 10Å, the path curvature effect decreased and the partitioning effect increased. Although the intrapore potential becomes more negative as the pore size decreases, the magnitude of the potential energy barrier trapping molecules near the surface also decreases. The effect of surface roughness was studied through a hard sphere dynamics version of the above simulation. Diffusivities were obtained for various surface coverage of the silica tetrahedra. The specular reflection condition resulted in diffusivities at least twice those obtained using diffuse reflection.

3.1 Introduction

The main result in the previous chapter was the failure of simple capillary network models to predict the evolution of the effective diffusivity in mesoporous materials undergoing pore closure. On the one hand it was discussed that the pore shape or geometry is important. In the case of silica deposition in Vycor, deviations from the assumed conformal pore closing resulted in lower effective diffusivities than simple models would predict. On the other hand it was clearly demonstrated that even for untreated Vycor it is necessary to account for the effects of the intrapore potential. The effects of pore shape and intrapore potential are equally important but it is not clear how one can correct for geometry since at this microscopic length scale geometric information is very difficult to obtain and quantify. As was pointed out at the end of the previous chapter however, the effects of the intrapore potential can be studied using molecular dynamics (MD) and Monte Carlo techniques. In this chapter these methods are used to investigate the diffusivity and permeation rate of various spherical molecules in infinite cylindrical pores under free molecular flow conditions. In particular an attempt is made to quantify the separate effects of partitioning and molecular path curvature on the gas permeation rates.

Before formulating the prescription for the MD simulations, it is instructive to briefly review the initial works on rarefied gas flow in infinite capillaries and to discuss in more detail the effects of the intrapore potential as well as the gas-surface interactions.

Several expressions were derived for diffusion in capillaries under free molecular flow conditions, in the early decades of this century, and these expressions have been applied to porous media without modification ever since. The well known formula for Knudsen diffusion was presented by Knudsen in 1909, but more general expressions were provided some years later by Smoluchowski and Clausing (Kennard, 1938). Specifically, Smoluchowski introduced the molecular path tracing technique for calculating diffusivities

in pores of nonre-entrant cross-section, and Clausing calculated transmission factors for capillaries of finite length. All of these free molecular flow models use two major assumptions, linear molecular trajectories, and diffuse reflections of molecules from the pore walls.

3.2 Effects of the Intrapore Potential Field

In part, the deviations between the actual transport properties in an unconfined gas and those inferred from ideal gas theory are due to the effect of the intermolecular potential on the molecular trajectories (Present, 1958). Similarly, one can expect the influence of the *intrapore* force field to be important for molecules in mesopores. Even though in the Henry's law regime gas molecules do not interact with each other, they do experience the force field of the porous substrate. Nicholson *et al.* (1979) and Nicholson and Petropoulos (1981) used molecular dynamics and molecular path tracing techniques to determine the effect of the intrapore potential on diffusion in cylindrical and slit-like pores. They deduced that the intrapore potential field has two strong effects on the diffusivity, namely path curvature and partitioning.

3.2.1 Path Curvature

It is instructive, though admittedly simplistic, to express the diffusivity as

$$D_{\text{pore}} \sim \lambda u_{\text{av}} \tag{3.1}$$

where u_{av} is the mean speed of the gas molecules and λ is the mean free path, or more accurately, the mean step size. For diffusion in the axial direction, λ can be regarded as the mean distance traveled in the direction of the pore axis before a *randomizing* collision with

the surface occurs. For example in the case of strict Knudsen flow in infinite cylindrical capillaries λ scales like the capillary radius. The effect of the intrapore force field on the mean step size of the gas molecules is not obvious. This is more easily examined if, instead of capillaries, one considers diffusion in the space between two infinite slabs (Figure 3.1). Here the surfaces are considered to extend to infinity in the x and y directions. With no potential energy field, a molecule traces out the straight path A. The effect of the intrapore field is to stop a fraction of molecules from crossing the slit, causing them instead to collide back with the reflecting surface, reducing their mean free path (trajectory C). However, the fraction that does escape the potential well curve towards the surface slightly so that after crossing the slit their free path has increased (trajectory B) and it is not clear whether the mean free path averaged over all the molecules has increased or diminished. To gain some understanding of the relative importance of these two effects, the model problem of molecules emitted from a planar surface according to the cosine law of reflection (*diffuse* reflection) is introduced. The implementation of the cosine distribution is equivalent to using the following velocity distributions for molecules reflected from the wall (Nicholson *et al.*, 1979)

$$f_x(v) = f_y(v) = \left(\frac{m}{2\pi kT}\right)^{\frac{1}{2}} \exp\left(-\frac{mv^2}{2kT}\right) \tag{3.2}$$

$$f_z(v) = \left(\frac{m}{kT}\right) v \exp\left(-\frac{mv^2}{2kT}\right) \tag{3.3}$$

Assuming an increasing potential $\Phi(h)$, it is relatively simple to calculate a general expression for the mean free path (Appendix B). Exploiting the symmetry of the problem and defining the following simplistic potential for the lower half of the slit in Figure 3.1

$$\phi(z) = \frac{\phi_o z}{H} \qquad z < H \qquad (3.4)$$

$$\phi(z) = \phi_o \qquad D/2 > z \geq H \qquad (3.5)$$

and the dimensionless parameters

$$u = \sqrt{\frac{m}{2kT}} v \;,\; \Phi = \frac{m\phi_o}{kT} \;,\; \Lambda = \frac{\lambda}{H} \;,\; D = \frac{d}{H} \qquad (3.6)$$

the mean free path, Λ, is eventually expressed as

$$\Lambda(\Phi, D) = \Lambda_1 + \Lambda_2 \qquad (3.7)$$

$$\Lambda_1(\Phi) = \frac{\pi}{\Phi} \operatorname{erf}\left(\sqrt{\Phi}\right) - \frac{2\sqrt{\pi}\exp[-\Phi]}{\sqrt{\Phi}} \qquad (3.8)$$

$$\Lambda_2(\Phi, D) = \pi(D-1)\exp(-\Phi) + \frac{4\sqrt{\pi}}{\Phi} \int_{\sqrt{\Phi}}^{\infty} \left(u\sqrt{u^2 - \Phi} - u\right)\exp\left(-u^2\right) \mathrm{d}u \qquad (3.9)$$

Here Λ_1 is the normalized contribution from molecules which do not escape the force field, and Λ_2 is the complementary contribution to the mean free path from molecules which cross the slit. The former contribution is independent of the dimensionless slit width as expected. Under zero field conditions the contribution from Λ_1 is zero and the contribution from Λ_2 is $\pi D/H$. It is interesting to note that

$$\lim_{D\to\infty}\frac{\Lambda(\Phi,D)}{\Lambda(0,D)}=\exp(-\Phi) \tag{3.10}$$

and the existence of a potential field in this example is seen to have ramifications for the mean free path even for very large pores. To verify that the potential does enhance the mean free path of some molecules, we examine Λ_2, normalizing it with the mean free path of molecules with initial velocity $u_z>\Phi^{1/2}$ calculated under zero field conditions, namely

$$\Lambda_1(0,D)=2\sqrt{\pi}D\ \mathrm{erfc}\left(\sqrt{\Phi}\right) \tag{3.11}$$

This ratio is plotted in Figure 3.2 for D/H=1. As shown in Figure 3.3, however, even though the free path of some molecules might be increased, the overall effect of the potential is to reduce the mean free path. One must understand that this is only a model problem, and in a real solid the diffusive process is more complex and not amenable to simple analyses. In particular, the intrapore potentials are complicated due to the non-ideal pore geometries and it is uncertain how the reflections from the pore surfaces must be treated.

3.2.2 Partitioning and Henry's Law

Besides influencing transport via its bending of the molecular paths, the intrapore potential also affects transport by the partitioning of molecules between the bulk gas phase and the porous gas space. Continuity of the chemical potential across the bulk gas/solid interface dictates that the gas concentration in the pore space must be higher than in the bulk gas. The partitioning coefficient is sometimes called Henry's constant (after the analogy with liquid

solutions) when the gas in the pore space is dilute enough that interactions between gas molecules is negligible. Under these conditions the partitioning constant K is a function of only the intrapore potential and can be expressed as

$$K = \frac{c_{\text{pore}}}{c_{\text{bulk}}} = \frac{\int_V e^{-\frac{\Phi}{kT}} dV}{V} \tag{3.12}$$

The partitioning coefficient has important consequences for the gas permeances since the concentration difference in the porous solid is not Δc_{bulk} but $K\Delta c_{\text{bulk}}$. Since the internal gas concentrations in many cases are not experimentally accessible, one often deals with the permeability here defined as KD_{pore}/RT, where D_{pore} is the diffusivity calculated from the random walk of molecules in the pore space. The factor RT is included because the flux is commonly expressed in terms of pressure rather than concentration differences

$$N = \frac{KD_{\text{pore}}}{RT}\frac{\Delta P}{L} \tag{3.13}$$

In this expression the dependence of the permeability on the network topology has been ignored. The effect on the flux of the internal concentration being higher than the external concentration has often been attributed to a surface flux. There is, however, no fundamental reason to distinguish between molecules in the gas phase and molecules on the surface. In fact, such definitions become untenable in the microporous range where it is difficult to define unambiguously what the pore surface is. This difficulty is also reflected in the calculation of K. When length scales are very small such as they are for small mesopores and micropores, there is a basic uncertainty in what constitutes matter and what constitutes free space. This uncertainty is related to the distinction between hard sphere

molecular dynamics and soft sphere molecular dynamics (Section 3.5). In the former case molecules possess a finite volume into which other molecules cannot penetrate, whereas in the latter case there is no absolutely impenetrable molecular volume. At these small length scales pore surfaces exhibit several kinds of atomic heterogeneities (such as defects, adatoms, etc.) making it difficult to decide *a priori* what the effective pore volume is. Owing to this ambiguity it makes sense to interpret the partitioning constant as the product of two constants - the traditional Henry's constant K_H and the volume exclusion factor K_V

$$K = K_H K_V \tag{3.14}$$

K can then be calculated in any defined volume, including both the gas and solid spaces. K_H can be conveniently calculated from equation (3.12), but by averaging over only those volume elements in which the potential energy is less that some value Φ^*, effectively defining the hard surface of the pore (i.e., the integration space in equation (3.12) is the volume of the gas space). The interpretation of K_V depends on the integration space used for calculating K. If the integration space for K is chosen to be the apparent volume of the macroscopic porous solid, then K_V can be understood as an effective void fraction, or equivalently, as the fraction of the porous solid's cross-sectional area that is available for transport.

3.3 Surface Roughness

In the analysis of path curvature effects presented in Section 3.2.1 the mean free path was calculated as the mean distance traveled between successive collisions with the pore wall. After a collision the molecule is assumed to be reflected according to the cosine law, i.e., with a completely random direction in the x-y plane. If this direction is not completely random then an *effective* mean free path must be used in expression (3.1). This idea can be

motivated by the following example. Consider the one-dimensional random walk. Assuming equal step sizes λ and a 50% chance of stepping in either the positive or negative directions, the mean-squared distance is given by the well known expression

$$\langle X^2 \rangle = n\lambda^2 \tag{3.15}$$

where n is the number of steps taken. If however a correlation is introduced such that the walker, after each step, continues to move in the same direction with probability p then one can deduce (Appendix B) that the mean-squared distance is

$$\langle X^2 \rangle = \frac{p}{1-p} n\lambda^2 \tag{3.16}$$

In the limit of p=0, the diffusivity is also zero as the walker cannot go anywhere; when p=1/2 (the case for diffuse reflections) the result (3.15) is recovered, and when p=1 the process can no longer be considered diffusive. One might consider this example to be analogous to a random walk in a rough-walled pore with *specular* wall reflections. For extremely smooth surfaces p might be close to unity leading to large effective mean free paths, while for rough surfaces p may be one half, or even less if the surface is particularly rough. Although simplistic, the above expression provides good reason to suspect that apart from the intrapore potential and finite molecular size, the mean free path is also affected by the nature of surface reflections.

3.4 Surface Reflections and Velocity Distributions

Gas molecules inside the pores must be in thermal equilibrium with the solid and the velocity distribution obtained by sampling phase space trajectory of a single molecule over a significant period of time should be the Maxwell Boltzmann distribution. How easily this equilibrium is established, or in a simulation, how long one must wait for reasonable statistics to be obtained, depends on the degree of ergodicity or mixing of the pore-gas system (Haile, 1992). In free molecular flow in a porous solid, mixing is caused by energy and momentum exchange with the pore surface. One of the classical measures of thermal equilibration between gases and solids is the thermal accommodation coefficient, α.

$$\alpha = \frac{E_i - E_f}{E_i - E_{eq}(T)} \tag{3.17}$$

Here the numerator is the actual mean energy change of molecules colliding with the solid surface and the denominator represents the mean energy change if the molecules came into thermal equilibrium with the solid. For perfect equilibration, $\alpha=1$. In general, it is found that the lighter the gas, the higher the temperature, and the smoother and cleaner the surface, the smaller is the value of the accomodation coefficient (Knudsen, 1950). For sufficiently rough surfaces with high energy accommodation coefficients, one can expect thermal equilibrium to be achieved relatively quickly. For flat surfaces, for example a polished metal for which accommodation coefficients of ~.02 are typically measured (Massey, 1956), thermal equilibrium may only be established after several collisions. Since the number of collisions required for equilibration can be expected to correlate with the effective step size, one might expect large diffusivities in pores when α~0.1 and small diffusivities when α~1. In his discussion of molecular beam scattering experiments,

Steele (1974) refers to three types of collisions; elastic, quasi-elastic and diffuse reflections. Elastic collisions result when the reflected molecule does not exchange energy with the solid and quasi-elastic collisions mean locally elastic collisions with a moving solid atom resulting in only partial equilibration with the surface. Diffuse reflections imply that gas molecules interact with the pore wall strongly enough to thermally equilibrate with the surface after only one collision (α=1). The cosine law of diffuse reflection attempts to reproduce this effect. In the original conception, when a molecule collides with the surface, it is assumed to come into equilibrium through interactions with other gas molecules trapped in the interstices of the solid surface (Present, 1958), or by the multiple collisions with the solid after penetration of the interstices (Knudsen, 1950). The molecule is eventually emitted with a new velocity, characteristic of the velocity distribution of a gas at the temperature of the solid and *independent* of the velocity with which it arrived. The analogous physical process of this picture of surface reflection is effusion through a pinhole aperture. The cosine law of diffuse reflection can then be derived by assuming that the gas molecule, when it leaves the surface, is in thermal equilibrium with a *fictitious* gas that is considered to exist on the *opposite* side of the pore wall (Present, 1958). The resulting cosine law of reflection is almost universally applied to treat the gas-surface interactions in free molecular flow simulations. Evidence for this assumption came initially from the experimental verification of Knudsen's equation for free molecular flow in long glass capillaries (Knudsen, 1950). However, a host of molecular beam scattering experiments conducted at temperatures of 100-500°C (summarized by Steele, 1974) have shown that scattering from non-metal and metal crystals is neither diffuse, nor specular; and that collisions are neither trapping nor elastic, but something in between. A variety of models for surface scattering from ideal planar crystal surfaces have been proposed and they have all had moderate success in qualitatively explaining some of the scattering phenomena. However, a model was proposed by Healy (1967) demonstrated that the frequently observed pseudospecular scattering patterns could be obtained by assuming

specular scattering from a rough surface. In general, gas-solid interactions involve energy and momentum exchange which is very complex and varied between different substrates, and it is impossible to summarize them in conditions as simple as diffuse reflection or specular reflection. One can nevertheless reconcile the experimental results of Knudsen diffusion with the apparently contrary results of molecular beam experiments by realizing that these experiments are analyzed at different length scales. Strictly, scattering is a molecular scale event. At a molecular level, acknowledging the dynamics of both the gas molecule and the surface lattice, the collision is specular or quasi-elastic in that Newton's laws of mechanics hold. If the dynamics of the surface lattice are ignored but it is accepted the surface has a non-planar topology (or roughness), then the reflected molecule will appear to have a specular bias (the persistence of velocity effect in the kinetic theory of gases, Present, 1958). If the surface structure is completely ignored and considered to be flat (which it is on the large length scales of the diffusion experiments), then the scattering may appear to be diffuse. In the molecular dynamics simulations presented here, it will be demonstrated that specular reflections from a rough surface are sufficiently mixed for an isotropic velocity distribution to be attained.

3.5 Molecular Dynamics Simulations

3.5.1 Diffusion in Rough Walled Pores

After the discussion in Section 3.4, the task of simulating all aspects of diffusion in mesopores appears daunting. To simulate diffusion realistically one should account for the internal degrees of freedom of the gas molecules and their coupling with surface phonons. Unfortunately, to include all of these interactions into a molecular dynamics simulation requires massive computational power. Wang *et al.* (1994) have performed simulations for the surface diffusion of hydrogen on a Cu (111) surface at temperatures near 150K, incorporating both the internal degrees of freedom of the gas and energy exchange with the

solid. In the simulations presented here, the internal degrees of freedom of the gas molecules and the dynamics of the solid lattice have been ignored. It is the resulting elastic collisions of the gas molecules with the static surface that are described here as being specular. Phonon-gas interactions are partly responsible for surface scattering behavior; by ignoring them the effective step size in the pore is likely to be overestimated. Nevertheless, it is reasonable to expect that by treating the surface reflections from a rough surface as specular, one might obtain a *limiting* pore diffusivity. It is also reasonable to assume that the influence of surface scattering on the diffusivity is completely decoupled from the intrapore potential effects of partitioning and path curvature, and thus the assumption of specular scattering should not have any influence on the relative effects of these phenomena.

Before presenting the details of the pore simulation, it is necessary to discuss what constitutes surface roughness. Roughness is intuitively felt to be the spatial heterogeneity of a surface, but to consider it more technically one must realize that the length scale which is used to measure these heterogeneities is all-important. For example, a table surface may appear flat but if the surface is magnified, i.e., a smaller length scale is considered, the table is seen to exhibit some surface perturbations away from the simple planar geometry. In fact, surface roughness can often be considered to be fractal in nature, in that the surface maintains its complexity (or roughness) on many length scales. Real pore surfaces can be imagined to behave fractally over only a certain range of length scales, perhaps 2-100Å. In porous Vycor glass, some variation of cross-section along pores of length 120Å may be expected so that one can consider roughness to be apparent at length scales of ~100Å. Moreover, the pore surface is usually saturated with hydroxyl groups so that heterogeneities must also be present at length scales of ~3Å. It is possible to extract this fractal information using adsorption techniques (Pfeifer *et al.*, 1991), however, here

roughness is only considered at the atomic length scale (~3Å) because of the extreme computational burden that would be required to simulate interactions with a fractal surface.

In this work the diffusivity of gas molecules in a mesopore is calculated through Einstein's mean squared distance formula. The pore is considered to be a perfect cylinder roughened with a collection of reflecting spherical *clusters* superimposed on the surface. *Specular* collisions with these clusters, i.e., elastic collisions enable the molecules to execute random walks. Two types of simulation are considered - hard sphere simulations (HSMD), and soft sphere simulations (SSMD) making use of the 6-12 Lennard-Jones (LJ) potential interaction.

In the free molecular flow regime, a dramatic simplification of the simulation problem is afforded by the fact that the gas molecules do not interact with each other but only with the pore surface. To find the mean squared distance, one only needs to independently simulate the behavior of molecules selected from some appropriate phase space, and then find the ensemble average. The absence of gas-gas interactions not only significantly reduces the computer time needed to simulate the problem by orders of magnitude, but also allows any code to be vectorized with close to 100% efficiency. On a parallel computer, each processor is then responsible for simulating the behavior of one molecule.

3.5.2 Pore Simulations

There are many ways of simulating pores. In the work of Bojan *et al.*. (1992), for instance, a carbon mesopore was made by randomly distributing non-overlapping LJ carbon atoms in a cylindrical volume in a way to ensure the true carbon density was matched. The pore was then made by hollowing out a cylinder through this structure. A more advanced procedure for simulating a mesopore in silica (an attempt at modeling a Vycor pore) was presented by Brodka and Zerda (1991) in their study of SF_6 diffusion in porous glass. The

fabrication of the pore was similar to the method of Bojan *et al.* but the solid substrate in this case was atomistically modeled by using the Born-Mayer-Huggins two body potential between the silicon and oxygen atoms. By relaxing the system from high temperature to low temperature via a computational annealing method, a silica structure was found that agreed quite well with many of the experimentally observed parameters of silica. The main problem with using these methods for SSMD simulations is that they are computationally burdensome. Determination of a gas molecule trajectory requires knowing the cartesian coordinates of all of the solid substrate atoms and summing over all the interactions between these stationary atoms and the diffusing molecule.

In the pore model presented here for the SSMD simulations, an analytical form is used for the average force the diffusing molecule experiences due to the underlying solid substrate. The additional force due to the surface clusters is found by summing over individual contributions. This requires one to know only the Cartesian coordinates of the surface clusters.

There are two types of pores that must be assembled; one each for the SSMD and the HSMD simulations. It is useful to review the fundamental differences between SSMD and HSMD simulations. In principle the pores look the same; however, for the HSMD simulation the surface is mathematically defined. One can imagine that a diffusing molecule can "see" the surface, defined by the locus of points at which the potential becomes infinite. The surface location is the same no matter what gas molecules are being considered or what temperature is used in the simulation. In fact, for a given size of molecule, changing the temperature has no effect on the molecular trajectory. On the other hand in the SSMD simulations a potential field, rather than a pore surface, is defined. The diffusing molecules "feel" the surface through the repelling effects of the sharply increasing potential. Here the

surface feels different depending on the velocity of the molecule; changing the temperature has a dramatic effect on the trajectories traced out.

3.5.3 Soft Sphere Dynamics Simulations

The pore for the SSMD simulations is built-up by assembling various force-fields. Everett and Powl (1976) provided a formula for the force-field in an infinite cylindrical pore, but in the form of a slowly converging infinite series. Here, instead of this series, an analytical form is used based on the 9-3 potential for two semi-infinite slabs.

$$\Phi(r) = \frac{2}{3} n\pi\varepsilon_{gs}\sigma_{gs}^3 \left[\frac{2}{15} \left(\frac{\sigma_{gs}^3}{(R_p + r)^9} + \frac{\sigma_{gs}^9}{(R_p - r)^9} \right) - \left(\frac{\sigma_{gs}^3}{(R_p + r)^3} + \frac{\sigma_{gs}^9}{(R_p - r)^3} \right) \right] \tag{3.18}$$

where n is the concentration of attracting centers in the slab material and the parameters σ_{gs} and ε_{gs} are the LJ parameters for the individual gas molecule-solid atom interaction. This equation has the correct form in that the potential changes as a function of radius, increases to infinity at a specified pore radius R_p, and except at very small radii gives values very close to those calculated from the infinite series. However, it is clear that the integrated potential given by the infinite series is no longer appropriate in very confined geometries because the atomic contributions can no longer strictly be treated in a continuous fashion (Steele, 1974). To find an accurate potential for our simulations, the form of equation (3.18) is used but the parameters ε_{gs} and σ_{gs} are treated as fitting constants calculated through the following procedure. In a method very similar to that of Bojan *et al.*, (1992) described above, a cylindrical pore is created within a randomly placed collection of oxygen atoms. The potential energy, averaged over thousands of different axial positions, is calculated as a function of radial position by summing over all of the pairwise LJ

potential gas-oxygen interactions. In this calculation the Lorentz-Berthelot mixing rule is used to calculate the parameters of interaction between gas molecule and oxygen atom in the solid from the gas-gas and oxygen-oxygen parameters. Interactions with silicon atoms are neglected in this calculation due to their low polarizability and shielding by the oxygen atoms (Brodka and Zerda, 1991). The Kirkwood-Müller formula was used to estimate ε_{oo}/k and σ_{oo} as 64K and 3Å respectively. The effective parameters ε_{gs} and σ_{gs} are then found by fitting equation (3.18) to the summation values using non-linear regression. The values of ε_{gs} and σ_{gs} depend on the pore radius and weakly on temperature. This latter dependence arises since typically it is not the potential energy that is important but its exponential and thus the error to be minimized in the non-linear regression is defined as

$$\mathrm{MSE} = \sum_i \left[\exp\left(-\frac{\Phi(r_i)}{kT} \right) - \exp\left(-\frac{\Phi_i}{kT} \right) \right]^2 \qquad (3.19)$$

where Φ_i is the averaged potential calculated by summation at radius r_i and $\Phi(r_i)$ is the potential at r_i calculated from equation (3.19).

To find the interaction between the diffusing molecules and the reflecting surface clusters (treated as being spherically symmetric), non-linear regression is also used to fit ε_{gc} and σ_{gc} for the LJ potential form. The clusters are considered to be regular silica tetrahedra - a point requiring some explanation. It has already been pointed out that the roughness investigated here is on the molecular scale, but no real information is available for ascribing any dimension to it. In the pore narrowing experiments of the previous chapter, $SiCl_4$ and water reacted with the silanol groups on the Vycor pore surface. Thus, the characteristic length of the silica tetrahedron will be comparable to the smallest scale of surface

roughness. To calculate ε_{gc} and σ_{gc}, oxygen atoms are placed at the corners of a tetrahedron consistent with the dimensions of a silica tetrahedron and the potential is calculated as a function of radius by averaging over randomly chosen points on the surface of a sphere centered at the tetrahedron origin. To complete the pore assembly, the clusters are arranged 3.2Å in from the cylindrical surface of radius R_p prescribed for the substrate potential, in a random, mostly non-overlapping configuration. The cluster concentration is calculated to be commensurate with the silanol concentration (vicinal and geminal pairs being counted as one). The silica deposition results from the experiments in Chapter 2 suggest that 2.3 nm^{-2} is a reasonable silanol number density for the Vycor surface.

To avoid correlation effects pore lengths of 1000Å were used and periodic boundary conditions were imposed. The interaction between gas and surface clusters were also assumed to be negligible for intermolecular distances beyond $6\sigma_{gc}$.

3.5.4 Evaluation of the Partitioning Constants

Once the pore has been simulated and the potential energy interactions defined, the partition coefficient K is evaluated simply by finding the average of $\exp(-\Phi/kT)$. This calculation is performed by randomly choosing points inside the cylinder of radius R_p making no exception for the presence of clusters within this volume. With this integration space K_V is interpreted as a factor necessary for correcting the cross-sectional area for transport calculated using R_p.

The Henry's constant K_H is found also by averaging $\exp(-\Phi/kT)$ over the interior of the cylinder, but if at a random point the potential energy is calculated to be greater than

$\Phi^*=100kT$, the point is discarded and a new point chosen. In this way allowance is made for the volume excluded by the surface clusters.

3.5.5 Hard Sphere Dynamics Simulations

The implementation of HSMD simulations requires the solution of quadratic equations only as opposed to the time consuming numerical integration of differential equations needed for the SSMD simulations. Hence it is tempting to replace SSMD simulations in the limit of small intermolecular forces by HSMD simulations; unfortunately, it is also impracticable. Decreasing the energy well parameters, ε_{gc} and ε_{gs}, to zero, does not yield the hard sphere potential. Instead the clusters become "softer" and this decrease in their effective size significantly alters the reflecting character of the pore surface. Nevertheless it is desirable for the pores in the two simulations to be approximately commensurate and to this end the clusters are arranged 3.2Å inwards from the surface of a perfect cylinder of radius R_p in an identical fashion to the arrangement in the SSMD simulation. The size of gas molecules is assumed to be the LJ σ_{gg} obtained from the literature and the size of surface clusters is assumed to be σ_{cc} calculated from the Lorentz-Berthelot mixing rule

$$\sigma_{gc} = \frac{\sigma_{cc} + \sigma_{gg}}{2} \tag{3.2}$$

using the σ_{gc} calculated for the gas cluster interaction in the SSMD simulation. The speed of the HSMD simulations allows the investigation of surface reflection effects which would ordinarily be too time consuming using the SSMD programs.

3.5.6 Simulation Algorithms

For both types of simulation, initial velocities are specified by randomly sampling velocities from the Maxwell Boltmann distribution. In the HSMD simulations the initial positions are chosen at random, whereas for the SSMD simulations the complexity of the surface potential requires the implementation of the Monte Carlo Metropolis algorithm.

Haile (1992) and Allen and Tildesley (1994) provide informative discussions of typical algorithms used for HSMD simulations and the assumption of non interacting molecules makes their implementation particularly simple. In the SSMD case there are a variety of ways in which the behavior of the gas molecules can be simulated. The typical procedure is to numerically integrate the differential equations obtained from the classical equations of motion for each gas molecule. This corresponds to sampling a phase trajectory in the micro-canonical (NVE) ensemble since the Newtonian equations of motion are conservative. In fact, not only is the total system energy conserved, but as a result of the assumption of non-interacting gas molecules, the energy of each molecule is conserved as well. Another method uses Nosé-Hooverian mechanics to rigorously sample trajectories from the canonical (NVT) ensemble. The equations to be solved are given as

$$\frac{\mathrm{d}\mathbf{q}_i}{\mathrm{d}t} = \frac{\mathbf{p}_i}{m_i}\ ,\ \frac{\mathrm{d}\mathbf{p}_i}{\mathrm{d}t} = -\nabla\Phi - \zeta\mathbf{p}_i \tag{3.21}$$

$$\frac{Q}{2}\frac{\mathrm{d}\zeta}{\mathrm{d}t} = \sum_i \frac{|\mathbf{p}_i|^2}{2m} - \tfrac{3}{2}NkT \tag{3.22}$$

where the subscript i refers to molecule i but in this work the molecules are simulated individually and the above equations are only applied to a single molecule at a time. Equations (3.21) and (3.22) change the *speed* of the gas molecules to maintain consistency with the canonical ensemble but it is important to understand that this prescription does not

guarantee that the system will evolve to an equilibrium state from an arbitrary initial condition. In both the NVE and NVT simulations ergodicity depends on the nature of the term $-\nabla\Phi$. In our simulations the ergodicity engendered by the surface clusters is sufficient for equilibrium distributions to be established. Our simulations have shown that, provided that the initial velocities are sampled from the Maxwell Boltzmann distribution, the ensemble averaged mean-squared distances in the NVE and NVT simulations are the same. To improve the statistics all the SSMD simulation results to be presented were generated using Nosé-Hooverian dynamics.

Even though in Nosé-Hooverian mechanics the energy of each molecule changes, this change occurs randomly in time and is not a direct result of interaction with the solid surface. Therefore we still refer to collisions with the surface as being specular. An alternative phenomenological non-conservative model devised by Fraser *et al.* (1977) was also considered. The crucial part of this model is in the description of energy transfer from the solid lattice to the gas molecule. In a conservative system the equations of motion for a molecule traveling in the *i*th direction are

$$m\frac{\mathrm{d}^2 x_i}{\mathrm{d}t^2} = -\frac{\mathrm{d}\Phi}{\mathrm{d}x_i} \tag{3.23}$$

Fraser *et al.* allow the energy of the diffusing molecule to change in a stochastic fashion, but only in response to the surface force field. Their equations of motion are

$$m\frac{\mathrm{d}^2 x_i}{\mathrm{d}t^2} + \frac{\mathrm{d}\Phi}{\mathrm{d}x_i} = -B\left(E_1 - E_2\right)\left(\frac{\mathrm{d}\Phi}{\mathrm{d}x_i}\right)^2\left(\frac{\mathrm{d}x_i}{\mathrm{d}t}\right) \tag{3.24}$$

Here E_1 is the current energy of the gas molecule and E_2 is a new energy chosen from an appropriate energy distribution towards which the molecule aspires. B is effectively a rate constant determining how quickly the new energy is achieved. E_2 is selected as a Poisson process governed by some rate ω such that in a time increment Δt the probability of the system energy being changed is $\omega\Delta t$. Although E_2 undergoes random changes over the whole time interval of the simulation, the rate at which the system approaches this energy depends on the local strength of the force field, the highest energy transfer rate occurring when the force field is strongest, namely near the surface. This model of energy transfer has some appeal in that apart from the scattering mechanism of surface roughness, there is also the possibility of uneven energy transfer to the different degrees of freedom resulting in an intuitive, though hardly rigorous, mechanism for thermal scattering.

To apply the model of Fraser *et al.* the energy E_2 must be chosen such that an ensemble average temperature of the molecule is commensurate with the temperature of the simulation. To this end two conditions must be fulfilled:

(1) The velocity distributions in the three degrees of freedom must be identical

(2) The kinetic energy of the system must be distributed as in the canonical distribution

$$f(E_k) = \frac{2\pi}{(\pi kT)^{3/2}} E_k^{1/2} \exp\left(\frac{E_k}{kT}\right) \tag{3.25}$$

Although the first condition will result from the ergodic nature of the simulation, it is not obvious how the energy can be chosen to guarantee fulfillment of the second requirement. For this reason this model was not implemented.

The equations of motion for all SSMD simulations were integrated using a 4th order Runge-Kutta algorithm with adaptive step size control. This algorithm is particularly slow and is usually shunned by investigators in this field, but in our simulations it was found to be particularly robust when compared to the classical predictor corrector algorithms. Typically 300-500 atoms were necessary to obtain reasonable statistics and simulation times were chosen so that each molecule executed between 100 and 200 wall collisions. The HSMD simulations were fast enough to be run on a Pentium 100MHz processor whereas for the SSMD code a Cray super computer comprising 256 DEC Alpha (21064) microprocessors was used and run times of ~ 1 hour were required for the simulation.

3.6 Results and Discussion

3.6.1 Molecular Interaction Parameters

Using the procedures outlined in Section 3.5.3 the parameters appearing in Table 3.1 were calculated. The resulting interaction parameters, as discussed earlier, which are dependent on the pore radius but only weakly dependent on temperature. In light of this weak dependence and the qualitative nature of the simulation, the parameters in Table 3.1 were calculated at 393K for pores of radius R_p=10Å for hydrogen, isobutane and nitrogen. The gas-gas interaction parameters were obtained from Hirschfelder *et al.* (1964).

3.6.2 Velocity Distributions

To obtain meaningful results from MD simulations, the dynamics of the system are required to be ergodic. Ergodicity is always present in nature, but it is possible for some simulations to be so contrived that the system cannot access all the available phase space. Access to the full energy surface requires the ability to exchange energy between the various degrees of freedom. Insufficient energy exchange may arise because of restrictions

in the degrees of freedom caused by the system geometry or on account of weak particle interactions. In these cases non-equilibrium, though stationary, distributions may arise. Figure 3.4 shows the velocity distributions in the three cartesian directions obtained from the simulation of nitrogen in a model rough-walled pore. The initial positions were chosen at random but the initial velocities in each of the cartesian directions were set at $(\pi/8)^{1/2}v_{av}$ for all molecules. Despite this non-equilibrium initial condition it is clear that Maxwell Boltzmann velocity distributions were obtained as a result of the Nosé-Hooverian energy exchange and the orientational randomness engendered by the clusters.

3.6.3 Hard Sphere Molecular Dynamics Results

The results from the HSMD simulations are of interest in that they loosely decouple the effects of surface roughness from the effects of the intrapore potential. Figure 3.6 illustrates the results of HSMD simulations in pores of radius R_p=25Å. The pore diffusivities of hydrogen, nitrogen, and isobutane, normalized with their mean molecular speeds, are plotted as a function of the cluster surface density. Here the filled markers represent the results of simulations utilizing specular reflection and the empty markers represent the results for diffuse (or cosine) reflection. It is interesting that all of the curves for specular reflection exhibit a minimum near a cluster density of ~1.7 nm^{-2}. At this density the diffusivities resulting from specular reflection are approximately twice those obtained using diffuse reflections. The minimum is not unexpected in that at both very low and high cluster densities the heterogeneity of the surface diminishes. At low cluster densities molecules mostly collide with the smooth wall resulting in large effective step sizes in the axial direction. At high densities the clusters begin to overlap, effectively producing a smooth pore wall, and again the effective step size is increased. A reasonable measure of the surface size heterogeneity is the pore diffusivity. Using this criterion it is clear that the surface roughness depends on the diffusing molecule. At high cluster

densities the normalized diffusivity clearly is an increasing function of molecular size; small molecules find the surface rougher than large molecules. As one might expect, the diffusivities obtained under diffuse reflection conditions are only slightly dependent on the cluster density. This weak dependence is due to small modifications in the mean free path caused by the finite size of the clusters.

The value of the diffusivity results obtained by specular reflection can be regarded as an upper bound for a given degree of surface roughness. If the intrapore potential field can be ignored (for example, at high temperatures or for weakly adsorbing gases such as hydrogen), one can expect the true pore diffusivity to lie between the results obtained by the two types of reflection. The bounds for the true pore diffusivity can be made tighter by incorporating into the simulation other scattering mechanisms such as the phonon-molecule coupling, and by simulating in more detail the shape of the pore and the shape and internal structure of the gas molecules.

3.6.4 Soft Sphere Molecular Dynamics Results

Because of the computational expense of SSMD simulations, only isobutane and nitrogen were studied and only for pores of cluster density 2.3 nm^{-2}. From the permeance results of Chapter 2, it is clear that isobutane and nitrogen show strong and moderate adsorbing effects respectively, and this is also evidenced by the potential energy curves shown for both gases in Figures 3.7 and 3.8. Here the potential energy, averaged over the axial and tangential coordinates, has been normalized against kT at 393K to give an indication of the adsorbing potential of the pores at moderate temperatures. Because of the uncertainty associated with the pore radius due to the surface clusters, an effective pore radius R_i has been defined as

$$R_i = R_p - 3.2 - \tfrac{1}{2}\sigma_{ic} \qquad (3.25)$$

where all dimensions are in Angstrom units and σ_{ic} is the LJ gas cluster size parameter. As the effective pore size decreases, the average potential energy also decreases (becomes more negative), suggesting that partitioning effects will be enhanced. However, it is also noticeable that the well depth ΔE as defined in Figure 3.8 also decreases.

Figures 3.9 and 3.10 respectively demonstrate the effects of temperature and pore radius on the partitioning of nitrogen. As expected the volume exclusion factor K_v is seen to be effectively independent of temperature because near the atom centers small changes in distance lead to large changes in energy. Figure 3.10 shows that as the pore radius decreases, the volume of the surface heterogeneities become more pronounced relative to the free volume of the pore resulting in volume exclusion factors substantially below unity.

The effect of temperature on the pore diffusivity is shown in Figure 3.11 for nitrogen and isobutane in pores of R_p=20Å. The pore diffusivities have been normalized against the average molecular speed to eliminate the effect of mass, and hence for molecules strictly behaving with a Knudsen temperature dependence, the results would be expected to lie on straight lines. Apparently, this is so for nitrogen at high temperatures, but the reduction in the diffusivity with decreasing temperature is dramatic for both gases. This is expected to be due to the path curvature effect which was shown in Section 3.2.1 to be a particularly strong function of $\exp(-\Delta E)$. However, inclusion of the partitioning constant K (Figure 3.12) approximately cancels the path curvature effect in the case of nitrogen, and overwhelms it in the case of isobutane. The results for isobutane are in accord with the experimental results of Chapter 2 where surface flows of isobutane in untreated Vycor were observed at temperatures of 450K. The results for nitrogen are also in accord with our

experimental results but not with the experimental work of Hwang and Kammermeyer (1966) who found surface flows for nitrogen in untreated Vycor at temperatures ~270K. This discrepancy implies that the intrapore potential for nitrogen used in the simulations might on average be too weak. However the simulated pore cannot be expected to entirely capture the nature of a real pore. For example, even though the permeance results of the the previous chapter have suggested the presence of pores with non-ideal geometry (e.g. pores with small necks) the simulated pore is cylindrical. The surface roughness has also been treated in a highly simplified manner. As already discussed in Section 3.5.1, real surfaces can be expected to exhibit roughness on many length scales and this spatial heterogeneity engenders a spectrum of energetic heterogeneities not accounted for in our model.

Because the intrapore potential decreases with decreasing pore radius, it is reasonable to also look for the dependency of partitioning and path curvature on pore radius. The pore diffusivities of the two gases normalized with the Knudsen diffusivity (as calculated at the effective pore radius) are shown as a function of pore size in Figure 3.13. As the pore radius decreases, the normalized diffusivities of both gases increase towards the Knudsen limit. Here again the dramatic effect of path curvature is noticeable. In the HSMD simulations it was demonstrated that specular reflection typically leads to pore diffusivities that are at least twice the Knudsen diffusivities in the same pore, but in this figure at pore radii of ~20Å the pore diffusivities are significantly below the Knudsen value. The decrease of the pore curvature effect with pore radius might have been anticipated after the discussion concerning the size of the potential energy wells in Figures 3.7 and 3.8. In the example of Section 3.2.1, it was made clear that, with regard to the diffusivity, the most dramatic effect of the intrapore potential was its reduction of the mean free path by trapping molecules near the surface. However, as the pore radius decreases, the potential energy barrier responsible for this trapping is seen to also diminish. For isobutane in pores of radius ~4Å the barrier is non-existent. Figure 3.14 presents this same diffusivity data but

incorporates the effects of partitioning, and again it is seen that for isobutane partitioning has the dominating influence on diffusivity. The diffusivity of nitrogen slightly decreases due to volume exclusion effects included in the partitioning constant K. One should be careful in interpreting simulation data when large partitioning effects occur since in this limit the assumption of free molecular flow almost certainly breaks down.

The calculated effects of the pore radius on permeation rates are compared with the experimental permeance results illustrated in Figure 2.14 of the previous chapter, in Figure 3.15. The particular choice of ordinate used in this figure eliminates both the effects of molecular mass and pore geometry, and in the case of the experimental results, it also eliminates the effect of the network topology. To convert from the experimental weight changes to pore radii a deposit density of 1.45 gcm^{-3} was used. It is encouraging to see that the simulation is in good agreement with the measurements, but it is also likely that this agreement is fortuitous. There are many aspects of the experiments that were not accounted for in the simulation. For example, as argued in Chapter 2, there is a large uncertainty in the deposit density that must be used for calculating the effective potential in the pore. As also discussed in Chapter 2, the pores exhibit strong deviations from the ideal cylindrical geometry assumed in the simulation.

Many of the results have been discussed from the standpoint of the effects of partitioning and path curvature but other influences on the diffusivity are likely to be present albeit less easy to detect. The HSMD simulations demonstrated that the pore diffusivity of spherical molecules depends on the relative molecular sizes. In the SSMD simulations then, the scattering efficiency of the surface can be expected to depend on the pore radius and temperature since these variables effectively control the shape of the surface; the intrapore force field is a strong function of the pore radius and the penetrating power of the gas atoms depends on the temperature.

3.7 Conclusion

In the simulation work we have explored the effect of the intrapore potential and surface roughness on the diffusivity.

Both the SSMD and HSMD simulations have used specular scattering from the roughened cylindrical surfaces as a means of creating random walks, but only the HSMD simulations were used to explore the effect of cluster density on the pore diffusivity. The effective mean step size executed by molecules in real pores depends on both the roughness of the pore walls and the degree of thermal equilibration between gas molecule and surface. Since thermal equilibration tends to randomize trajectories, it is likely that a specular prescription for surface scattering overestimates the effective path length. Hence the simulation results can be interpreted as upper bounds for the pore diffusivity. Assuming that the model silica glass surface used in our simulations is representative of a real surface, at least in the smallest scale of roughness, the results suggest that one can expect the limiting diffusivity to be at least twice the Knudsen value.

In the SSMD simulations the intrapore potential has been assumed to manifest itself in two effects - path curvature and partitioning. Both effects were shown to be substantial even at high temperatures. However, for isobutane by far the most important effect was the partitioning on account of which diffusivities in excess of that expected for Knudsen flow were calculated at temperatures as high as 500K. For nitrogen it appears that the partitioning and path curvature effects cancel out resulting in a temperature dependence close to that of Knudsen diffusion over the temperature range of 900-200K. This is not in accord with experimental results of previous investigators which demonstrate nitrogen surface flows to exist at temperatures as high as 270K. In view of the simplistic treatment of the pore shape and the surface roughness it is reasonable to expect some discrepancy. A real surface is likely to be more energetically heterogeneous and permeation studies of

diffusion have suggested that pore shapes are far from ideal. These effects of pore shape and surface roughness can be addressed more fully by incorporating into the pore simulation different cluster sizes and by arranging the clusters in patterns which effectively alter the pore shape.

3.8 Acknowledgments

The authors would like to acknowledge the Jet Propulsion Laboratory, for allowing the use of their supercomputing resources.

3.9 Notation

Symbols not presented here are defined in the text.

Roman

c	gas concentration, mol m^{-3}
D_{pore}	pore diffusivity, m^2s^{-1}
$D_{Knudsen}$	Knudsen diffusivity
H	slit diameter, m
K	partitioning constant
K_H	Henry's constant
K_V	volume exclusion coefficient
L	length of macroscopic sample, m
m	molecular mass, kg
N	molar flux, mol $m^{-2}s^{-1}$
n	number of attracting centres per unit volume
ΔP	pressure difference across macroscopic porous samples, Nm^{-2}
p	probability of molecule continuing in the same direction from which it came
R	gas constant, $Jmol^{-1}K^{-1}$
R_p	pore radius as defined by the 9-3 potential, J
r	radial distance in pore
T	temperature, K
u_{av}	mean molecular speed, ms^{-1}
V	pore volume
v	molecular speed, ms^{-1}
X	distance, m
z	axial distance in pore, m

Greek

α void fraction

ε a measure of the depth of potential well in the pore, also the Lennard-Jones interaction energy, J

λ mean free path, m

σ Lennard-Jones molecular diameter, m

ϕ potential energy, J kg^{-1}

Subscripts

c cluster

g gas

p pore

s surface

Bibliography

Allen, M.P., D.J., Tildesley, 1993, *Computer Simulation of Liquids*, Clarendon Press, Oxford

Bojan, M.J., Vernov, A.V., Steele, W.A., 1992, Simulation Studies of Adsorption in Rough-Walled Cylindrical Pores, *Langmuir*, **8**, 901-908

Brodka, A., Zerda, T.W., 1991, Molecular Dynamics of SF_6 in Porous Silica, *J. Chem Phys.*, **95**(5), 3710-3718

Everett, D.H., Powl, J.C., 1976, Adsorption in Slit-like and Cylindrical Micropores in the Henry's Law Region, *J. Chem. Soc. Faraday Trans. I*, **72**(61), 619-635

Fraser, S., Murrell, J.N., Mason, R., 1976, The Simulation of Gas-Surface Scattering by a Classical Stochastic Propagator Model, *Chem Phys Lett.*, **46**(3), 399-405

Haile, J.M., 1992, *Molecular Dynamics Simulation - Elementary Methods*, John Wiley & Sons, Inc., New York

Hirschfelder, J.O., Curtiss, C.F., Bird, R.B., 1964, *Molecular Theory of Gases and Liquids*, John Wiley & Sons, Inc., New York

Hoover, W.G., 1985, Canonical Dynamics: Equilibrium Phase Space Distributions, *Phys Rev A*, **31**(3), 1695-1697

Hwang, S.T., Kammermeyer, K., 1966, Surface Diffusion in Microporous Media, *Can. J. Chem. Engng*, **44**, 82-89

Kärger, J., Ruthven, D.M., 1992, *Diffusion in Zeolites and Other Microporous Materials*, John Wiley & Sons, Inc., New York

Knudsen, M., 1950, *Kinetic Theory of Gases*, Methuen & Co, London

Massey, H.S.W., Burhop, E.H.S., 1956, *Electronic and Ionic Impact Phenomena*, Oxford University Press, London

Nicholson, D., Petrou, J., Petropoulos, J.H., 1979, Calculation of the Surface Flow of a Dilute Gas in Model Pores from First Principles: 1. Calculation of Free Molecule Flow in an Adsorbent Force Field by Two Methods, *J. Colloid Interface Sci.*, **71**(3), 570-579

Nicholson, D., Petropoulos, J.H., 1981, Calculation of the Surface Flow of a Dilute Gas in Model Pores from First Principles: 2. Molecular Gas Flow in Model Pores as a Function of Gas-Solid Interaction and Pore Shape, *J. Colloid Interface Sci.*, **83**(2), 420-427

Nicholson, D., Petropoulos, J.H., 1985, Calculation of the Surface Flow of a Dilute Gas in Model Pores from First Principles: 3. Molecular Gas Flow in Single Pores and Simple Model Porous Media, *J. Colloid Interface Sci.*, **106**(2), 538-546

Nosé, S., 1990, Constant Temperature Molecular Dynamics, *J. Phys.:Condens Matter*, **2**, SA115-SA119

Pfeifer, P., Johnston, G.P., Deshpande, R., Smith, D.M., Hurd, A.J., 1991, Structure Analysis of Porous Solids from Preadsorbed Films, *Langmuir*, **7**, 2833-2843

Present, D.R., 1958, *Kinetic Theory of Gases*, 1st edn, McGraw-Hill Book Company, New York

Saltsburg, H., Smith, J.N., Rogers, M., 1967, *Fundamentals of Gas-Surface Interactions*, pg 435, Academic Press, New York and London

Steele, W.A., 1974, *The Interaction of Gases with Solid Surfaces*, Chapt. 6, Pergamon Press, New York

Vansant, E.F., Van Der Voort, P., Vrancken, K.C., 1995, Characterization and Chemical Modification of the Silica Surface, *Studies in Surface Science and Catalysis*, **93**, Elsevier

Wang, L., Ge, Q., Billing, G.D., 1994, Molecular Dynamics Study of Diffusion on a Cu(111) Surface, *Surf. Sci.*, **301**, 353-363

	ε_{gg}/k /K	ε_{gc}/k /K	ε_{gs}/k /K	σ_{gg} /Å	σ_{gc} /Å	σ_{gs} /Å
hydrogen	29	-	-	2.78	4.07	3.03
nitrogen	80	111	65	3.75	4.53	3.53
isobutane	313	338	165	5.34	5.19	4.17

Table 3.1 Intermolecular potential parameters

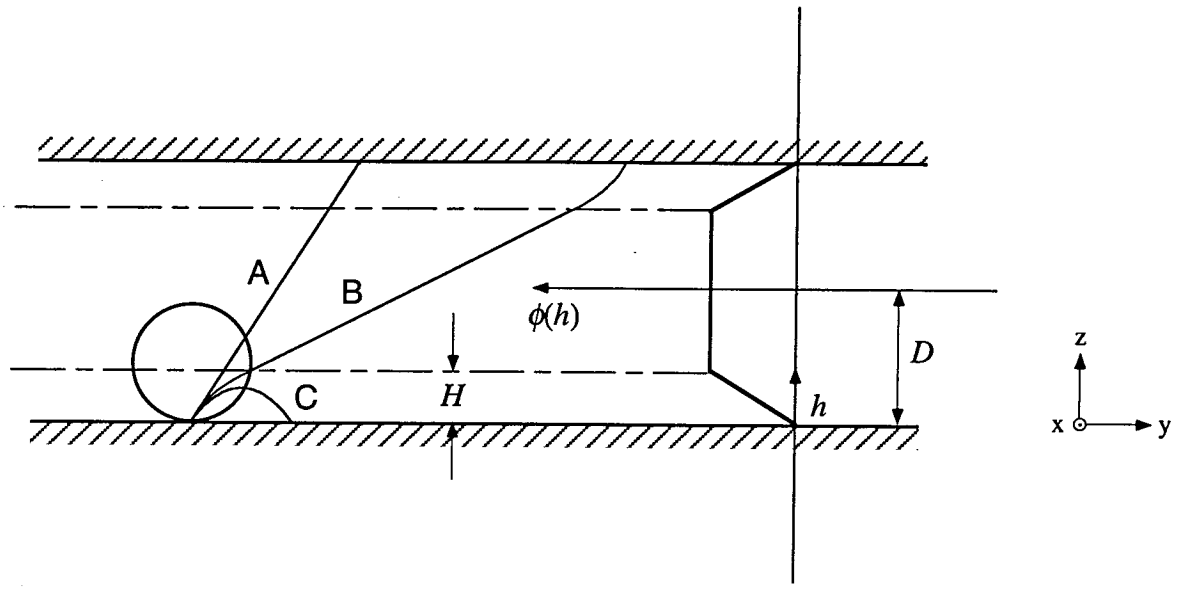

A Zero field trajectory for arbitrary v

B Trajectory of molecule with initial $v_z > (2\phi_o)^{1/2}$

C Trajectory of molecule with initial $v_z < (2\phi_o)^{1/2}$

Figure 3.1 Molecular trajectories and the intrapore potential for the slit problem

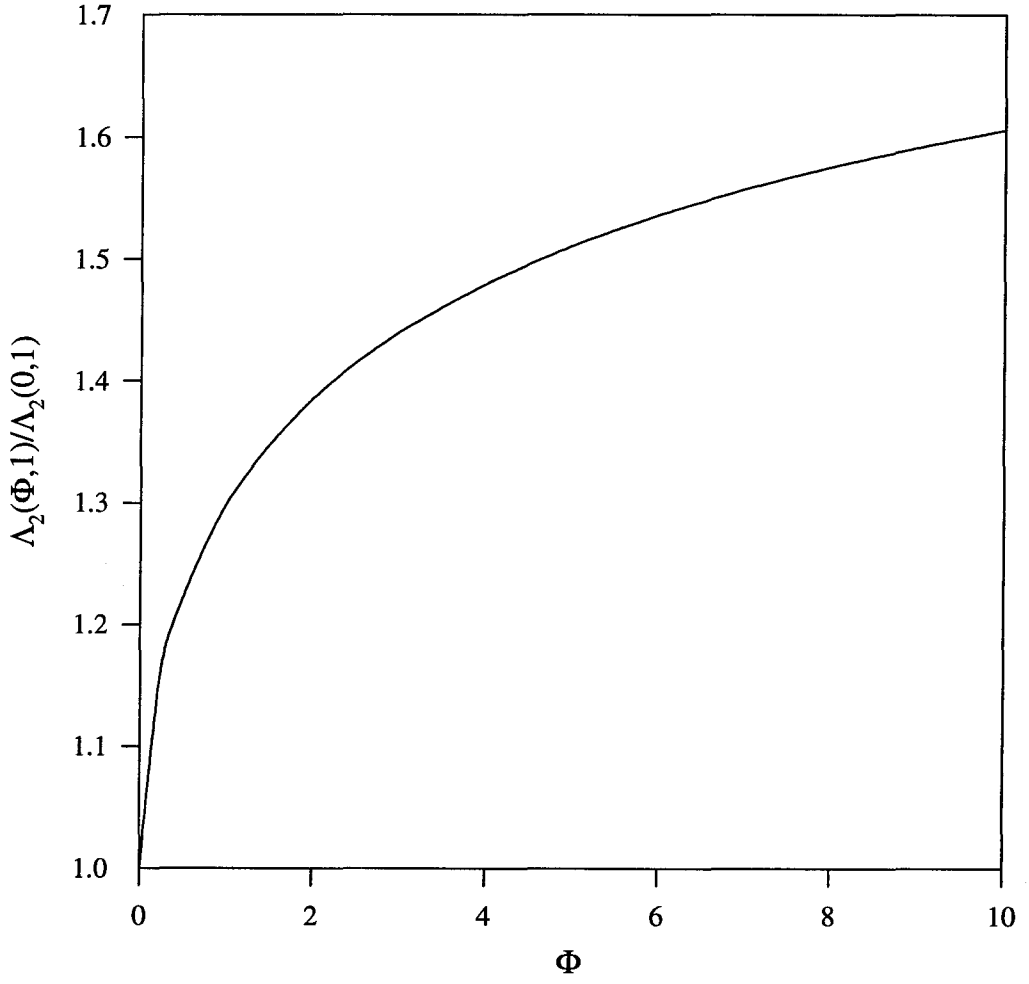

Figure 3.2 Normalized mean free path of molecules with $u>\Phi^{1/2}$ as a function of Φ for $D/H=1$

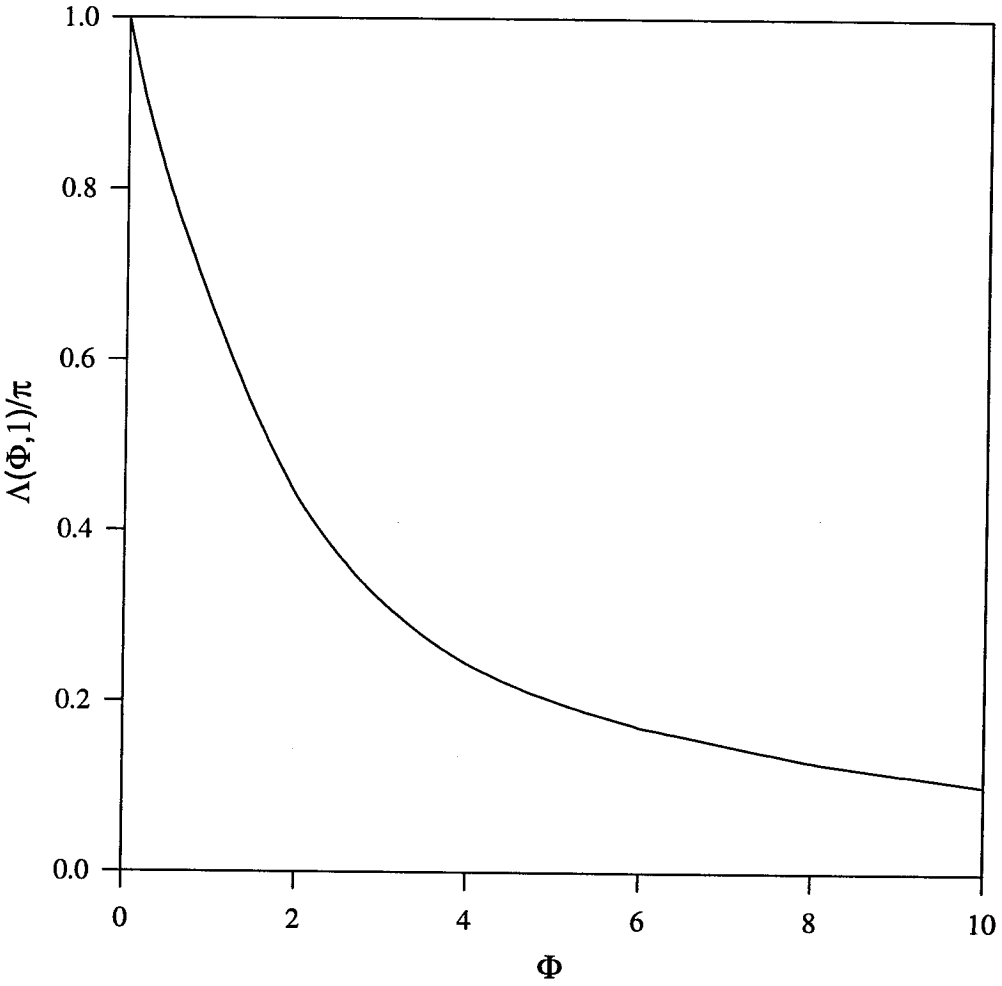

Figure 3.3 Normalized mean free path as a function of Φ for D/H=1

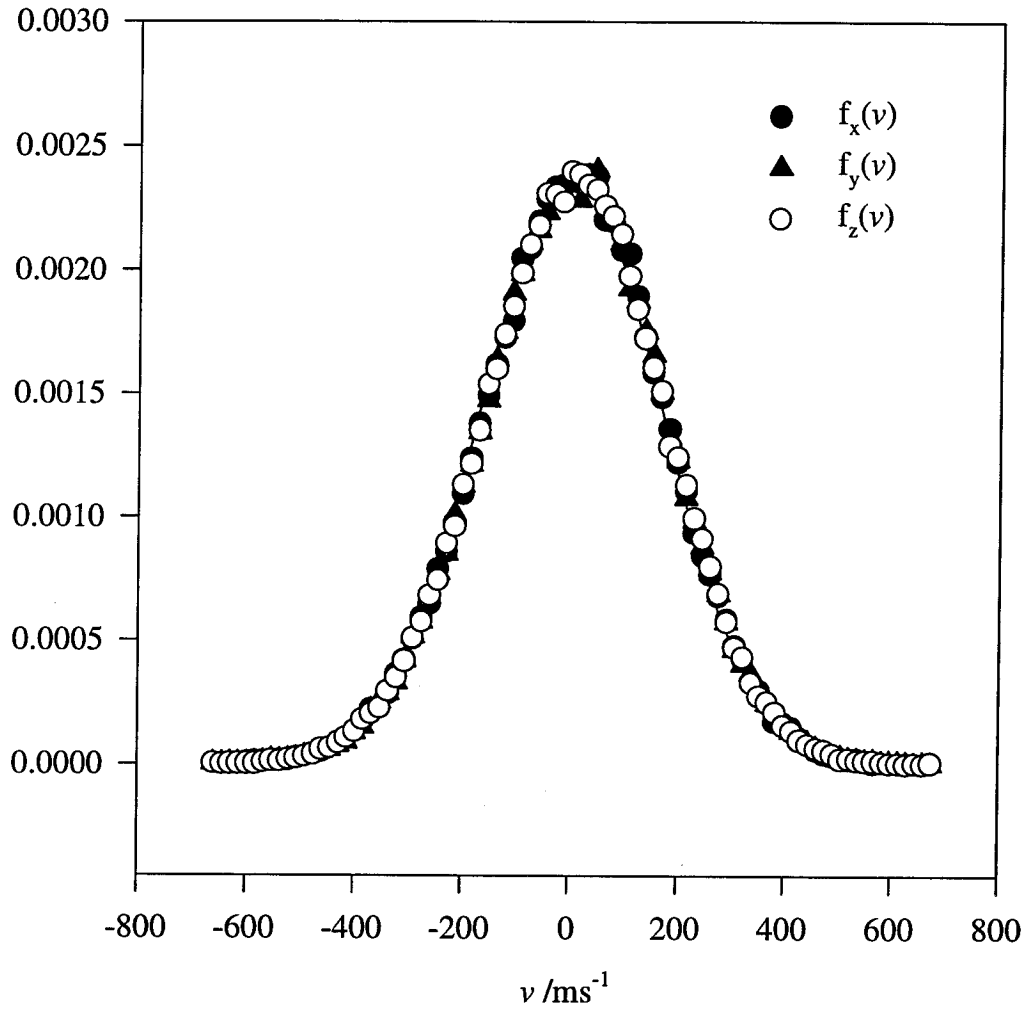

Figure 3.4 Velocity distributions obtained from the SSMD simulation of nitrogen at 200K. Cluster density = 0.5 nm^{-2}

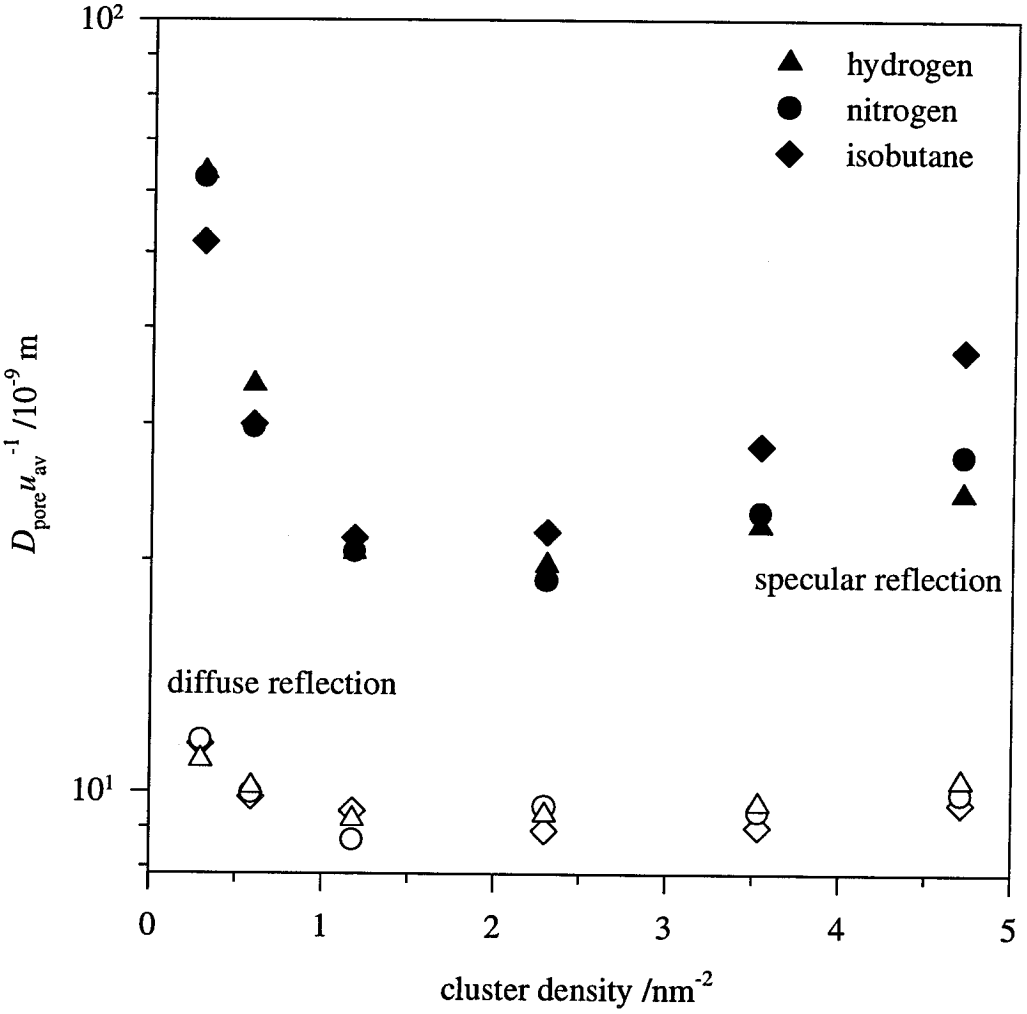

Figure 3.5 HSMD results of diffusion of isobutane, nitrogen, and hydrogen in pores of R_p = 25Å at 393K

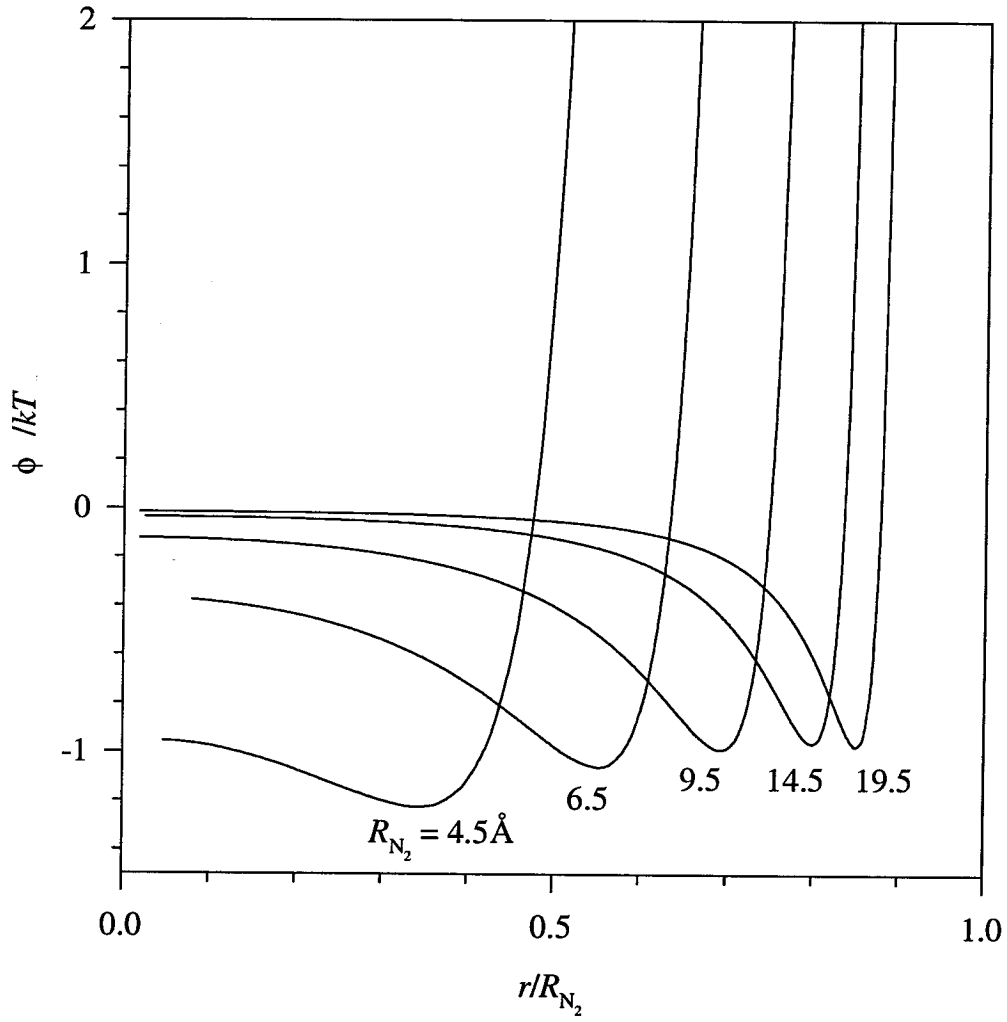

Figure 3.6 Intrapore potential for nitrogen in silica pores at various pore radii. The potential has been normalized with kT at 393K

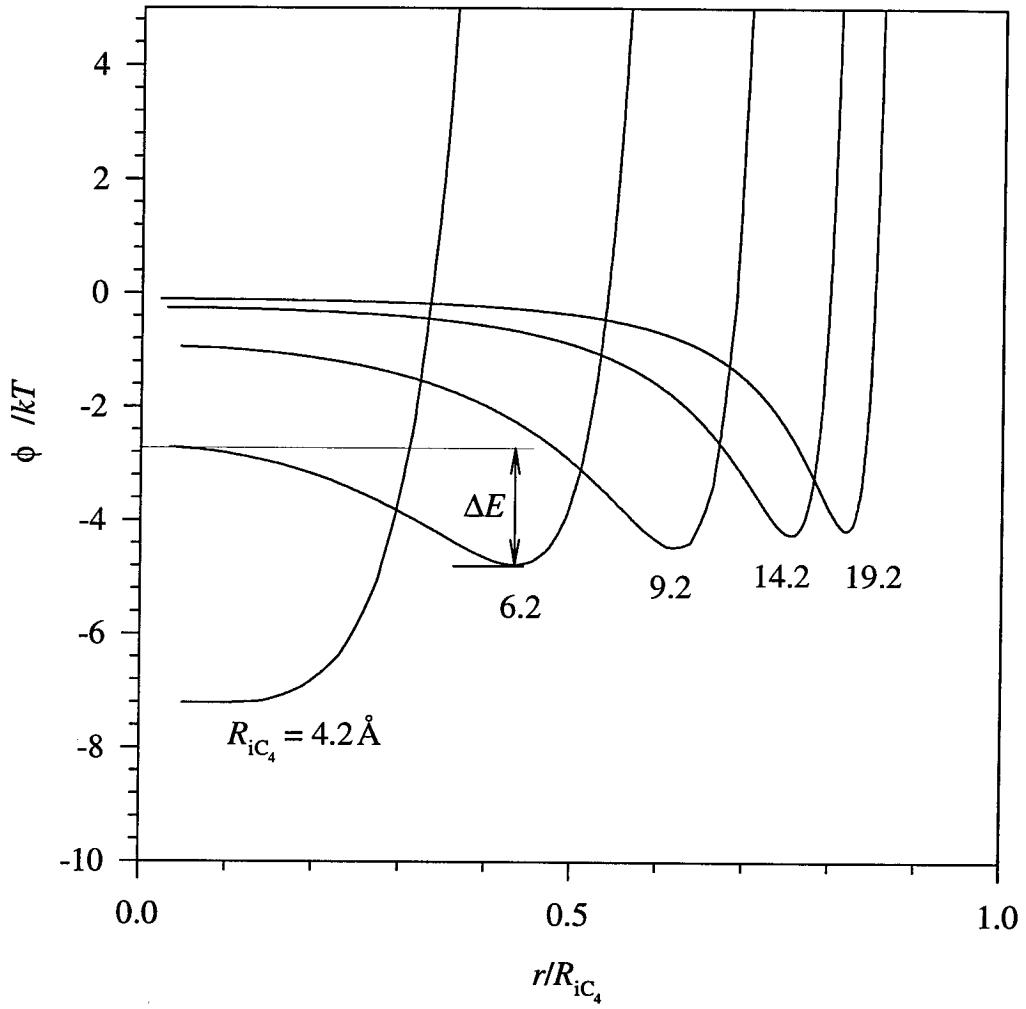

Figure 3.7 Intrapore potential for isobutane in silica pores of various pore radii. The potential has been normalized with kT at 393K

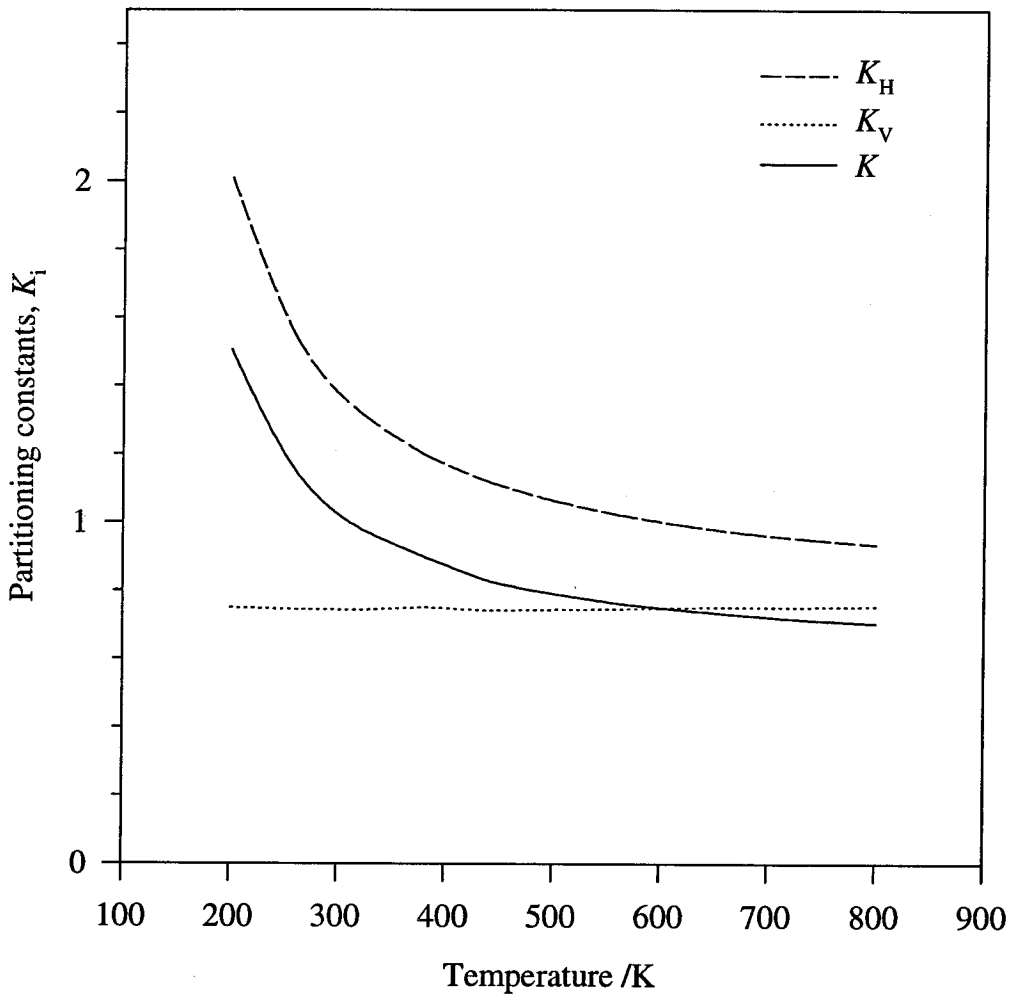

Figure 3.8 The variation of the partitioning constant K and its separate contributions K_H and K_V for nitrogen in silica pores of radius R_p = 20Å with temperature

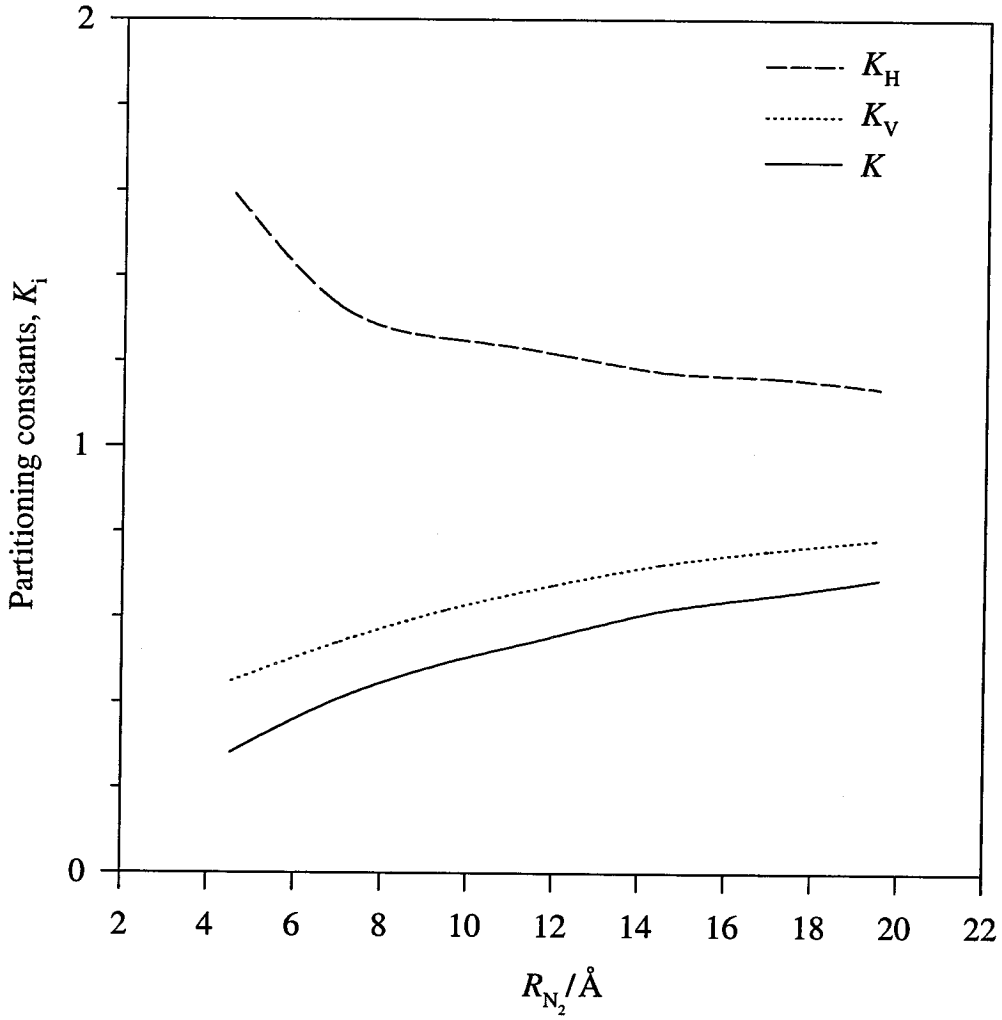

Figure 3.9 The variation with pore radius, of the partitioning constant K and its separate contributions K_H and K_V for nitrogen in silica pores, at 393K

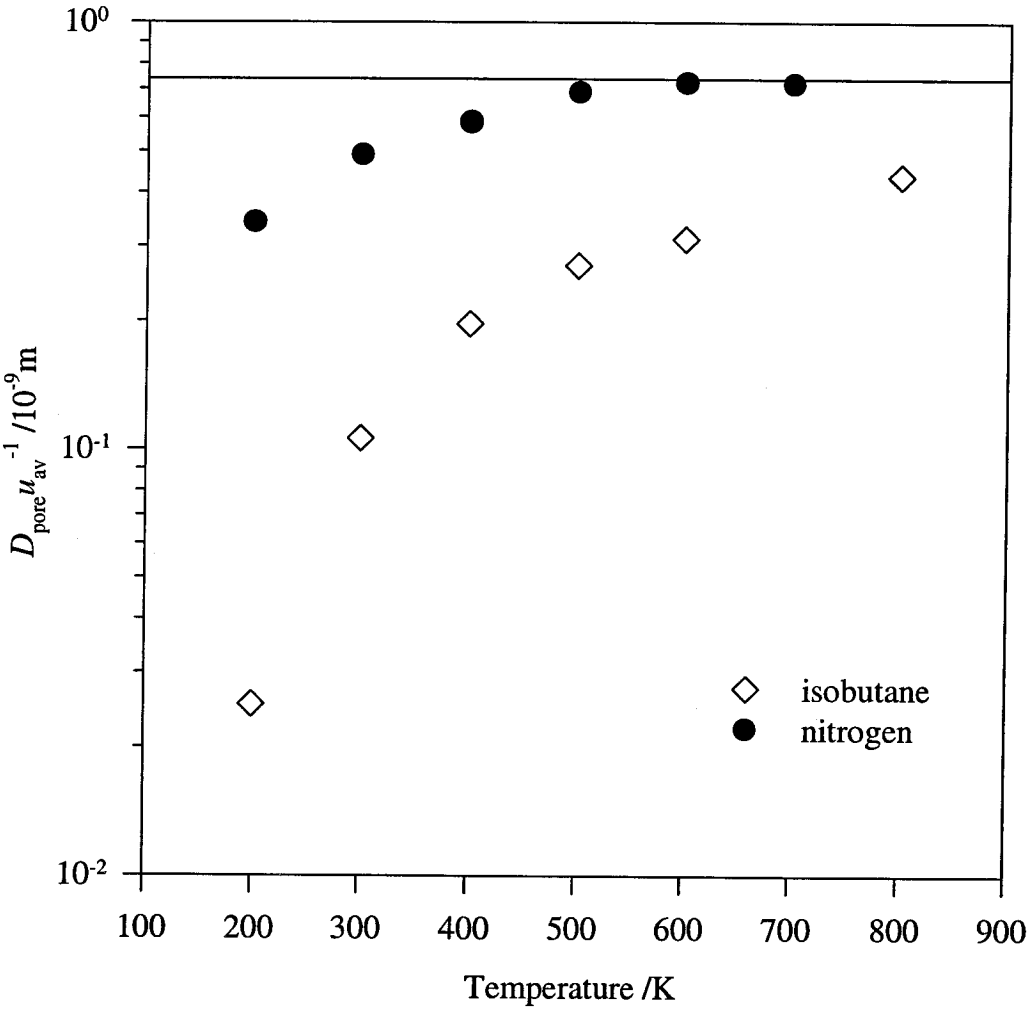

Figure 3.10 The variation of the nitrogen and isobutane pore diffusivities with temperature. R_p = 20Å

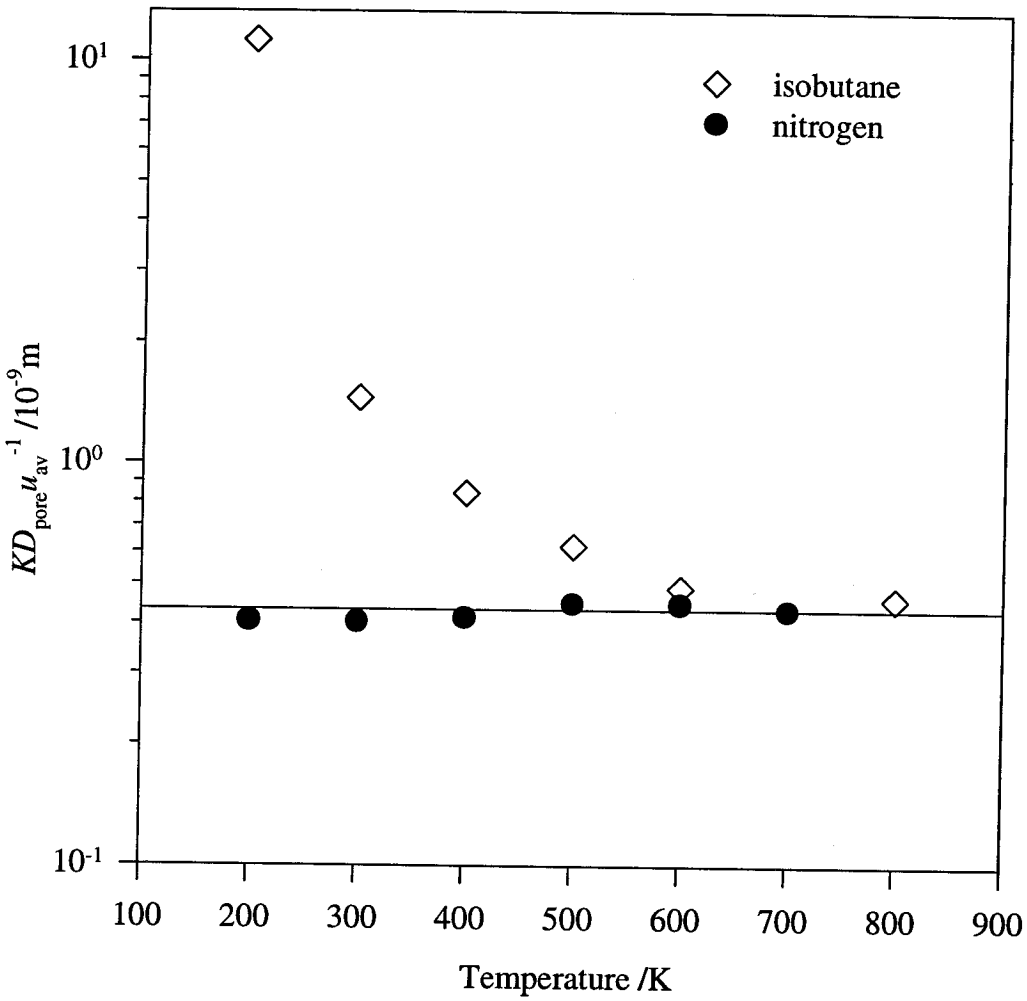

Figure 3.11 Variation of the nitrogen and isobutane effective pore diffusivities with temperature. R_p =20Å

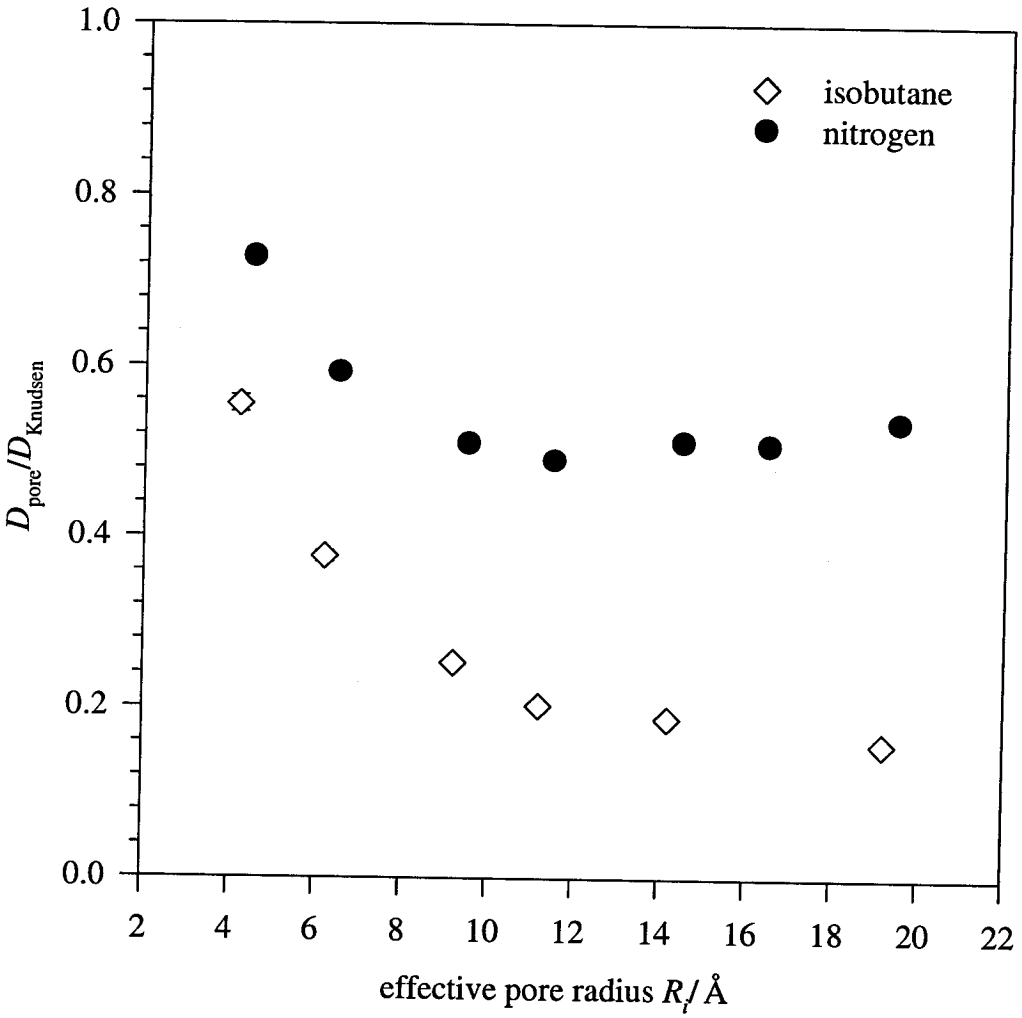

Figure 3.12 Variation of normalized pore diffusivities with pore radius

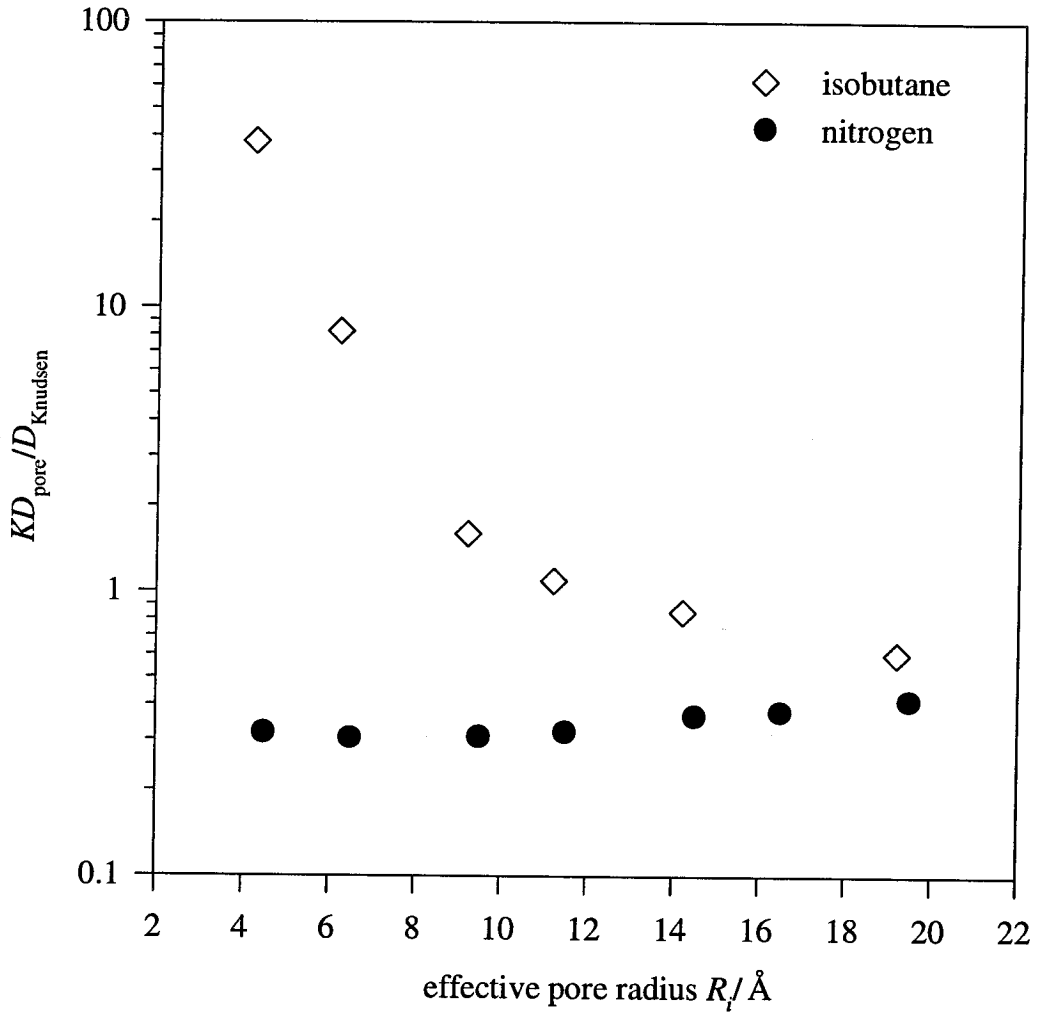

Figure 3.13 Variation of normalized effective pore diffusivities with pore radius at 393K

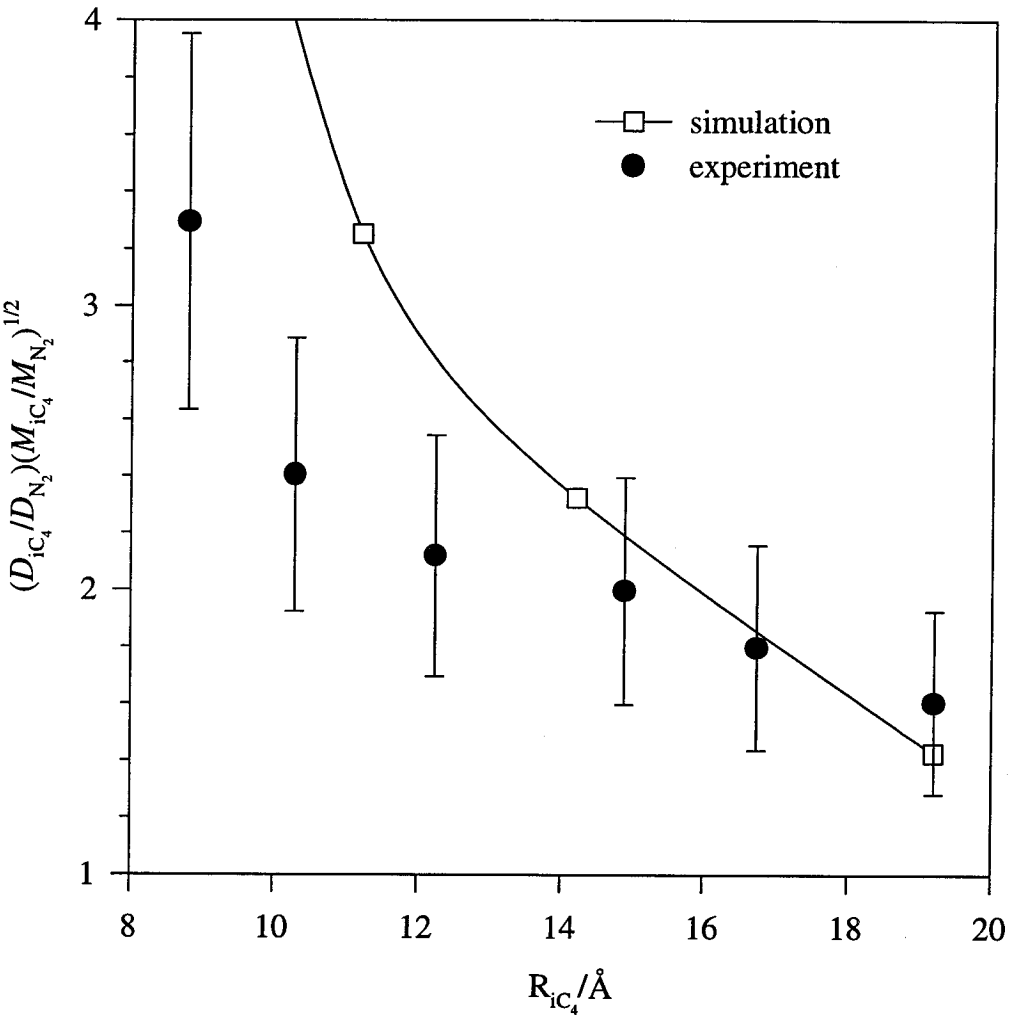

Figure 3.14 Comparison of SSMD simulation results with the pore narrowing experiment results. Normalized effective diffusivity vs pore radius

Chapter 4

Concluding Remarks

4.1 Concluding Remarks

The aim of this thesis was to explore diffusion in mesoporous materials, and to this end experiments were conducted with mesoporous glass. Vycor is considered to be a model material with well defined characteristics, however, even using models considered to be fairly accurate, we were unable to successfully predict the permeance behavior of relatively simple gases. The discrepancy was attributed to non-ideal pore geometry and the neglect of the effects of the intrapore potential.

This illustrates one of the difficulties one can expect to encounter in the mesoporous/microporous range. The molecular scale surface roughness, common to all surfaces, does not significantly change the shape of large pores. As a result, in the macroporous regime, cylindrical pore models are often reasonable approximations. However, for small pores, in the size range of 40Å, any surface deviation is significant enough to influence the pore shape. At these length scales it is very difficult to obtain quantitative information concerning pore geometry. In this work the analytical methods exploited macroscopic phenomena, such as capillary condensation and simple permeance, to infer microscopic details such as the pore radius.

It is for this reason that molecular simulations have come to the forefront of science. At the moment, the technology to accurately determine the pore shapes in mesoporous materials does not exist, but attempts have already been made to simulate the pore structure of Vycor (Monette *et al*, 1994). In our molecular dynamics simulation work it was shown that through a relatively simple model we are able to at least make corrections to the diffusivity for the intrapore potential which are at least first order accurate.

Though it was not stressed in the earlier chapters, the explosive growth of parallel computational science has had important consequences for simulations. In this work it was

particularly easy to vectorize the simulation code due the assumption of non-interacting molecules, but with the current growth in the research in parallel computational algorithms, massively parallel computers will doubtless have application in all future simulation work

Bibliography

Monette, L., Grest, G.S., Anderson, M.P., 1994, Three-dimensional Ising System with Long Range Interactions: a Computer Model of Vycor Glass, *Phys. Rev. E*, **50**(5), 3361-3369

Appendix A

A Semi-analytical Technique for Describing Irreversible Fluid-Solid Reactions in Packed Columns

Published 1995, *A.I.Ch.E. J.* **41**(12) 2549-2555

A Semi-analytical Technique for Describing Irreversible Fluid-Solid Reactions in Packed Columns

Neil E. Fernandes and George R. Gavalas
Chemistry and Chemical Engineering Division
California Institute of Technology
Pasadena, CA 91125

Abstract

A semi-analytical technique is presented for solving the equations describing an isothermal ,irreversible reaction of a trace component in a packed bed of a solid reactant or adsorbent. The reaction rate expression is assumed to have an arbitrary dependence on the solid reactant concentration, but a first order dependence on the trace gaseous component. The technique relies on an integral transformation that reduces the set of partial differential equations to a set of two coupled ordinary differential equations in the spatial variables. Solving these two equations is simpler than solving the original equations by finite differences or finite elements, especially in the presence of steep concentration gradients. Two examples are presented to illustrate the technique; a progressive conversion model with reaction occurring at dispersed sites within the adsorbent pellet, and a reaction proceeding in the shrinking core mode.

A.1 Introduction

Adsorption or reaction in packed beds of solid reactants or sorbents is widely employed for the separation or purification of gases. The modeling of adsorption in packed beds has been treated extensively, and the textbooks of Ruthven (1984) and Yang (1987) provide an excellent introduction and detailed references.

We consider here the following equations describing the isothermal adsorption of reaction of a single trace component in a packed bed:

$$D_L \frac{\partial^2 c}{\partial x^2} - u\frac{\partial c}{\partial x} - \frac{\partial c}{\partial t} = \frac{(1-\epsilon)}{\epsilon}\frac{\partial q}{\partial t} \tag{A1}$$

This equation was solved analytically by Rasmuson and Neretnieks (1980) for the case where the sink term, $\frac{\partial q}{\partial t}$, was controlled by the external film resistance and intraparticle diffusion, with adsorption-desorption at equilibrium and a linear adsorption isotherm. The case of a nonlinear isotherm has been treated numerically by Liapis and Rippin (1978) among others. To our knowledge no analytical solution is available for irreversible adsorption or reaction with dispersed flow models.

In this paper we extend a semianalytical technique of Del Borghi *et al.* (1976) and Dudukovic and Lamba (1978), for fluid-solid reactions in single pellets to reactions in packed beds. This technique involves the transformation of the governing partial differential

equations (PDEs) into two coupled ordinary differential equations (ODEs). The technique is restricted to isothermal, irreversible reactions, first order with respect to the gaseous reactant. These conditions often apply when trace quantities of gaseous contaminants are removed by irreversible reactions or chemisorption. An example is the removal of hydrogen sulphide by reaction in a bed of iron or zinc oxide. The governing equations are similar to those of reversible adsorption and are amenable to numerical solution by collocation methods such as those used by Liapis and Rippin. The technique proposed here is simpler and numerically more efficient, especially when steep concentration gradients are encountered inside the pellets or along the bed.

A.2 Analytical Development

We consider a fluid-solid reaction

$$\nu_A A(f) + \nu_B B(s) \rightarrow \nu_P P(f) + \nu_Q Q(s) \tag{A2}$$

with rate per unit solid volume given by

$$R = kf(X)c' \tag{A3}$$

where c' is the concentration of the fluid component A per unit fluid volume in the pellet and X is the local conversion of the solid B. The form of the function f can be derived from various reaction models or it can be empirically determined.

The conservation equations for A and B for a bed of spherical pellets can be written as

$$D_L\frac{\partial^2 c}{\partial x^2} - u\frac{\partial c}{\partial x} = \frac{(1-\epsilon)}{\epsilon}\,\frac{3k_m}{R_p}\,(c - c'|_{R_p}) \tag{A4}$$

$$x = 0 \;:\; uc_0G(t) = uc - D_L\frac{\partial c}{\partial x} \tag{A5}$$

$$x = L \;:\; \frac{\partial c}{\partial x} = 0 \tag{A6}$$

$$D_e\frac{\partial}{\partial r}\left(r^2\frac{\partial c'}{\partial r}\right) = \nu_A k f(X) c' \tag{A7}$$

$$r = 0 \;:\; \frac{\partial c'}{\partial r} = 0 \tag{A8}$$

$$r = R_p \;:\; D_e\frac{\partial c'}{\partial r} = k_m(c - c') \tag{A9}$$

$$\frac{\partial X}{\partial t} = \nu_B k f(X) c' \tag{A10}$$

$$t = 0 \;:\; X = 0 \tag{A11}$$

These equations incorporate the following simplifications and assumptions:

1. The gas phase accumulation terms in the bed and pellet equations (A4) and (A7) have been neglected since in the adsorption/reaction of trace gases, the ratio of bulk gas concentration to solid reactant concentration $\left(\frac{c_o}{\sigma_o}\right)$ is very small, in many cases below 10^{-3}. For example, a copper-exchanged zeolite, 13-X containing 3 wt% Cu, i.e. σ_o

about 0.7 x 10^{-3} mol/cm^{-3} can be used to desulfurize a flue gas with 0.5% SO_2. At 300°C the SO_2 concentration is c_o = 1.06 x 10^{-7} mole/cm^{-7} so that $c_o/\sigma_o \simeq$ 1.5 x 10^{-4}.

2. The size and porous structure of the pellets do not change with reaction, excluding from consideration reactions such as lime sulfation which significantly decrease the pore volume.

3. Through the function $G(t)$ in equation (A5), time varying inlet concentrations have been included in the formulation of this problem. However $G(t)$ must change relatively slowly for consistency with the approximation 1 above.

Defining the dimensionless variables

$$\xi = \frac{x}{R_p} \ , \ \rho = \frac{r}{R_p} \ , \ \zeta = \frac{c'}{c_0} \ , \ y = \frac{c}{c_0} \ , \ \tau = \nu_B \frac{k c_0 t}{\sigma_o}$$

and the dimensionless parameters

$$Pe = \frac{u R_p}{D_L} \ , \ \beta = \frac{(1-\epsilon)}{\epsilon} \frac{3 k_m R_p}{D_L} \ , \ \Phi^2 = \frac{\nu_A k R_p^2}{D_e}$$

$$Bi_m = \frac{k_m R_p}{D_e}$$

the equations take the dimensionless form

$$\frac{\partial^2 y}{\partial \xi^2} - Pe\frac{\partial y}{\partial \xi} = \beta(y - \zeta|_{\rho=1}) \tag{A12}$$

$$\xi = 0 \;:\; g(\tau) = y - \frac{1}{Pe}\frac{\partial y}{\partial \xi} \tag{A13}$$

$$\xi = \Lambda \;:\; \frac{\partial y}{\partial \xi} = 0 \tag{A14}$$

$$\frac{1}{\rho^2}\frac{\partial}{\partial \rho}\left(\rho^2 \frac{\partial \zeta}{\partial \rho}\right) = \Phi^2 f(X)\zeta \tag{A15}$$

$$\rho = 0 \;:\; \frac{\partial \zeta}{\partial \rho} = 0 \tag{A16}$$

$$\rho = 1 \;:\; \frac{\partial \zeta}{\partial \rho} = Bi_m(y - \zeta) \tag{A17}$$

$$\frac{\partial X}{\partial \tau} = f(X)\zeta \tag{A18}$$

$$\tau = 0 \;:\; X = 0 \tag{A19}$$

The basic transformation consists of replacing the dependent concentration variable ζ by the cumulative pellet concentration

$$z = \int_0^\tau \zeta d\tau' \tag{A20}$$

Dividing equation (A18) by $f(X)$ and integrating yields the following relation between z and X

$$z = \int_0^X \frac{dx}{f(x)} \tag{A21}$$

Equation (A21) defines X implicitly as a function of z

$$X = w(z) \tag{A22}$$

Integrating equations (A15) – (A17) with respect to time we obtain the corresponding equations in the cumulative concentration z.

$$\frac{1}{\rho^2}\frac{\partial}{\partial\rho}\left(\rho^2\frac{\partial z}{\partial\rho}\right) = \Phi^2 w(z) \tag{A23}$$

$$\rho = 0 \;:\; \frac{\partial z}{\partial\rho} = 0 \tag{A24}$$

$$\rho = 1 \;:\; \frac{\partial z}{\partial\rho} = Bi_m(Y - z) \tag{A25}$$

where Y is the cumulative column concentration

$$Y = \int_0^\tau y(\xi, \tau')d\tau' \tag{A26}$$

In deriving equation (A23) we made use of the relation

$$w(z) = X = \int_0^{\tau} f(X)\zeta(\rho, \tau')d\tau'$$

obtained by direct integration of Eq. (A18). It is noted that the elimination of the dependent variable X from Eq. (A23) is possible only when the chemical reaction is first order in the gas concentration.

The solution to the two-point boundary problem (A23) – (A25) can be obtained numerically by integrating Eq. (A23) from the center of the pellet to the surface using the initial conditions

$$\rho = 0 \; : \; \frac{\partial z}{\partial \rho} = 0 \; ; \; z = \kappa \tag{A27}$$

for different values of κ and then using boundary condition (A25) to establish a one to one correspondence between Y and z at $\rho = 1$

$$z(1, Y) = h(Y) \tag{A28}$$

It is often useful to know the fraction of the sorbent that remains unreacted at breakthrough. In order to extract this information from the transformed equations, it is necessary to know the extent of conversion of the pellets as a function of Y. This can be found by integrating equation (A22) throughout the pellet

$$\sigma_{av}(Y) = 3\int_0^1 \rho^2(1 - w(z))d\rho \tag{A29}$$

where it is recalled that $z = z(\rho, Y)$. The functions $h(Y)$ and $\sigma_{av}(Y)$ summarize all the information contained in the pellet equations. The numerical solution provides $h(Y)$ and $\sigma_{av}(Y)$ at a discrete set of points, which can be interpolated using cubic splines to provide smooth functions.

Proceeding to the column problem, equations (Al2) – (A14) are integrated with respect to τ yielding

$$\frac{\partial^2 Y}{\partial \xi^2} - Pe\frac{\partial Y}{\partial \xi} = \beta(Y - h(Y)) \tag{A30}$$

$$\xi = 0 \;:\; \int_0^\tau g(t)dt = Y - \frac{1}{Pe}\frac{\partial Y}{\partial \xi} \tag{A31}$$

$$\xi = \Lambda \;:\; \frac{\partial Y}{\partial \xi} = 0 \tag{A32}$$

Using the initial conditions

$$\xi = \Lambda \;:\; \frac{\partial Y}{\partial \xi} = 0\,;\; Y = \lambda \tag{A33}$$

equation (A30) is integrated from $\xi = \Lambda$ to $\xi = 0$ for different values of λ. Each value of λ yields $Y(0, \tau)$ and $\frac{\partial Y}{\partial \xi}(0, \tau)$ as well as the cumulative concentration profile $Y(\xi, \tau)$. The

boundary quantities are substituted into equation (A31) to obtain the time τ for this particular profile. From the profile $Y(\xi,\tau)$ and the function $\sigma_{av}(Y)$, the concentration of solid reactant is immediately known everywhere in the column. To find the gas concentration profiles $y(\xi,\tau)$, the cumulative profiles $Y(\xi,\tau)$ could be numerically differentiated. However the numerical integration of equations (A30) – (A32) would yield Y at a non-equidistant set of values of τ, so that in practice it would be necessary to calculate the cumulative concentration profiles for a very dense set of values of τ to allow accurate numerical differentiation. A more efficient procedure becomes apparent by differentiating equation (A30) with respect to τ to obtain the linear equation

$$\frac{\partial^2 y}{\partial \xi^2} - Pe\frac{\partial y}{\partial \xi} = \beta[1 - h'(Y)]y \tag{A34}$$

subject to the boundary conditions (A13), (A14). Equation (A34) is linear because $h'(Y)$ is a known function of ξ through the cumulative concentration profile $Y(\xi,\tau)$. The function $h'(Y)$ can be obtained from the spline formulae used to generate $h(Y)$ but a more accurate method is given in the Appendix. By integrating equation (A34) from $\xi = \Lambda$ to $\xi = 0$ with the initial conditions

$$\xi = \Lambda \; : \; \frac{\partial y}{\partial \xi} = 0 \; ; \; y = \alpha \tag{A35}$$

a profile is obtained which differs from the true concentration profile only by a scaling factor. This profile can be scaled by a suitable constant so that the result $y(\xi,\tau)$ satisfies

boundary condition (A13).

It is useful at this point to summarize the computational procedure required to solve the original problem. First, the functions $h(Y)$ and $\sigma_{av}(Y)$ are calculated from the single pellet equations. In general, this involves solving the differential equation (A23) for several different values of $z(0, Y) = \kappa$. For certain fluid-solid reaction models the calculation of these functions may require solution of an algebraic equation rather than the differential equation (A23) (Example 2). Proceeding to the column equations, equations (A30) and (A34) need to be solved once for every concentration profile required. There is no requirement for a time mesh as with finite difference methods. One can solve for as few profiles as are needed to accurately portray the breakthrough behavior of the column.

Example 1.

The technique will now be illustrated for an irreversible reaction which is first order in both the gaseous reactant and the reacting sites in the solid. In this case the function f takes the simple form

$$f(X) = 1 - X$$

where the initial density of reacting sites is absorbed into the rate constant k. Equations (A21) and (A22) now appear as

$$X = w(z) = 1 - e^{-z}$$

The relevant forms of equations (A23) – (A25) were integrated by a Runge-Kutta method with adaptive step size control (RKAS) to calculate the function $h(Y)$. Figure 1 shows the calculated $h(Y)$ for various values of Φ. In practical applications, the mass transfer Biot number is sufficiently high and most resistance is due to intraparticle processes. For small values of Φ, intraparticle gradients are small and thus the cumulative concentrations in the bulk, Y, and at the particle surface, $h(Y)$, are similar. For large values of Φ, Y is significantly larger than $h(Y)$ as shown in Figure A.2. Figures A.2 through A.6 survey the results easily extracted through this method of solution. Figures A.2, A.3 and A.4 illustrate the development of the gas and solid concentration profiles in the bed. Note how the gas and solid concentration profiles at $\tau = 0.0$ in Figures A.3 and A.4 are consistent with the pseudo-steady state assumption. Figure A.3 reveals the wave-like character of the solution reflecting the relatively small effect of dispersive processes. Finally, Figures A.5 and A.6 show breakthrough curves for different values of various parameters. For the range of parameters explored, broadening effects caused by kinetic resistances in the pellet are seen to be much more important than those due to axial dispersion.

In this example the feed concentration to the column was taken as constant. However, the technique can be applied to unsteady inputs, subject to the restrictions of the pseudo-steady state approximation. In particular, the characteristic time for changes in the feed

concentration must be much larger than the characteristic time for concentration changes in the column and the pellet. Our experience with Example 1 indicates that the solution of equation (A34) is very sensitive to the function $h'(Y)$. Differentiation of the spline-interpolated function Y introduces sizable error especially for Thiele moduli below 1 or above 20. However, this difficulty was largely eliminated by using the direct calculation of $h'(Y)$ outlined in the Appendix. To test the numerical accuracy of the technique the numerical solution for short times was compared with the corresponding analytical solution obtained from the asymptotic form of equation (A34)

$$\frac{\partial^2 y}{\partial \xi^2} - Pe\frac{\partial y}{\partial \xi} = \beta A(Bi_m, \Phi)$$

where $A(Bi_m, \Phi)$ is a constant calculated from the short-time limiting form of the pellet equations. The two solutions differed by less than 1%. Overall mass balances based on the outlet tracer concentration-time curve also gave consistent results.

Example 2.

As pointed out earlier, functions $h(Y)$ and $\sigma_{av}(Y)$ can be calculated for a variety of reaction models. To further illustrate this calculation, we consider a pellet undergoing shrinking core reaction. Mass transfer through the gas film, diffusion through the product layer, and

reaction at the interface are described by the standard pseudo-steady state equations

$$r_c < r < R_p \quad : \quad \frac{D_e}{r^2}\frac{\partial}{\partial r}\left(r^2\frac{\partial c'}{\partial r}\right) = 0 \tag{A36}$$

$$r = r_c \quad : \quad D_e\frac{\partial c'}{\partial r} = \nu_A k c' \tag{A37}$$

$$r = R_p \quad : \quad k_m(c - c') = D_e\frac{\partial c'}{\partial r} \tag{A38}$$

$$\frac{d}{dt}(\sigma_o\frac{4}{3}\pi r_c^3) = -\nu_B k c' 4\pi r_c^2 \tag{A39}$$

$$t = 0 \quad : \quad r_c = R_p \tag{A40}$$

where c' is the concentration of the gaseous reactant, σ_o is the concentration of the solid reactant in the core and r_c, R_p are the radii of the core and the pellet. With the new definition of dimensionless time

$$\tau = \frac{\nu_B k c_o}{\sigma_o R_p}t$$

and Thiele modulus

$$\Phi^2 = \frac{\nu_A k R_p}{D_e}$$

equations (A36) – (A38) yield the following expressions for the dimensionless gradients at

the core surface and pellet surface

$$\rho = \rho_c \;:\; \frac{\partial \zeta}{\partial \rho} = \frac{\zeta(1,\tau) - \zeta(\rho_c,\tau)}{\rho_c(1-\rho_c)} \tag{A41}$$

$$\rho = 1 \;:\; \frac{\partial \zeta}{\partial \rho} = \frac{\rho_c[\zeta(1,\tau) - \zeta(\rho_c,\tau)]}{(1-\rho_c)} \tag{A42}$$

Equation (A41) is now introduced into equation (A39) to obtain

$$\frac{\partial \rho_c}{\partial \tau} = \frac{-\zeta(1,\tau)}{\Phi^2(1-\rho_c)\rho_c + 1} = -\zeta(\rho_c,\tau) \tag{A43}$$

After integration with respect to time equation (A43) appears in the familiar form

$$\Phi^2\left(\frac{\rho_c^2}{2} - \frac{\rho_c^3}{3} - \frac{1}{6}\right) + \rho_c - 1 = -z(1,Y) \tag{A44}$$

Matching the fluxes at the solid-fluid boundary gives

$$\rho = 1 \;:\; (Y - z) = \frac{1}{Bi_m}\int_0^\tau \frac{\rho_c}{1-\rho_c}[\zeta(1,\tau') - \zeta(\rho_c,\tau')]d\tau' \tag{A45}$$

which after substitution with equation (A43) and integration, provides the simple equation

$$Bi_m(Y - z(1,Y)) = \frac{\Phi^2}{3}(1-\rho_c^3) \tag{A46}$$

Equations (A44) and (A46) can be easily solved for ρ_c and $z(1,Y)$. For example, a value for z is selected and equation (A44) is solved for ρ_c, where only the root between 0 and 1 is

physically relevant. The values of z and ρ_c are then substituted into equation (A46) to give the corresponding Y. With Y, $z(1,Y)$ and ρ_c all known, one immediately has

$$h(Y) = z(1,Y) \tag{A47}$$

$$\sigma_{av}(Y) = \rho_c^3 \tag{A48}$$

As before cubic splines can be used to generate continuous functions. Figure A.7 shows breakthrough curves calculated for the progressive conversion model and the shrinking core models for high values of the Thiele modulus. In this case both models describe the same physical situation, namely reactions with steep intraparticle concentration gradients which explains the close agreement of the two breakthrough curves.

A further special case of some interest is one in which the reactive solid consists of small crystallites supported on an inert porous matrix. The mathematical structure of this problem is similar to that of the grain model. If reaction in the crystallites takes place in the shrinking core fashion, then the analysis of Example 2 can be combined with that of Example 1 to provide the function $h(Y)$ for the pellet. The function $h(Y)$ of the pellet is then used in the column equations. This procedure represents a compounding from one level to the next one: from the crystallite to the pellet and from the pellet to the column. Each such transition, from one level to the next, eliminates one spatial coordinate. For background material on shrinking core and grain models see Levenspiel (1972) and Szekely and Evans (1971).

A.3 Discussion and Conclusions

A previous technique of Del Borghi *et al.* and Dudukovic and Lamba dealing with a single spatial variable (single pellet) was extended to the case of two spatial variables (packed bed). This technique allows successive elmination of spatial variables from the smaller scale to the larger scale until only the spatial varilable at the highest level remains. Time is eliminated as an independent variable and becomes a parameter so that there is no need for a mesh in the time variable. Once the function $h(Y)$ has been computed for the pellet, only two one-dimensional spatial integrations are required for each time at which the solution is desired.

Transformation of the original partial differential equations to ordinary differential equations is advantageous because of the availability of very efficient numerical algorithms for the latter even when the solutions have steep gradients. For example the 4th order RKAS algorithm automatically reduces the integration step to handle steep gradients in the dependent variable. In typical finite element and finite difference techniques very dense meshes in time and space must be used in the vicinity of steep concentration fronts. Although moving finite element techniques have been developed to handle such problems, their implementation is considerably more tedious. The technique presented here is applicable only to a limited class of problems involving irreversible reactions, first order in the gaseous reactant and excludes reactions which significantly change the porous structure of the reacting solid.

A.4 Acknowledgement

Funding for this project was provided by the Advanced Development Activity for Microgravity Containerless Technology of the Jet Propulsion Laboratory.

A.5 Notation

Roman

B_{i_m} pellet mass transfer Biot number

c gas concentration in the bulk phase

c_o inlet or characteristic gas concentration

c' gas concentration in the pellet pores

D_e effective diffusivity within the pellet

D_L axial dispersion coefficient within the column

f dimensionless function summarizing the surface contribution in the rate expression R

G arbitrary function of time expressing the inlet concentration to the bed

h dimensionless function relating the cumulative concentrations Y and $Z(\rho = 1, \tau)$

h' derivative of h with respect to Y

k reaction rate constant

k_m mass transfer coefficient

L total length of packed bed

Pe pellet Peclet number

q concentration of solid product in the pellet

R_p pellet radius

r radial distance in pellet

r_c radius of unreacted core in the shrinking core example

t time

u interstitial velocity

X solid reactant conversion

x axial distance from front of bed

Y cumulative concentration in the bed

y dimensionless bulk concentration

z cumulative concentration in the pellet

Greek

β dimensionless number

ϵ bed void fraction

ξ dimensionless distance from front of bed

ζ dimensionless gas concentration within the pellet

Φ Thiele modulus

Λ dimensionless total bed length, L/R_p

ρ dimensionless radial distance within pellet

ρ_c dimensionless unreacted core radius

σ_{av} pellet average of the solid reactant concentration

σ_o initial solid reactant concentration

τ dimensionless time

τ_{ideal} dimensionless ideal breakthrough time

Bibliography

Del Borghi, M., Dunn, J.C., Bischoff, K.B., 1976, A Technique for Solution of the Equations for Fluid Solid Reactions with Diffusion, *Chem. Engng Sci.*, **31**, 1065

Dudukovic, M.P., Lamba, H.S., 1978, Solution of Moving Boundary Problems for Gas-Solid Noncatalytic Reactions by Orthogonal Collocation, *Chem. Engng Sci.*, **33**, 303

Liapis, A.I., Rippin, D.W.T., 1978, The Simulation of Binary Adsorption in Activated Carbon Columns using Estimates of Diffusional Resistance within the Carbon Particles Derived from Batch Experiments, *Chem. Engng Sci.*, **33**, 593

Levenspiel, O., 1972, *Chemical Reaction Engineering*, John Wiley and Sons, Inc., New York

Rasmuson, A., Neretnieks, I., 1980, Exact Solution for Diffusion in Particles and Longitudinal Dispersion in Packed Beds, *AIChE J.*, **26**, 686

Ruthven, D.M., 1984, *Principles of Adsorption and Adsorption Processes*, John Wiley and Sons, Inc., New York

Yang, R.T., 1987, *Gas Separation by Adsorption Processes*, Butterworths, Boston

Szekely, J., Evans, J. W., 1971, The Effect of Grain Size, Porosity and Temperature on the Reaction of Porous Pellets, *Chem. Engng Sci.*, **26**,1901

Appendix

A more accurate method for calculating $h'(Y)$ for the progressive conversion problem is as follows. The pellet equations for the cumulative concentration are

$$\frac{1}{\rho^2}\frac{\partial}{\rho}\left(\rho^2\frac{\partial z}{\partial \rho}\right) = \Phi^2 w(z) \qquad \text{(A49)}$$

$$\rho = 0 \; : \; \frac{\partial z}{\partial \rho} = 0 \qquad \text{(A50)}$$

$$\rho = 1 \; : \; \frac{\partial z}{\partial \rho} = Bi_m(Y - z) \qquad \text{(A51)}$$

These equations can be differentiated with respect to Y to obtain an equation in the derivative $v = \partial z/\partial Y$:

$$\frac{1}{\rho^2}\frac{\partial}{\rho}\left(\rho^2\frac{\partial v}{\partial \rho}\right) = \Phi^2 w'(z)v \qquad \text{(A52)}$$

$$\rho = 0 \; : \; \frac{\partial v}{\partial \rho} = 0 \qquad \text{(A5)}$$

$$\rho = 1 \; : \; Bi_m(1 - v) = \frac{\partial v}{\partial \rho} \qquad \text{(A53)}$$

With z known from the solution of (A49) – (A51), equations (A52) – (A54) constitute a linear boundary value problem in v and can be readily integrated. We have found that calculating v from equations (A52) – (A54) gives much more accurate results than those obtained by numerically differentiating $h(Y)$, especially for early times.

For the shrinking core model, significantly less work is involved. The pertinent equations from the main text are

$$\Phi^2\left(\frac{\rho_c^2}{2}-\frac{\rho_c^3}{3}-\frac{1}{6}\right)+\rho_c-1=-z(1,Y) \qquad \text{(A55)}$$

$$Bi_m\left(Y-z(1,Y)\right)=\frac{\Phi^2}{3}\left(1-\rho_c^3\right) \qquad \text{(A56)}$$

which result respectively from solving for the reaction front in the pellet and continuity of reactant flux at the pellet surface. By differentiating (A55) and (A56) with respect to Y and solving for $\frac{\partial z}{\partial Y}\,|_{\rho=1}$ the result is

$$\frac{\partial z}{\partial Y}\,|_{\rho=1}=\frac{1}{\left(1+\frac{\Phi^2\rho_c^2}{Bi_m\Phi^2\rho_c(1-\rho_c)+1}\right)}$$

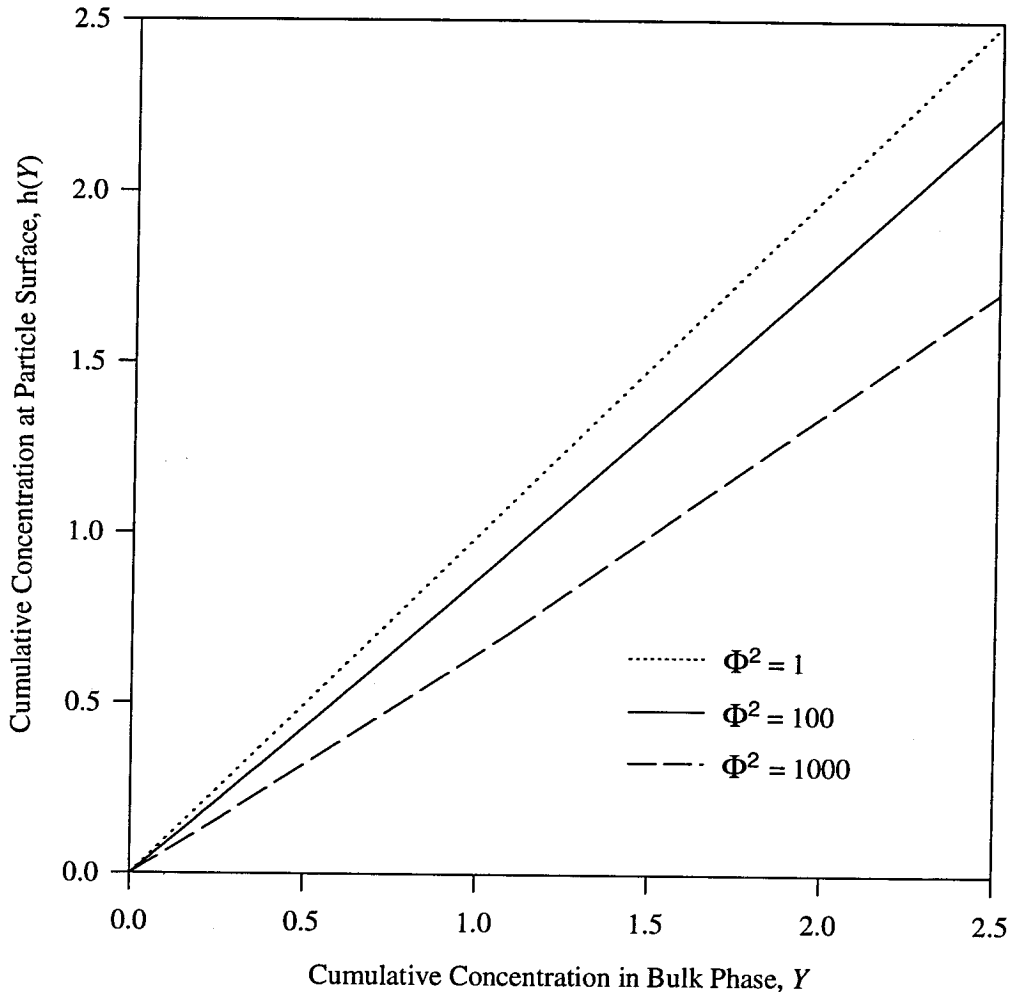

Figure A.1 The function h(Y) in Example 1 for $Bi_m = 50$ for various values of Φ^2

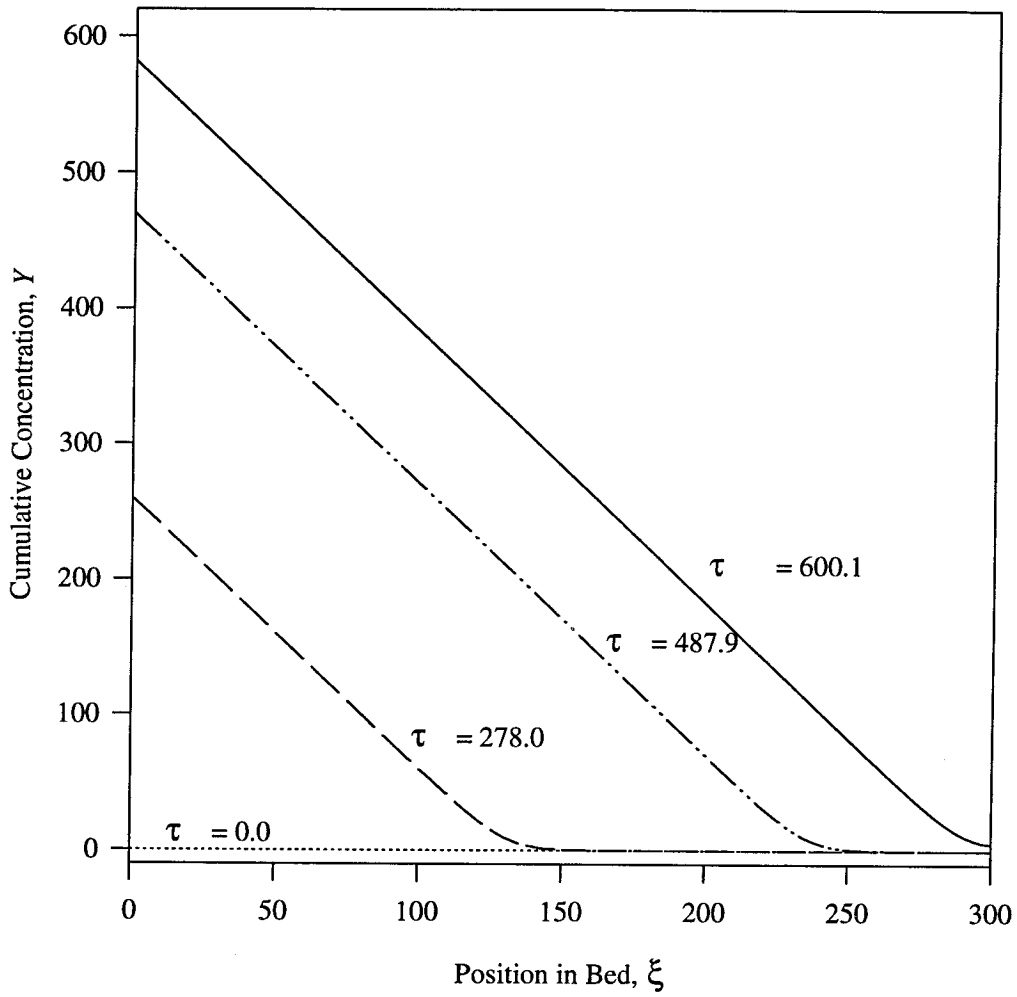

Figure A.2 Development of the cumulative concentration profiles $Y(\xi,\tau)$ in Example 1 for

$$\Phi^2 = 100,\ Bi_m = 50,\ Pe = 1.1,\ \beta = 3.3$$

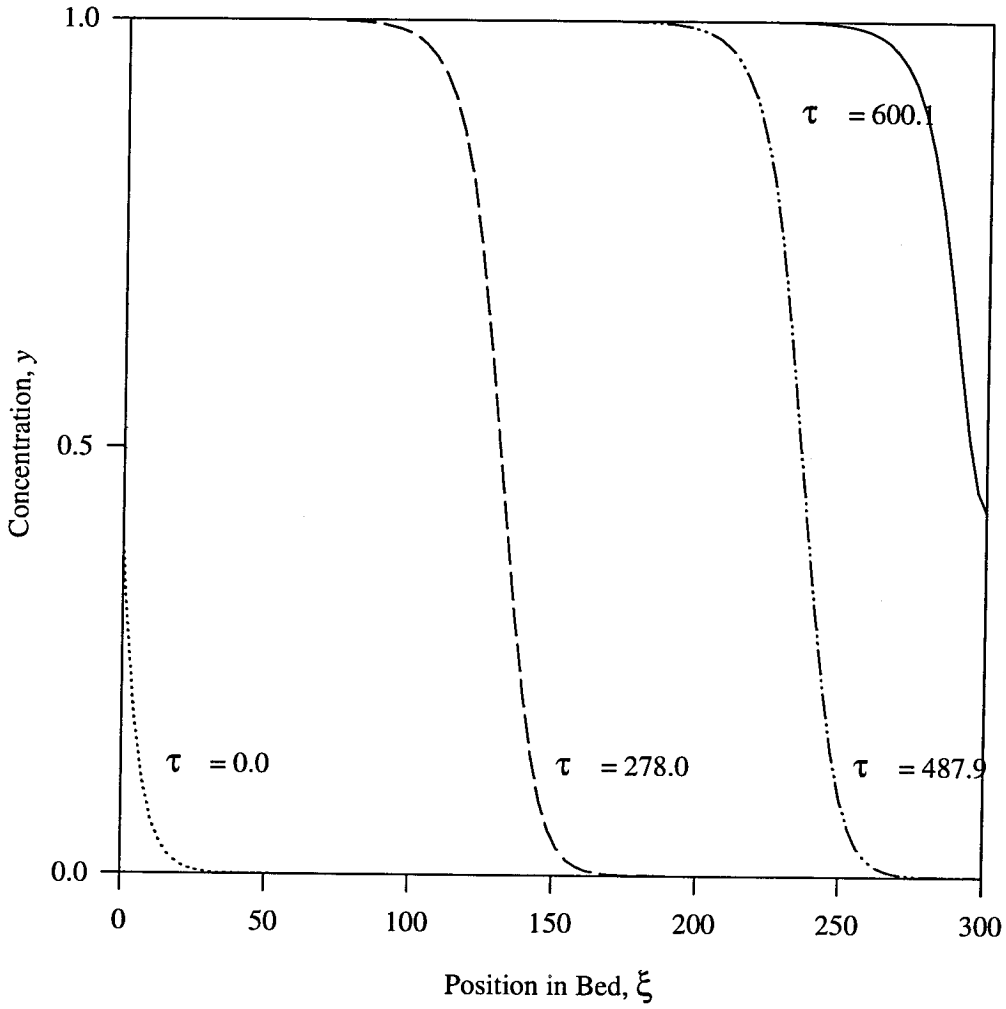

Figure A.3 Development of the concentration profiles $y(\xi,\tau)$ in Example 1 for $\Phi^2 = 100$,

$Bi_m = 50$, $Pe = 1.1$, $\beta = 3.3$

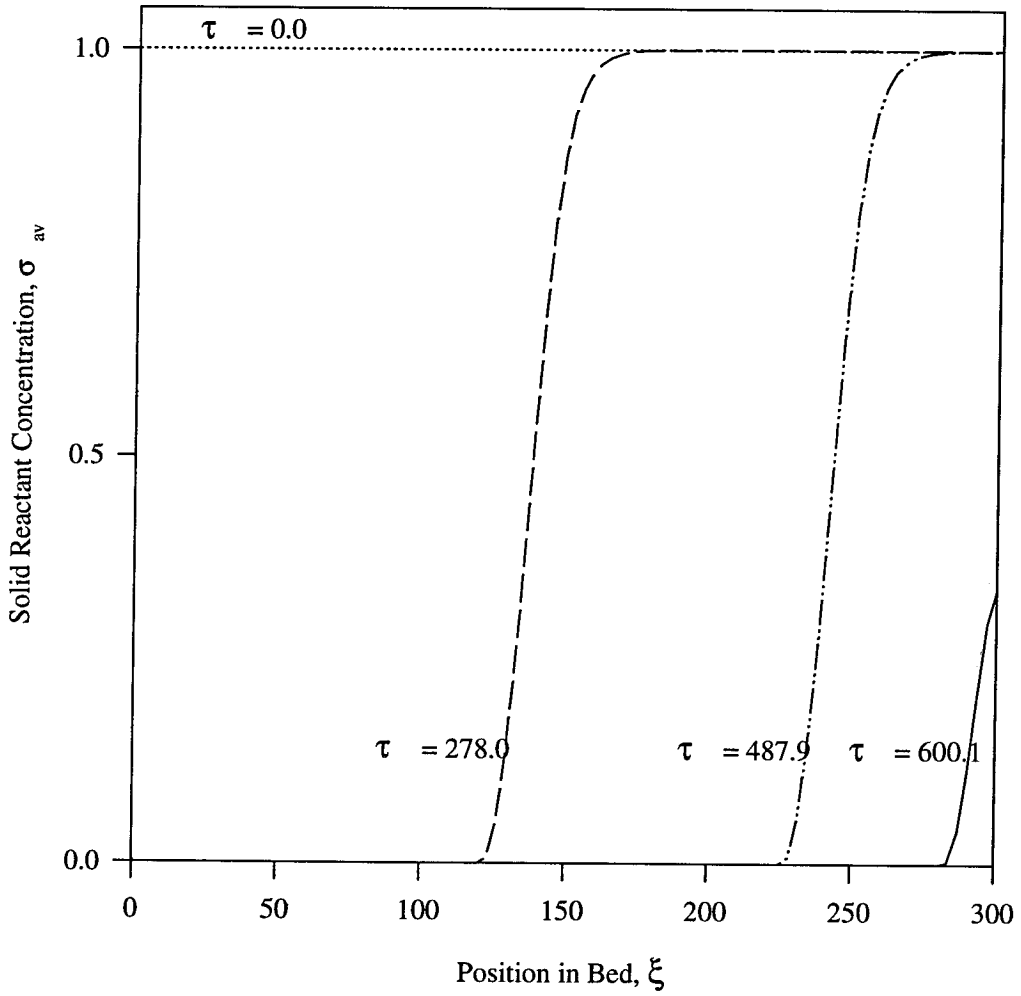

Figure A.4 Concentration profiles of the solid reactant in Example 1 for $\Phi^2 = 100$,

$Bi_m = 50$, $Pe = 1.1$, $\beta = 3.3$

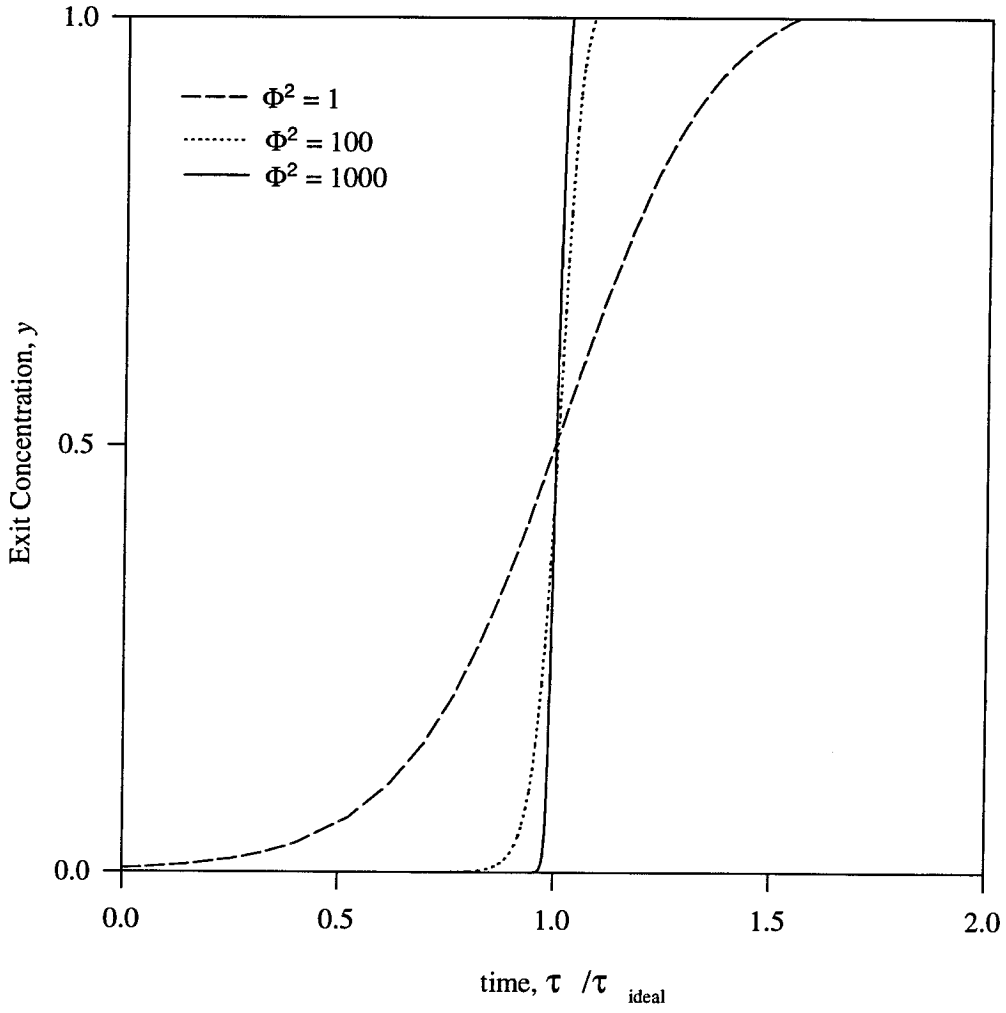

Figure A.5 The effect of reaction rate constant on the shape of the breakthrough curve in Example 1 for $Bi_m = 50$, Pe = 1.1, $\beta = 3.3$, L=300

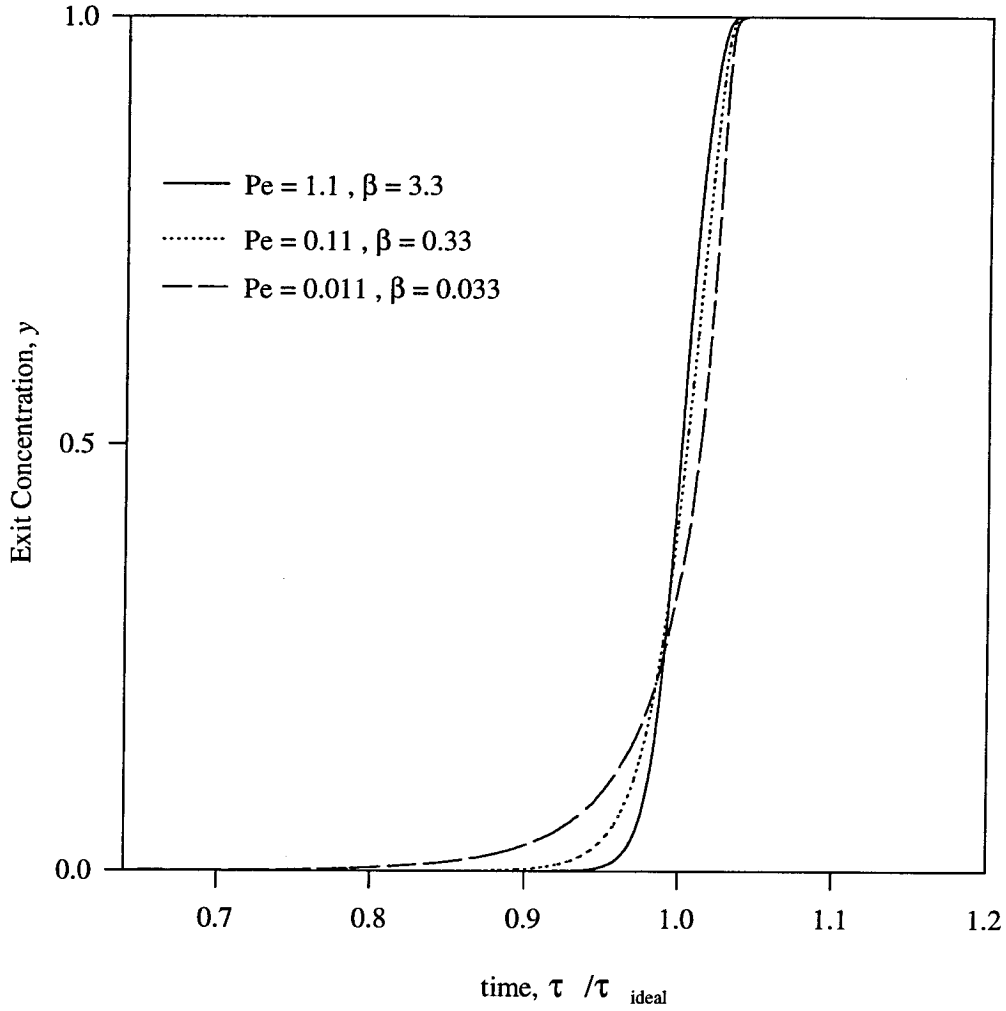

Figure A.6 The effect of axial dispersion on the breakthrough curve in Example 1 for

$\Phi^2 = 100,\ Bi_m = 50,\ L=300$

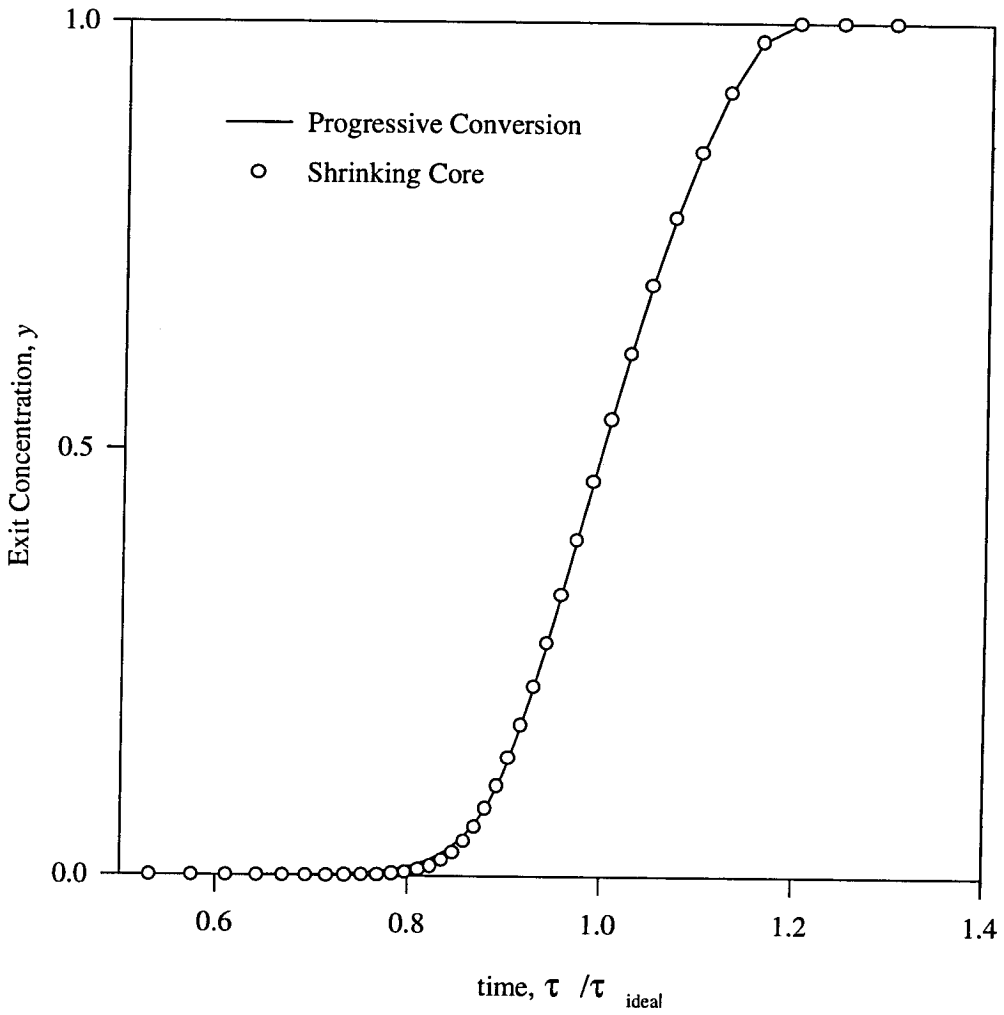

Figure A.7 Breakthrough curves for the progressive conversion model and the shrinking core model of Example 2 for $\Phi^2 = 100$, $Bi_m = 50$, Pe = 1.1, $\beta = 3.3$, L=300

Appendix B

Derivation of Mean Free Path Formulae in Chapter 3

B.1 Mean Free Path in a Slit with an Intrapore Potential (Section 3.2.1)

The logic of the derivation is to calculate the mean free paths of two groups of molecules

(1) Molecules which leave the wall but cannot escape the potential field and return to the surface.

(2) Molecules which leave the wall and eventually cross the slit and collide with the opposite wall

The velocity distributions for molecules emitted from the wall are given in the main text as

$$f_{xy}(v) = 2\pi v\left(\frac{m}{2\pi kT}\right)\exp\left(-\frac{mv^2}{2kT}\right) \tag{B1}$$

$$f_z(v) = \left(\frac{m}{kT}\right)v\exp\left(-\frac{mv^2}{2kT}\right) \tag{B2}$$

where f_{xy} is the distribution of speeds in the x-y plane. The velocity, v_z, of a molecule at any height, h, is calculated from the simple conservation of energy statement

$$\tfrac{1}{2}mv_{zo}^2 = \tfrac{1}{2}mv_z^2 + m\phi(h) \tag{B3}$$

To calculate the mean free path of molecules from group 1 we consider those molecules which only have enough energy to reach a height, *h*.. The time taken to reach this height is given by the integral

$$t = \int_0^h \frac{\mathrm{d}z}{\sqrt{2\phi(h) - 2\phi(z)}} \tag{B4}$$

and the distance traveled in the x-y plane by these molecules is simply $2v_{xy}t$. Integrating over v_{xy} gives the mean distance traveled in the x-y plane by those molecules which can only reach height *h*, as

$$\lambda_h = 2\sqrt{\frac{2kT}{\pi m}} \int_0^h \frac{\mathrm{d}z}{\sqrt{2\phi(h) - 2\phi(z)}} \tag{B5}$$

Letting $P(h)\mathrm{d}h$ be the *fraction* of total molecules emitted from the surface which are able to reach a height between h and $h+\mathrm{d}h$ and Q the fraction that escape the potential well altogether, then from the velocity distribution f_z, equation (B2)

$$P(h) = \alpha \frac{m}{kT} \frac{\mathrm{d}\phi}{\mathrm{d}h} \exp\left(-\frac{m\phi}{kT}\right) \tag{B6}$$

where α is a normalizing constant. Since

$$\int_0^H P(h)\,\mathrm{d}h + Q = 1 \tag{B7}$$

where

$$Q = \int_{\sqrt{2\phi(H)}}^{\infty} \left(\frac{mv}{kT}\right) \exp\left(-\frac{mv^2}{2kT}\right) dv \tag{B8}$$

the nomalization constant α is given by

$$\alpha = \frac{1 - \exp\left(-\frac{m\phi(H)}{kT}\right)}{\int_0^H \frac{m}{kT}\frac{d\phi}{dh}\exp\left(-\frac{m\phi}{kT}\right) dh} \tag{B9}$$

Integrating over h, the contibution to the mean free path from molecules not escaping the field is

$$\lambda_1 = \alpha\sqrt{\frac{\pi m}{kT}} \int_0^H \int_0^h \frac{dz}{\sqrt{\phi(h) - \phi(z)}} \frac{d\phi}{dh} \exp\left(-\frac{m\phi(h)}{kT}\right) dh \tag{B10}$$

The calculation for the contibution to the mean free path from molecules of group 2 is very similar. The mean distance traveled in the x-y plane by those molecules emitted with an initial velocity v_{zo} great enough to reach the midway point of the slit is

$$\lambda_{v_{zo}} = 2\sqrt{\frac{kT\pi}{2m}} \int_0^h \frac{dz}{\sqrt{v_{zo}^2 - 2\phi(z)}} \tag{B11}$$

Integrating over all molecules with velocities large enough to escape the field gives the following contribution to the mean free path.

$$\lambda_2 = 2\sqrt{\frac{m\pi}{2kT}} \int_{\sqrt{2\phi(H)}}^{\infty} v_{zo} \int_0^h \frac{dz}{\sqrt{v_{zo}^2 - 2\phi(z)}} \exp\left(-\frac{mv_{zo}^2}{2kT}\right) dv_{zo} \qquad \text{(B12)}$$

B.2 Random Walk in 1-D with Persistence of Velocity Effects (Section 3.3)

Consider a random walker able to move in either of the directions north or south, with a base step of λ. The mean distance traveled by the walker before he turns around is the effective step size Λ. In the usual 1-D random walk, after any step the walker can move north or south with equal probability, and the effective step size is simply λ. However if p is the probability that the walker continues in the same direction i.e.,

p = probability of the walker stepping south given that he has just come from the north
= probability of the walker stepping north given that he has just come form the south

and P_i is defined as the probability that the walker travels i steps before turning around, then

$$P_i = p^i(1-p) \tag{B13}$$

and the the effective step size is given by

$$\begin{aligned} \Lambda = & \sum_{i=1}^{\infty}(i\lambda)p^i(1-p) \\ = & (1-p)\lambda\sum_{i=1}^{\infty}\frac{\mathrm{d}}{\mathrm{d}p}\left(p^{i+1}\right)-p^i \\ = & \frac{p}{(1-p)}\lambda \end{aligned} \tag{B14}$$

Appendix C

Gas Phase Deposition Experiments

C.1 Introduction

Much of the effort associated with this project was spent investigating practical methods for achieving uniform silica deposition within the Vycor pores. To this end, three techniques were researched:

(1) Low temperature (25°C) deposition of silica from a liquid phase, using silicon tetrachloride ($SiCl_4$) as a precursor.

(2) Moderate temperature (300°C) deposition from the gas phase using the precursor tetraethyl orthosilicate (TEOS).

(3) High temperature (500°C) deposition from the gas phase, using the $SiCl_4$ precursor.

Details for silica deposition from the liquid phase have been presented in Chapter 2; this appendix describes the gas phase deposition techniques.

C.2 Pore Narrowing of Vycor Glass by Silica Deposition

C.2.1 Characteristics of Vycor®

All of the deposition experiments were performed with porous glass, however, it was made clear in Chapter 2, that there are a variety of gas-solid reactions in which pore structural changes occur. Nevertheless, to be ideal for an experimental investigation, there are certain characteristics which are desirable. Any candidate porous material should have some, if not all, of the following attributes. In the order of importance:

(1) It must be able to participate in a reaction causing the pore radii to either diminish or enlarge

(2) The dynamic pore reactions must be kinetically controlling in order to ensure uniform reaction throughout the sample. A single permeance measurement can then be ascribed to a particular level of conversion.

(3) For ease of analysis, an ideal cylindrical pore geometry is preferable so that models for cylindrical geometries can be applied with some degree of confidence. A narrow pore distribution is also advantageous in that one diffusion mechanism is applicable for all pores.

(4) The availability of the solid in macroscopic dimensions lends to experimental flexibility with regard to both the reactions and the permeance measurements.

Only the first two characteristics are essential, however, from its description in Chapter 2, it is clear that Vycor actually satisfies all of these requirements.

There is a disadvantage in using Vycor due to the brittle nature of glasses. In the permeance measurement experiments, it is necessary to bond or seal Vycor to an impermeable host , or substrate, such as fused silica glass. However, it is very difficult to meld Vycor with other materials and have the union stay intact over broad temperature ranges. In the case of sealing Vycor to glasses, this is usually due to a mismatch in the thermal expansion properties. It is possible to make a graded transition from Vycor to quartz and Pyrex glasses, a technique used in the fabrication inorganic membranes (Tsapatsis *et al.*, 1991), but the procedure is time consuming and expensive.

Another method for sealing and bonding Vycor makes use of glazes and resins. Torr-seal® by Varian is an epoxy based resin suitable in the temperature range of 25°C to 200°C. Inexpensive high temperature sealants other than glazes are not readily available. In our high temperature gas phase experiments (300-500°C) we were able to successfully use a leadsilicate based glaze to bond the Vycor tube sections to quartz glass. To cure the glaze the assembly must be heated to 700°C. As a result of this high temperature it is necessary to pre-treat the Vycor at 700°C for ~1 hour *before* sealing it to the quartz host tubes at room temperature. At temperatures above ~ 650°C, the smaller pores inside the Vycor start to collapse irreversibly causing a dramatic volume shrinkage, stressing the glass/quartz transition. By allowing these pores to collapse during the pre-treatment, such stresses can be avoided during the experiment. An oxygen sweep gas is used for at least the first two hours of the high temperature phases of the pre-treatment, and glaze curing treatment, in order to oxidize and remove organic contaminants.

Pre-treating the Vycor at temperature of 700°C has dramatic consequences for the surface silanol concentration and, therefore, also for any deposition techniques which exploit these silanol groups (Section C.2.4). For almost all types of silica, the concentration of silanols at a given temperature is regarded as a physiochemical constant. Accordingly, for samples pre-treated under vacuum, the total of vicinal pairs of silanols and isolated silanols is ~2.5 nm^{-2} at 200°C, compared with ~1.0 nm^{-2} at 700°C (Vansant *et al.*, 1995). Silanol pairs are here counted as one because, presumably, only one of the silanols will easily react with $SiCl_4$, the other site being blocked as a result of steric hindrance. It is possible to replenish the silanol concentration by boiling in water (hydroxylation). Table C.1 summarizes the results of gas phase experiments with $SiCl_4$ and water, performed to determine the sensitivity of the Vycor surface silanol concentration to temperature pre-treatments. The samples were pre-treated at the stated temperature for ~2 hours.

Sample Size	Pre-treatment Temperature/°C	Hydroxylation Time/hrs	Reaction Temperature/°C	% Weight Change After: Silylation	Hydrolysis	Ratio of Weight Changes
~5mm	none	none	500	6.13	3.61	1.70
~5mm	none	10	500	6.29	3.79	1.66
~5mm	750	none	500	2.93	1.76	1.66
~5mm	750	10	500	4.67	2.68	1.74
~5mm	750	24	500	5.65	3.82	1.48
100μm	none	none	550	5.69	3.32	1.71

Table C.1 Weight changes of Vycor samples having undergone different pre-treatments.

C.2.2 Silica Deposition from the Gas Phase

In Chapter 2, the liquid phase deposition procedure was used to deposit a silica film on the pore walls, but it was also mentioned that the deposition could be achieved from the gas phase. To this end, a novel reactor, with the ability to measure the deposition progress and resulting permeances *in situ*, was designed and assembled (Figure C.1). Detailed schematics appear in Section C.3. The reaction progress is inferred from the weight change of a Vycor sample suspended from a sensitive weighing balance (resolution 0.1 μg). Gas permeances through the Vycor/quartz glass tube assembly are measured using a quadrapole mass analyzer (QMA).

Most of the experimental procedure was derived from the work on inorganic membranes by Tsapatsis *et al.* (1991) and Kim and Gavalas (1993). With the QMA physically disconnected from the quartz glass reactor, the reactants are admitted to the reaction chamber in the form of saturated vapors using a nitrogen carrier gas, whereupon they are further diluted by a nitrogen sweep stream, and swept into the high temperature zone of the reactor. Gas concentrations in the reactor are controlled either through the flowrates of the nitrogen carrier and sweep gases, or through the temperature of the bubblers. The nitrogen sweep gas is essential for protecting the weighing balance from possibly corrosive

chemicals. Once inside the reaction zone, the reactants diffuse into both the suspended Vycor sample, and the mounted Vycor tube, and react with the pore surfaces. *It is assumed that deposition occurs to the same extent in both pieces.* After a certain amount of deposition is achieved the flow of reactants is stopped and the reactor prepared for permeance measurements by purging the reactor with pure nitrogen for several minutes, evacuation, and finally pressurization with the permeating (or probe) gas mixture. The QMA is then reconnected to the reactor for the permeance measurements. The actual measurement procedure is complicated and the reader is referred to Section C.4 for details. After the permeance measurements have been made, the QMA is again disconnected and the deposition reaction restarted.

C.2.3 Silica Deposition using the TEOS Precursor

At temperatures above 200°C, tetraethylorthosilicate or TEOS, reacts both heterogeneously and homegeneously forming silica. To inhibit the gas phase reaction, low gas concentrations are used with the result that TEOS pyrolyzes only on the Vycor pore surface forming a film of silica. This silica film is usually contaminated with hydrocarbon fragments. There has been an enormous amount of investigation into the CVD of silica by TEOS pyrolysis because of its pertinence to the semi-conductor industry. Raupp *et al.* (1992) presented experimental evidence in favor of a heterogeneous deposition mechanism initially suggested by Schlote *et al.* (1991). Silica deposition proceeds through the heterogeneous decomposition of adsorbed TEOS while re-adsorption of the gaseous byproducts onto the growing surface film surface is assumed to inhibit further deposition. The resulting rate equation, in the limit of low TEOS concentration, reduces to a simple first order rate equation. Uniform deposition then, requires that the Thiele Modulus, $(k_r L^2/D_e)^{1/2}$ be much less than unity. One can show, using an order of magnitude analysis, that in order for the deposition to be uniform the rate of weight gain must be approximately 0.003mg min^{-1}. In practice this is a very inconvenient rate requiring tens of hours of

reaction time in order to achieve pore radius changes of only a few angstroms. Moreover, because the reaction is not self-limiting, as is the case for deposition from the $SiCl_4$ precursor, the transport dynamics become especially important. Reviewing the diagram in Figure C.1 again, it is clear that if we are to infer the degree of deposition in the mounted sample from the weight change of the suspended sample, the mass transfer coefficients are required to be the same for both.

A series of experiments at 300°C were attempted with the aim of uniformly narrowing the pore size. A TEOS concentration of ~0.4% by volume and an average deposition rate of 0.004 mg min^{-1} was used. The pore size distribution of both the suspended Vycor sample and the mounted Vycor tube, illustrated in Figure C.2, is a good indication that silica was being uniformly deposited, however, it also obvious that the deposition rates in the two Vycor pieces cannot have been the same. This is believed to be a result of the complex flow fields around the two samples. Owing to the high temperatures, there are significant convective flows within the reaction zone, which most probably cause different mass transfer coefficients for the two Vycor pieces. In retrospect, a better reaction scheme is to let the reactants enter from the bottom so that they flow in the same direction as the convection currents. The TEOS also has access to both the inside and outside of the suspended Vycor, whereas it can only access the outside tube surface of the mounted Vycor. Owing to the difficulty in guaranteeing that the two Vycor pieces undergo deposition under identical conditions, the TEOS experiments were abandoned. Nevertheless the porosimetry results do demonstrate that it is possible to deposit silica inside Vycor pores using this precursor.

C.2.4 Silica Deposition using Gas Phase $SiCl_4$

As already pointed out in Chapter 2, macroscopically uniform layers of silica can be deposited by alternatively reacting $SiCl_4$ and H_2O with the pore surface. This type of

deposition, achieved by an alternating reactant scheme, is also known in the literature as *chemical surface coating*. Vansant *et al.* (1995) describe such a procedure for the deposition of a silica nitride films on a glass surfaces from the reactants NH_3 and $HSiCl_3$.

In a preliminary experiment this deposition technique was used to narrow the pores of powdered Vycor glass (~100μm in size) at a reaction temperature of 550°C. This particular temperature was chosen for the high reaction rate. The weight trace for the duration of the experiment (Figure C.3) indicates pore closure (with regard to the transport of $SiCl_4$) to have occurred after 14 deposition cycles corresponding to a weight gain of ~28%. Typical reactant gas concentrations are shown in Figure C.1.

Just as for deposition from the liquid phase, only 6-7 deposition cycles could be performed from the gas phase before the Vycor tube samples cracked. It was initially thought that this fracturing was a result of stresses at the seals. However, the fragmenting of the Vycor in liquid phase experiments, where no sealing is necessary, suggest that the fractures are actually caused by internal stresses in the deposited film.

C.3 Experimental Apparatus and Design Schematics

The initial chemical vapor deposition (CVD) experiments were performed in a custom built reactor. The system is comprised of three distinct parts; the reaction chamber and thermogravimetric analyzer (CVDR and TGA respectively, Figure C.4), and the residual gas analyzer (RGA, Figure C.5).

The reactor is designed to allow the progress of a reaction to be measured *in situ*. To this end two measurements are available, the weight of the sample, as measured by the TGA, and the effluent gas composition as measured by the RGA. Much of the experimental method pertinent to our particular application has already been discussed, but to briefly

summarize : in our experiments the reaction progress is monitored by the sample weight change and the RGA is only used to measure probe gas permeances. Silicon tetrachloride, $SiCl_4$, or tetraethylorthosilicate, TEOS, is admitted to the reaction chamber before being further diluted by the nitrogen sweep stream. Reaction or deposition occurs simultaneously in the porous Vycor tube and the Vycor sample. In the case of silica deposition using the $SiCl_4$ precursor, the two reactants $SiCl_4$ and H_2O are admitted to the reactor in alternate cycles. In either case the weight change of the suspended Vycor sample is an indication of the degree of reaction. After a sufficient level of reaction has been completed, the reaction chamber is evacuated and the permeating probe gas mixture admitted. The gas permeances are subsequently measured using the RGA.

C.3.1 The Reaction System

Figure C.4 illustrates the essential components of the reactor. The weight measurements are performed by a Cahn D200 Weighing Analyzer, supplied by ATI Instruments, and are recorded on an Intel 486DX/66 based PC. The temperature in the AST furnace is controlled by a CN2011 Omega temperature controller. For flexibility the reactor tube is actually a two part assembly. The reactant inlet section is made from Pyrex glass for ease of fabrication, but to allow high temperatures in the furnace, the reactor section is made from quartz glass. The two sections are fastened together via an o-ring joint. The two part reactor design allows modifications to be made to the reactor at minimal expense.

In standard operation the CVDR/TGA system is physically disconnected from the RGA vacuum system when reactions are in progress. This precaution is necessary to keep the RGA system clean and free from any corrosive chemicals. The standard reactor outlet however is connected by a 3-way valve to a Leybold DB 1.6B vacuum pump allowing the rough degassing of samples, low pressure reaction or permeation, and the efficient purging

of gases from the reactor. The last feature is particularly important for permeance measurements using the RGA.

Typically a nitrogen carrier gas passes into temperature controlled bubblers containing the appropriate liquid phase chemical and becomes saturated before entering the reactor via a heated inlet tube. Omega 6102H (on/off) temperature controllers are sufficient for maintaining a constant bubbler temperature. A nitrogen sweep gas ensures that the weighing balance is not contaminated with any corrosive chemicals. Many of the chemicals used throughout this study are highly reactive towards water and thus the carrier and sweep gases each pass through a drierite ($CaCl_2$)/zeolite (Z4A) column before entering the bubblers.

C.3.2 The Residual Gas Analyzer

The heart of the RGA system shown in Figure C.5 is the 100C quadrapole RGA supplied by UTI Instruments. Data is recorded on an Intel 486DX/66 based PC via a UTI Spectralink and the proprietary software Spectrasoft 1.2. As already pointed out the RGA system is a physically distinct system from the CVDR/TGA. The system was designed to measure very low gas flow rates. Because mass spectrometers (MS) systems are sensitive to the actual individual molecule types and not the macroscopic properties of the gas mixture the RGA also has the ability to measure the partial pressures of gases in a mixture. This type of discernment can also be achieved by gas chromatography (GC). GC and MS are complimentary measuring techniques. On the one hand GC is not able to efficiently separate some of the lower molecular weight gases, a task requiring no extra effort using MS. On the other hand quantitative analyses of large molecular weight organics become extremely complicated using MS, but for the GC the analysis is straightforward. In the experiments, permeance measurements were performed using a gas mixture comprising 10% by volume of H_2, and 30% each of N_2, CH_4 and SF_6.

The RGA vacuum system is assembled from predominantly stainless steel components obtained from Swagelok. 1/4"VCR face sealing fittings are generally used to allow any future modifications to be easily made. In typical high vacuum work relatively large (~1") fittings are used to avoid throttling the pumping capacity, however the pump speed of the Leybold D4A (127 l min^{-1}) is sufficiently high to allow us to avoid using the larger more expensive fittings. All of the rotary vane vacuum pumps are fitted with Kurt J. Lesker micromaze traps.

The vacuum system can be broken up into a rough vacuum (>10^{-3} torr) chamber and a high vacuum chamber (10^{-5}-10^{-7} torr). These sections are separated by the 40μm orifice. In order to make a measurement of gas permeance, the permeating gas is mixed with a small known flow of argon controlled by the Accu-flo metering valve. The partial pressures of the gases in the rough vacuum side are proportional to their flow rates, and so by measuring the partial pressures of the gases in this chamber we can use the relationship

$$\frac{P_{\mathrm{Ar}}}{Q_{\mathrm{Ar}}} = \frac{P_i}{Q_i} \qquad \text{(C1)}$$

to deduce the flow rates and subsequently the permeances of the other gases. During the permeation measurements most of the permeating gas is pumped out by the D4A vacuum pump but a small amount is allowed to effuse through the orifice. Measuring the partial pressures is not straightforward and will be discussed in detail in the next section.

C.4 Quantitative Measurements Using the RGA

C.4.1 Overview of the Quadrapole Mass Filter

All mass spectrometers are comprised of an ionizer, some type of mass filter, and a detector.

In the ionization section the sample is typically bombarded with electrons (electron ionization, EI) . In the dominant ionization process the high energy emitted electrons collide with electrons in the sample molecules stripping them from their molecular orbitals. As a result mostly positive ions are produced. In the collision process the ionized molecule is highly energized and can fragment further into daughter ions. For example the molecule SF_6 does not produce SF_6^+ ions but the daughter ions SF_5^+, SF_4^+ etc. All of the ions are accelerated into the mass filter section which only ions of a particular mass-charge ratio are able to traverse. The resulting ion current can be measured using a variety of detectors.

The most basic detector, the Faraday cup, is essentially a thin plate of stainless steel which collects the ions. The detector output is then amplified with a high input impedance operational amplifier. The Faraday cup is inexpensive, electrically and mechanically simple and offers a response that is independent of the ion mass or other variables, however it has very low sensitivity because it does not provide any internal amplification. For this reason all modern mass spectrometers utilize an electron multiplier detector. In the 100C Precision Mass Analyzer, used in our experiments, a continuous dynode multiplier (Channeltron®) is employed. In this particular detector a ~2keV potential difference is applied across a long trumpet-shaped channel. Ions impacting with the entrance eject electrons which skip along its surface, each collision causing large emissions of secondary electrons. The entire electron flow is collected at its end. Gains of ~100000 are easily achieved. The advantages of electron multiplier detectors is their stability and high internal amplification. There are

two major disadvantages in that the efficiency of the secondary electron emission depends on the ion, decreasing as its mass increases, and that the performance of the detectors change with time due to deposition of materials from the ion stream and gas samples. In particular back streaming pump oil can coat the detector surface destroying its amplification performance altogether. At one stage during our investigation, the sensitivity of the Channeltron® deteriorated to the point where it had to be removed for cleaning. The performance was revived by a short (~10 min) ultrasonic treatment in acetone and ethanol.

The defining element of a mass spectrometer is its filter. In the quadrapole mass filter (QMF) based spectrometer instead of using a constant magnetic field to select a particular mass-charge ratio as used in the more familiar sector mass spectrometers, a varying electric field is applied to four precisely machined and aligned metal rods (hence the name). The QMF based spectrometers are thus referred to as dynamic mass analyzers. The principle of the QMF is that by applying a dc potential of magnitude U and a radio frequency (rf) potential $V\cos\omega t$ to opposite pairs of rods an electric field is set up such that ions moving between and along the axis of the rod experience a combination of forces causing them to undergo oscillations. Except for ions of a particular mass-charge ratio, the oscillations increase indefinitely in amplitude eventually causing the ions to collide with the rods. Typical values for U and V are 500V and 3kV, and rf frequencies are between 0.5 and 3 MHz. In a sector mass spectrometer scanning is achieved by changing the magnetic field or kinetic energy of the ions. In the QMF scanning is achieved by keeping the rf frequency and the ratio U/V constant while linearly increasing the dc and rf potential amplitudes.

For reasons of low cost, simplicity, capability of rapid scanning, tolerance of relative high pressures the QMF has become one of the most widely used mass filters (Strobel and Heineman,1989)

C.4.2 Quantitative Measurements

Despite the high sensitivity for individual molecules and the fast response times of the mass spectrometer, quantitative measurements are not easy to achieve. In the simplest calculation one might assume that the ion currents measured are proportional to the partial pressures in the ionization chamber, and further that this proportionality constant is the same for all ionic species. Calculations based on this procedure are usually in error ~600%! This is not surprising however, we have already mentioned that the electron multiplier detector is very sensitive to the mass of the ionic species. It is also necessary to take into account transmission efficiencies through the mass filter, and ionization efficiencies, both of which depend on the chemical components being analyzed. Transmission factors decrease non-linearly as the mass-charge ratio increases, whereas the ionization efficiency is usually assumed to be a linear function of the number of electrons in the molecular species. However even applying these corrections errors of ~100% are not uncommon.

The most accurate way to determine partial pressures is by direct, comparative calibration. Essentially this requires measuring the ion current signal for each gas at different partial pressures, a laborious task. Such calibration curves must be made every time a permeation experiment is run because the experimental system is not static over significant periods of time. The gain and basic sensitivity of the analyzer can change even during experiments. We have already discussed that deposits will cause the performance of the electron multiplier to deteriorate, but it is also possible for the basic sensitivity to change if the ionization filaments change position slightly. Such an event is quite possible during start-up, or if the mass spectrometer is used at relatively high pressures. Another aspect that must be considered is that the transmission characteristic of the 40μm orifice dividing the high and rough vacuum chambers is also dynamic. During routine maintenance of the vacuum system, deposits were noticed by microscopy to partially obstruct the pinhole of

the orifice plate. It is not clear exactly where these deposits came from, but we can speculate that they were probably reactants used in the silica deposition experiments. Because of the extreme labor that would be required to make calibration curves for all the permeating gases after every experiment, and to avoid having to accommodate several types of calibrating gas cylinders, the following procedure was devised for making permeation measurements using only a single gas mixture.

Figure C.6 illustrates again the RGA schematic shown in Figure C.5 but with all the valves re-numbered for the experimental description. The figure also indicates the normal configuration of the valves.

Step 1 Permeation measurement.

It is first necessary to set the required argon flow rate. The flow across valve 2 is choked and thus is only determined by the upstream pressure and valve stem position. With valves 4, 7 and 8 open and valves 10 and 11 shut, valve 2 is partially opened. At an appropriate instant valve 7 is shut and the pressure rise rate measured. Given that the volume of the rough vacuum chamber is 31.1 cm^3 this rise rate can be converted into an argon flow rate. In our measurements a flow rate of ~3.5×10^{-3} cm^3s^{-1} (STP) was found to be satisfactory. With the flow rate set, valve 10 is now opened and the permeating gas flow allowed to mix with the argon flow. The flow through valve 8 is adjusted so as to obtain a pressure in the chamber less than 0.4 torr. This is necessary in order to maintain a low pressure (~10^{-5} torr) in the high vacuum chamber. At this pressure free molecular flow occurs through the orifice. Although it may not be obvious now it will become apparent later that this condition is also best for the calibration. After a few minutes, valve 9 is opened and using the selected peak monitoring function in the Spectrasoft software the ion currents are measured for a few minutes.

Step 2 Evacuation

Once the permeation measurement is finished and the ion currents recorded valves 9, 2, and 10 are closed and valve 11 is opened. The throttling valve 8 is now fully opened to allow the rough vacuum chamber to be quickly pumped down.

Step 3 Making the calibrating gas mixtures

The calibration procedure involves mixing prescribed amounts of argon with the probe gas mixture to achieve various calibrating concentrations . To accomplish this there are two controlling elements available namely valve 2 and valve 7.

The first calibration mixture has an extremely low concentration of argon. This can be achieved as follows. Valves 3 and 7 are shut and the volume before valve 5 is filled with the probe gas. Valve 5 is then opened and the rough vacuum chamber (now with the mixing volume connected) is filled up to a pressure P^{in} of ~1.9 torr using valve 7 to reconnect the vacuum and pump the system down again if necessary. Valve 11 is subsequently closed. Argon is then allowed to flow via valve 2 into the chamber, building the pressure P^{fin} up to ~2 torr. At this stage the mixing volume is reconnected. It is necessary to wait ~10 minutes to guarantee that the concentrations in the rough vacuum chamber are uniform. Valve 7 is opened to allow the pressure of the chamber to be pumped down to ~0.2 torr. Valve 9 is subsequently opened to allow the ion currents to be measured. The mole fractions can be calculated using the following formulae

$$x_i^{fin} = \frac{x_i^{in} P^{in}}{P^{fin}} \tag{C2}$$

$$x_{Ar}^{fin} = \frac{x_{Ar}^{in} P^{in} + P^{fin} - P^{in}}{P^{fin}} \tag{C3}$$

where x represents the mole fractions, the superscript *in* signifies the condition before mixing with argon and the superscript *fin* the condition after mixing. For instance in our

experiments the probe gas mixture consisted of 10% by volume H_2, and 30% each of N_2, CH_4 and SF_6. and using the exact prescription just described the mole fractions would be calculated as

Gas	*Mole Fraction*
H_2	0.095
N_2	0.285
CH_4	0.285
SF_6	0.285
Ar	0.050

Table C.2

The idea now is simply to continue making calibration mixtures until the ion currents obtained in the permeation measurements are bracketed. One can then linearly interpolate to find out what partial pressure causes a particular ion current.

The second calibration mixture is made using the previous mixture as a starting point. Valve 9 is shut and valve 7 is opened pumping the chamber pressure down to ~0.1 torr, or half the initial pressure. Valve 7 is subsequently closed and valve 2 used to build up the pressure back up to 0.2 torr with argon. After about 5 minutes of equilibration valve 9 is again opened and the ion currents measured. Again using this prescription the mole fractions would be calculated as

Gas	*Mole Fraction*
H_2	0.0475
N_2	0.1425
CH_4	0.1425
SF_6	0.1425
Ar	0.5250

Table C.3

This procedure is continued until all of the permeation gas partial pressures have been obtained.

There are some experimental points that should be addressed. Clearly the calibrating gas mixtures used are not identical in composition to the gas mixture used for measuring the gas permeances. The consequences of this are minimized by ensuring that free molecular flow exists in the orifice. The ion currents depend on the pressure in the ionization chamber and this in turn depends on the flow characteristics through the orifice. In the free molecular flow region, the effusion rate of a particular gas depends only on its partial pressures on either side of the orifice. In bulk flow, transport through the orifice will depend on the viscosity of the mixture and thus on its *entire* composition.

In this particular setup a 1 liter mixing volume is used. One of the disadvantages of using free molecular flow is that the orifice actually causes separation, since the rate of effusion for a particular gas depends on its mean squared velocity. It can be shown that using a volume of 1 liter the time constant for concentration changes caused by the effusion is ~10 minutes. More accurate results can be obtained if a larger mixing volume is used. Using our particular setup and by comparing permeation results against those found using the

simple permeance method described in Chapter 2, we estimate the uncertainty in the concentration measurements to be from 5-10%.

Up to this point valves 13 and 14 have not been mentioned. They are not used in experiments but in the shut down of the RGA system. Once the vacuum pumps on the high vacuum side have been shut off, either deliberately or because of a power cut, it is necessary to break the vacuum in order to stop any pump oil from being drawn up into the chamber. In such an event the solenoid valve 13 is opened. Because of the relatively high fractions of water and organic substances in the ambient air however it is not wise to open the chamber to the atmosphere . Water is very hard to degas and pump oil has particularly deleterious effects on the electron multiplier. For this reason a nitrogen cylinder is connected via the solenoid valve to the high vacuum chamber. Valve 14 is used, just before shut down, to purge the line from any contaminants that may have diffused inside the line.

Bibliography

Kärger, J., Ruthven, D.M., 1992, *Diffusion in Zeolites and Other Microporous Materials,* John Wiley& Sons, Inc., New York

Kim, S., Gavalas, G.R., 1993, Kinetic Study of the Reactions of Chlorosilanes with Porous Vycor Glass, *J. Colloid Interface Sci.*, **161**(1), 6-18

Raupp, G.B., Shemansky, F.A., Cale, T.S., 1992, Kinetics and Mechanism of Silicon Dioxide Deposition through Thermal Pyrolysis of Tetraethylorthosilicate, *J. Vac. Sci. Technol. B*, **10**(6), 2422 -2430

Schlote, J., Schröder, K.W., Drescher, K., 1991, *J. Electrochem. Soc.*, **138**, pg 2393

Strobel, H.A., Heineman, W.R., 1989, *Chemical Instrumentation: A Systematic Approach*, 3rd edn, John Wiley and Sons, Inc., pg 686

Tsapatsis, M., Kim, S., Nam, S.W., Gavalas, G.R., 1991, Synthesis of Hydrogen Permselective SiO_2, TiO_2, Al_2O_3, B_2O_3 Membranes from the Chloride Precursors, *I & EC Res.*, **30**, 2152-2159

Vansant, E.F., Van Der Voort, P., Vrancken, K.C., 1995, *Characterization and Chemical Modification of the Silica Surface, Studies in Surface Science and Catalysis*, V93, Elsevier,

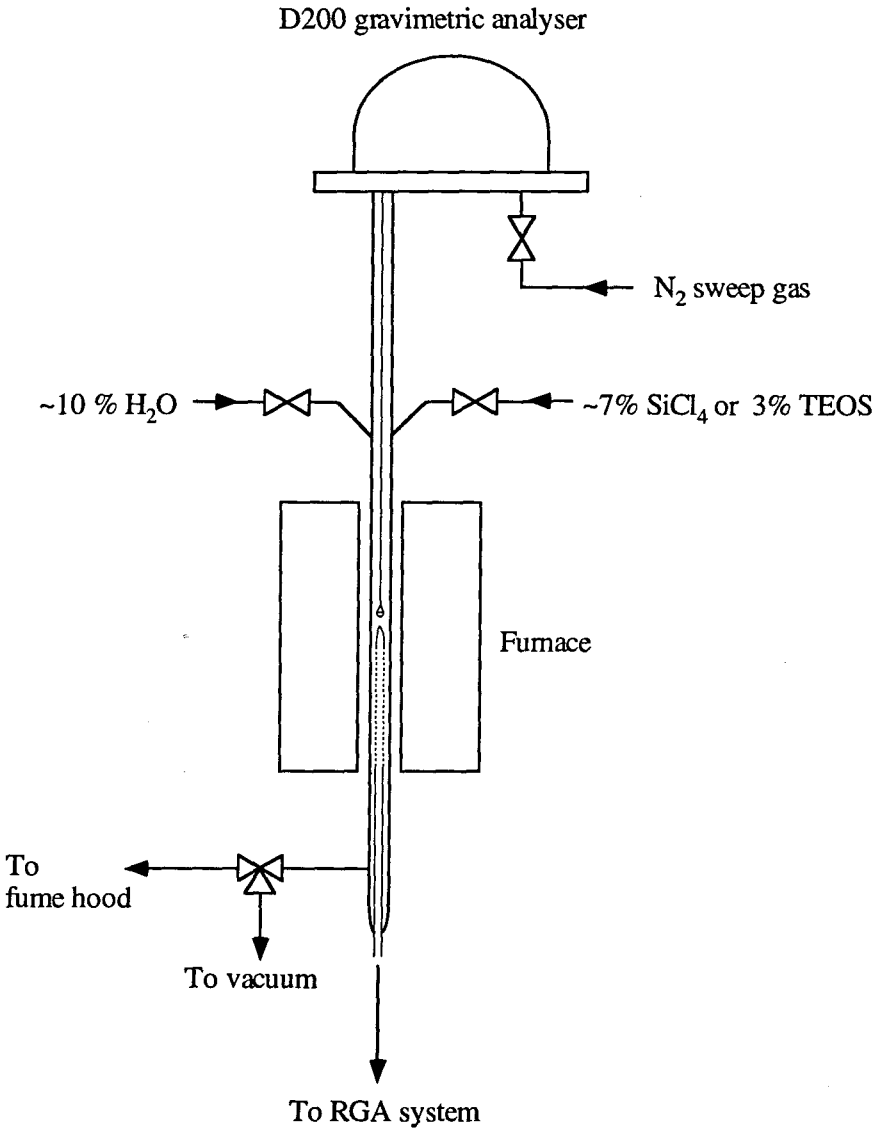

Figure C.1 Reaction schematic for the CVD deposition of silica

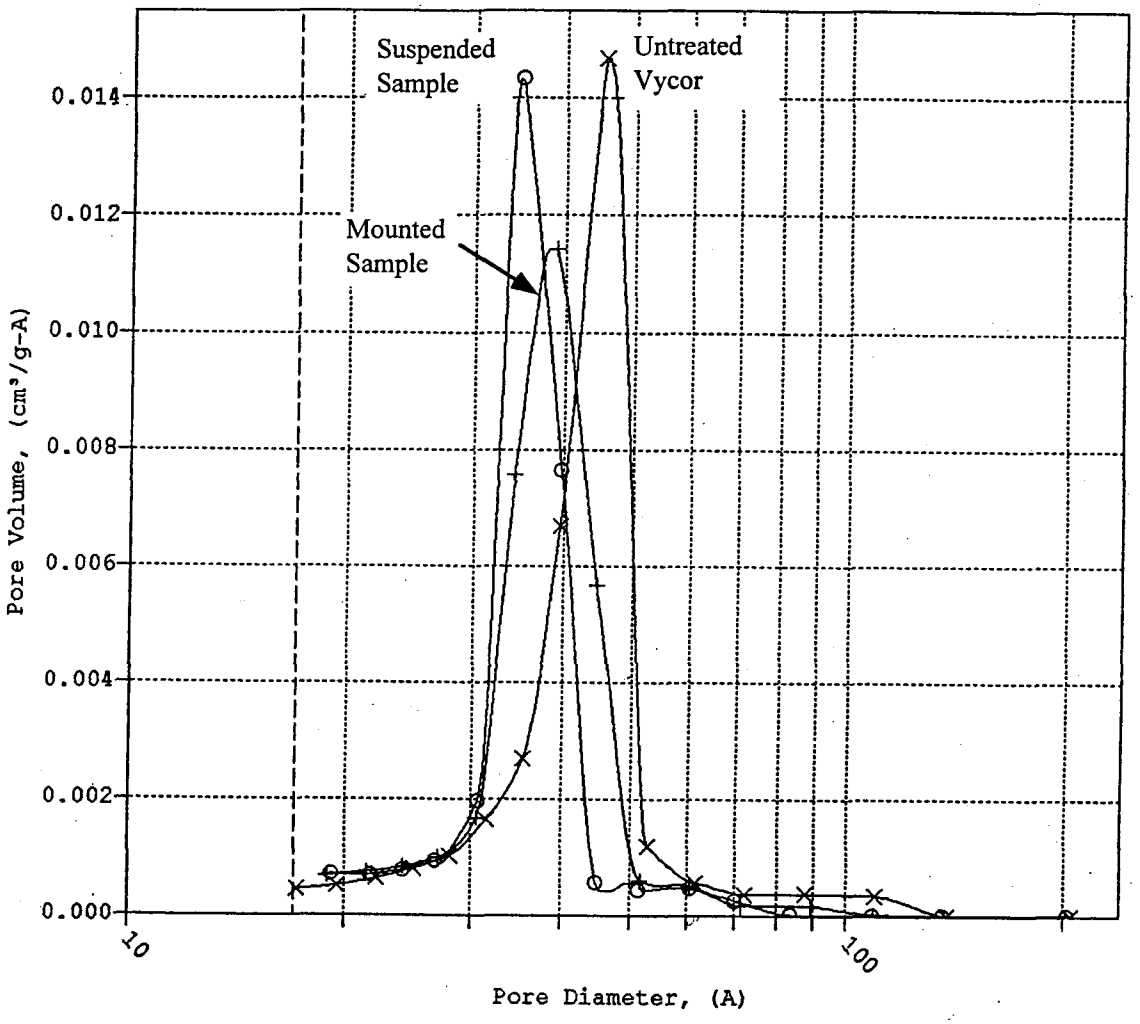

Figure C.2 Pore size distribution of the suspended and mounted Vycor samples, after silica deposition by TEOS pyrolysis

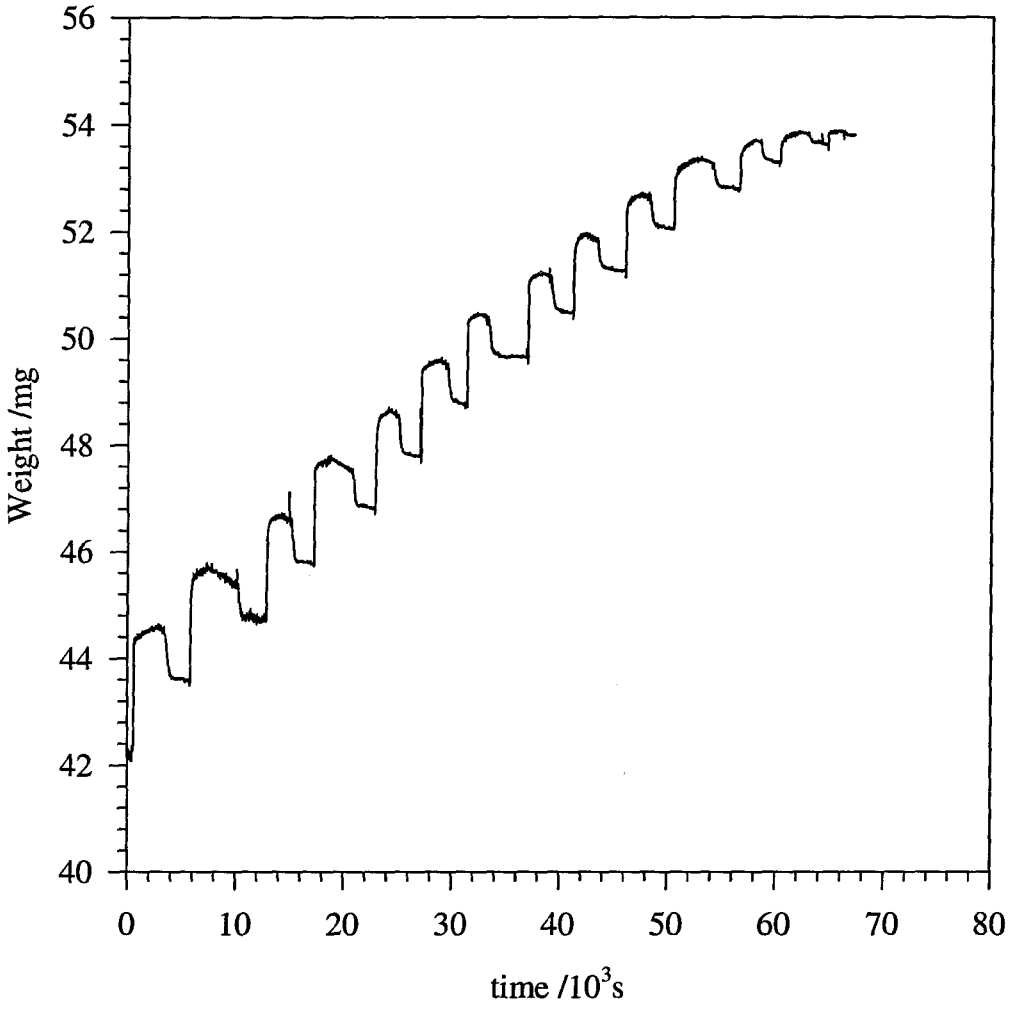

Figure C.3 Weight gain of powdered Vycor after CVD of silica using $SiCl_4$

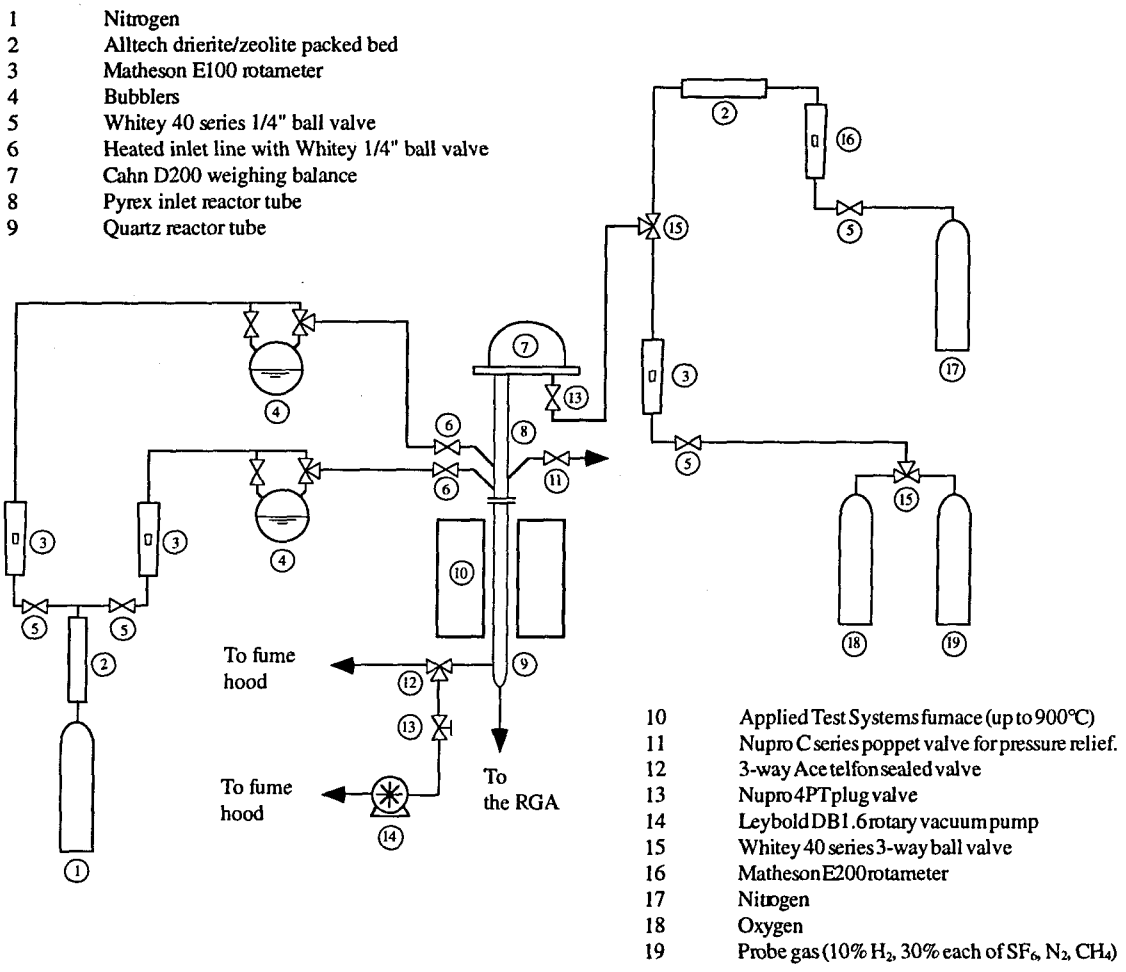

Figure C.4 CVDR and TGA Schematic

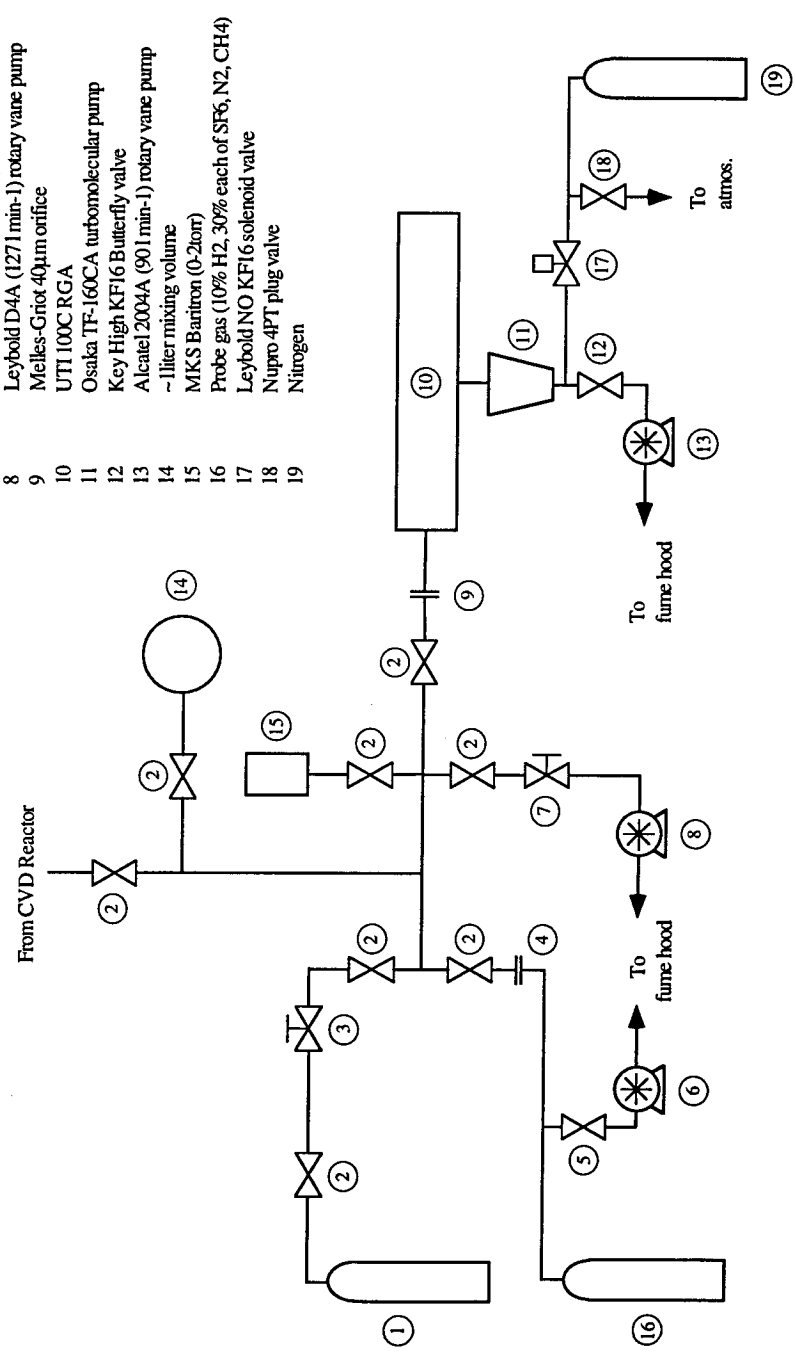

Figure C.5 RGA Schematic

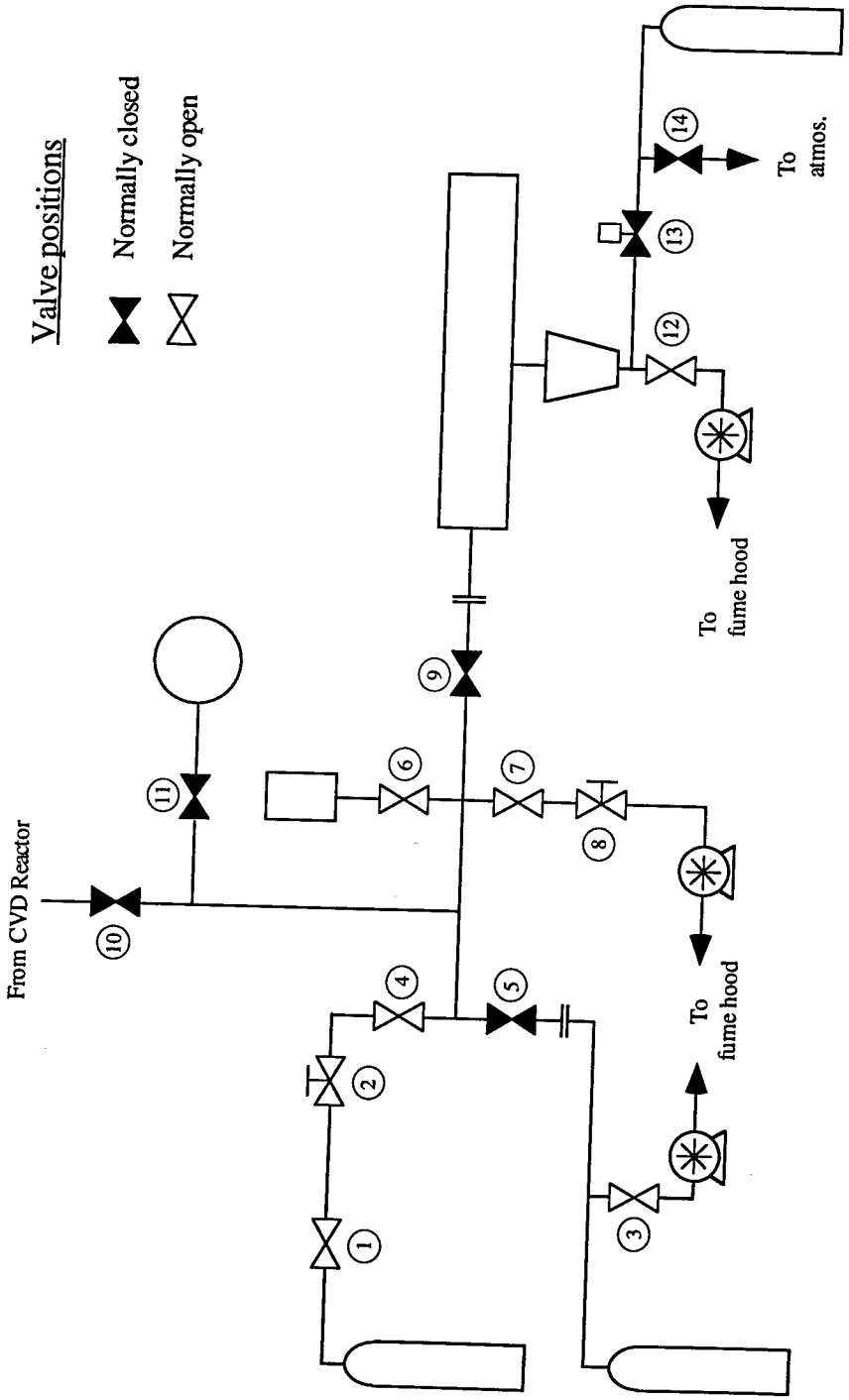

Figure C.6 Valve numbering for quantitative measurements using comparative calibration